Development and Evaluation of Micro-Electrocorticography Arrays for Neural Interfacing Applications

By

Amelia Ann Schendel

A dissertation submitted in partial fulfillment of

the requirements of the degree of

Doctor of Philosophy

(Materials Science)

at the

UNIVERSITY OF WISCONSIN-MADISON

2014

Date of final oral examination: 02/25/2014

The dissertation is approved by the following members of the Final Oral Committee:

Justin C. Williams

Mary Elizabeth Meyerand

David J. Beebe

Frank E. Pfefferkorn

Walter F. Block

Kevin W. Eliceiri

Azam S. Ahmed

ABSTRACT

Neural interfaces have great promise for both electrophysiological research and therapeutic applications. An ever-developing medical knowledge base, combined with continual advancements in techniques for the study of neural circuitry, has resulted in a vast transformation of the research and clinical requirements for neural interfacing devices over the past several years. The constant improvement of algorithms for more effective brain-computer interfacing and neural prosthetics has led to a push for complimentary development of more biocompatible devices with the long-term *in vivo* reliability necessary for implantation in human patients. In addition, the advent of optogenetics, which enables scientists to evoke cellular activity by stimulation with specific light wavelengths, has resulted in a demand for transparent electronics, through which light can be transmitted, as well as devices with electrodes, for recording neural signals, integrated with light sources, for stimulation. Whether for the study of neural circuitry or for neural prosthetic or other therapeutic applications, micro-electrocorticography (micro-ECoG) arrays have proven extremely useful as neural interfacing devices. These devices strike a balance between invasiveness and signal resolution, an important step towards eventual human application.

The objective of this research has been to make design improvements to micro-ECoG devices in order to enhance both biocompatibility and device functionality. To aid in and best evaluate the effectiveness of these improvements, a cranial window imaging method for *in vivo* monitoring of the longitudinal tissue response post device implant was developed. Employment of this method provided valuable insight into the way tissue grows around micro-ECoG arrays after epidural implantation, spurring a study of the effects of substrate geometry on the meningeal tissue response. The results of the substrate footprint comparison suggest that a more open substrate geometry provides an easy path for the tissue to grow around to the top side of the device, whereas a solid device substrate encourages the tissue to thicken beneath the device, between the electrode sites and the brain. The formation of thick scar tissue

between the recording electrode sites and the neural tissue is disadvantageous for long-term recorded signal quality, and thus future micro-ECoG device designs should incorporate open-architecture substrates for enhanced longitudinal *in vivo* function.

In addition to investigating improvements for long-term device reliability, it was also desired to enhance the functionality of micro-ECoG devices for neural electrophysiology research applications. To achieve this goal, a completely transparent graphene-based device was fabricated for use with the cranial window imaging method and optogenetic techniques. The use of graphene as the conductive material provided the transparency necessary to image tissues directly below the micro-ECoG electrode sites, and to transmit light through the electrode sites to underlying neural tissue, for optical stimulation of neural cells. Furthermore, graphene is much more flexible than indium tin oxide, the material traditionally used for transparent electronics applications. Thus, graphene is a more ideal choice for thin-film, flexible electronic devices, which are less invasive than traditional silicon-based arrays and provide enhanced long-term stability of recorded neural signals.

This dissertation provides valuable insight into tissue growth patterns around micro-ECoG arrays, as well as some suggested mitigation strategies for minimizing the effects of scarring on recorded signal quality. Furthermore, the cranial window imaging method and the transparent micro-ECoG array will be useful tools for future research involving chronic *in vivo* imaging and optogenetics.

To my loving parents.

Dad, you have been, and always will be my inspiration.

Mom, your unconditional love, patience, and support have made me the person I am today.

ACKNOWLEDGEMENTS

First and foremost, I would like to thank Prof. Justin Williams for giving me the opportunity to be a part of the NITRO lab, and for guiding me along the way to the completion of this thesis. Under his direction, I have learned to be a self-motivated, independent thinker, and have been provided with all of the tools necessary for future research success.

Special thanks go to Dr. Kevin Eliceiri for his invaluable advice and assistance with providing direction to my research. I am extremely lucky to have had the opportunity to collaborate with Dr. Eliceiri, as his vast knowledge, insight, and enthusiasm for science have greatly enhanced the quality of my work. Thank you to the remaining members of my committee, Prof. Mary-Elizabeth Meyerand, Prof. David Beebe, Prof. Frank Pfefferkorn, Prof. Walter Block, and Dr. Azam Ahmed, for their helpful advice and guidance over the years.

I would also like to thank all of the members of the NITRO lab, present and past, for their continual assistance and support with both scientific and non-scientific matters. I would especially like to acknowledge Dr. Sanitta Thongpang, Sarah Brodnick, Tom Richner, Léo Walton, Brad Lindevig and Kevin Cheng. The friendships I have formed are among the most valuable things I will be taking from my graduate experience. Thanks also to Mike Nonte, Paige Bostrom, and Mohammed Hayat for voluntarily contributing their precious time to helping with my research studies.

Additional thanks go to the members of the Wisconsin Center for Applied Microelectronics for striving to provide a safe, pleasant, and productive cleanroom environment and for always being willing to answer questions and provide assistance. Thank you to the LOCI researchers, especially Dr. Corinne Vokoun, Dr. Julie Last, and Dr. Ruth Sullivan, for assistance with imaging and histological tissue analysis. Thank you to Prof. Ramin Pashaie and his students

Seth Fry and Farid Atry for their valuable assistance with obtaining optical coherence tomography images, and to Professor Jack Ma and his student Dong-Wook Park for their wonderful collaboration on the CLEAR device project. Also, thank you to Beth Gray at RARC for her tireless efforts to help with tissue slicing and staining, and to Dr. Lisa Krugner-Higby for her constant willingness to provide her expert opinion regarding anything related to animal studies.

I would like to express my deepest gratitude to all of my family and friends for their belief in me and my work. Thank you to my father, Dr. Mike Schendel, for inspiring me to pursue a graduate degree in a technical discipline, and for always lending his advice in matters of science as well as ethics. Thanks to my mother, Jan Schendel, for her unconditional love and patience, even through the most stressful times, and to my brother, Greg Schendel, for all of the visits to Madison to help me move apartments. Thank you to all of my friends, both in Madison and Minneapolis, especially Megan Braaten, Mahima Gupta, Dana Dentice, and the members of the Dream Team, for helping to keep my life balanced by getting me out of the lab.

Finally, a tremendous thank you to my fiancé, Ed Sandberg, for always being there for me and for listening when I needed to be heard and speaking when I needed to listen. For putting up with "date nights" involving working at coffee shops, and, more often, Skype, and for making countless five hour drives and megabus trips between Minneapolis and Madison. Thanks also for reviewing innumerable technical documents with minimal background knowledge. Without his support, or that of a single one of the aforementioned individuals, this document would not have been possible.

This work was supported by the National Institute of Health, the Defense Advanced Research Projects Association, and the University of Wisconsin - Madison.

TABLE OF CONTENTS

LIST OF FIGURES

LIST OF TABLES

1 INTRODUCTION

Background

Neural interfaces are devices which provide an electrical connection between nervous tissue and the *ex vivo* environment. These connections allow for closed-loop control, such as stimulation of neural tissue to excite or inhibit cellular activity, and the ability to record neural signals. The use of neural interfaces for the study of electrophysiology dates back to 1928, when Edgar Adrian reported the ability to record neural potentials using a Lippmann Electrometer, a device invented for measuring small rushes of electric current (Adrian, 1928). Since that time, neuroscientists have continued to develop devices and techniques to improve the study of electrical signaling and neural networks.

One of the most ground-breaking neuroscience techniques that has surfaced in the past several years is optogenetics (Deisseroth, 2011). This is a method in which cell membranes are modified to include light-sensitive ion channels. The incorporation of these channels into neuronal cells allows the cells to be effectively turned "on" and "off" by select light wavelengths. The ability to modulate the activity of specific types of cells by exposing them to light has revolutionized the way scientists study neuronal networks, but has also added to the requirements for neural interface devices, creating the need for implantable optical stimulators and transparent electronics.

Recent developments in neural interfacing technology have also revolved around the use of these devices for therapeutic applications. One of the most common examples of the therapeutic potential of neural interfaces is in the field of neural prosthetics. In this field, signals are recorded from neural electrodes and sent to a microprocessor, which decodes the intent of the user and sends a command to a device, such as a wheelchair or prosthetic limb (Schwartz, 2004). In this way, patients use their neural signals to control devices which they otherwise may not have been able to operate. Additional examples of therapeutic neural interface applications include deep brain stimulation for control of essential tremor (involuntary shaking) from Parkinson's disease, and spinal cord stimulation for pain management (North

et al., 2002; Perlmutter and Mink, 2006). The use of these devices for long-term therapeutic purposes has necessitated the requirement for longitudinal *in vivo* reliability, an unnecessary consideration for neural interfaces strictly used for short-term research applications.

Several different types of electrode arrays can be used for neural interfacing, ranging from invasive devices that penetrate into nervous tissue to completely non-invasive electrode caps worn over the skin (Hopkins et al., 1988; Maynard et al., 1997). Although the most invasive devices, such as traditional silicon intracortical probes, provide the highest signal resolution due to their proximity to nerve cell bodies, there is a large trade-off between recorded signal quality and device biocompatibility (Schwartz et al., 2006). The primary drawback to these types of devices is that the significant scar tissue formation around the implants often renders them unusable within a short time period after implantation (Polikov et al., 2005). Additionally, the inevitable injury caused by these devices can lead to inflammation or infection, which are also detrimental to device function. Conversely, non-invasive electrode arrays, such as electroencephalography (EEG) grids worn over the scalp, do not cause any tissue trauma, but the information contained within the recorded signals is, however, significantly degraded by the amount of bone and skin tissue through which the signals must travel (Leuthardt et al., 2004). To develop a neural interface device that will ultimately be acceptable for long-term human use, it is necessary to strike a balance between the invasiveness of the device and the quality of the recorded signals. For this reason, surface electrode arrays, which are implanted within the body but rest near the neural tissue rather than penetrating it, have been developed. Examples of these types of devices include electrocorticography (ECoG) grids for recording from and stimulation of the cerebral cortex, extradural spinal cord stimulation arrays, and nerve cuff electrodes, which wrap around peripheral nerves (Kumar et al., 1998; Leuthardt et al., 2004; Loeb and Peck, 1996; Rodri´guez et al., 2000; Thongpang et al., 2011).

To conform to the non-uniform, curvilinear exterior of neural tissues, such as the cerebral cortex, epidural space, and peripheral nerves, surface electrode arrays must be developed on flexible substrates. Typically, the substrates of these devices are polymeric in nature, due to the intrinsic dielectric and mechanical compliance properties of these materials (Hassler et al., 2011). Traditional intracortical

electrode arrays require rigid substrates, such as silicon, for insertion into neural tissues, but the mechanical impedance mismatch between the soft brain tissue and the stiff devices can cause a large proportion of the tissue trauma contributing to glial scar formation (Polikov et al., 2005; Rousche et al., 2001). Therefore, an added benefit of using flexible substrates is the allowance of device motion and deformation with the soft surrounding tissues, rather than causing damage. This makes these devices more biocompatible in terms of both invasiveness and rigidity.

As previously mentioned, the proximity of neural interfaces to the structures from which they are recording is a crucial factor contributing to the quality and resolution of the acquired signals (Figure 1.1, Schwartz et al., 2006). Less invasive implants are required to obtain a more compatible interface with nervous tissue. This leads to more stable signal recordings over the long-term. Since neural cell bodies lie in layer V of the cortex and peripheral nerve axons are contained within several layers of connective tissue sheaths, there is an inevitable sacrifice of signal information when shifting to a surface neural recording modality. Although this loss of signal resolution is unavoidable, it does not prohibit the use of surface electrode arrays for tasks which require high-information signals to decode user intent. This is true with brain-computer interfacing and neural prosthetic control (Navarro et al., 2005; Wilson et al., 2006). In fact, studies have been performed which validate the employment of micro-electrocorticography (micro-ECoG) surface arrays for such applications (Humayun et al., 2003; Leuthardt et al., 2009; Rouse et al., 2013).

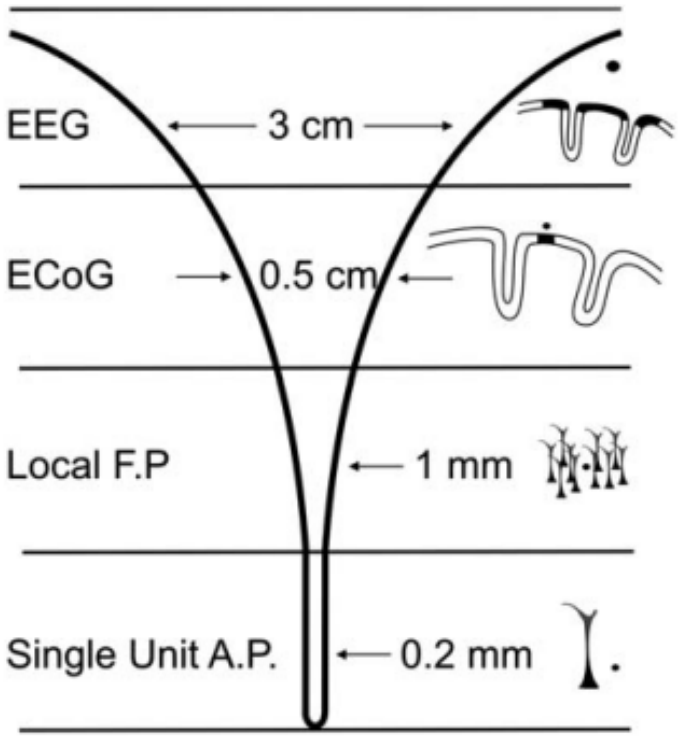

Figure 1.1. Spatial signal domains for the four primary recording modalities of neural interfaces. While penetrating probes can recorded single unit action potentials (A.P.s), the invasiveness of these devices causes significant scarring, which decreases signal longevity. Micro-ECoG arrays are capable of recording local field potentials (Local F.P.s), but rest on the surface of the brain, creating a balance between signal information and device invasiveness (Schwartz et al., 2006).

The validation of surface electrode arrays for neural interfacing tasks has triggered a large body of research into the development of more advanced, yet less invasive devices to address the requirements of the field. Here, we discuss examples of new technologies for enhancing *in vivo* device reliability and function in terms of the novel design modifications employed.

Open Architecture and Resorbable Device Substrates

One method for reducing the tissue response to implanted medical devices is to minimize the amount of foreign material present. This has been demonstrated in the neural field with histological

studies of the cellular response to open-architecture intracortical devices (Seymour and Kipke, 2007). Through these studies, it has been discovered that the presence of holes through implanted micro-electrode arrays allow for tissue integration, and also for diffusion of neural chemicals through the device. This has been demonstrated to be another crucial factor for maintaining normal signal transduction and cell health (Polikov et al., 2005; Richardson-Burns et al., 2007b; Roitbak and Syková, 1999).

Recently, researchers have begun to adopt more open substrate geometries for neural surface electrodes. Kim et al have demonstrated the benefits of a mesh-like neural surface electrode array, but have taken the idea further by minimizing the surface area of the substrate material, and also its thickness (Kim et al., 2010). As in the case of penetrating electrode arrays, surface devices require a sufficient degree of structural integrity for handling during processing and implantation. However, this robustness is not necessary for the function of the device *in vivo*, and can be disadvantageous, causing an increased amount of pressure on neural tissue. Additionally, the increased structural integrity required for device handling can result in a decrease in flexibility, diminishing the ability of these devices to conform to non-uniform tissue surfaces. To create a device with adequate mechanical stability, capable of withstanding the required processing and implantation procedures, but flexible enough to conform with neural structures, Kim et al employed the use of a dissolvable silk matrix. This matrix was adhered to a mesh-type micro-ECoG array with a very thin (~2.5 μm) polyimide (PI) layer insulating the traces. The silk matrix was robust enough to permit precise implantation of the electrode arrays over the feline visual cortex, but dissolved away within 1 hour after implantation, allowing the array to conform to the gyri and sulci of the brain, thus enhancing the quality of the recorded signals by increasing connectivity of the electrodes with the cortical tissue. Although there are many other biodegradable polymeric materials which could be employed, the transparency, robustness, and flexibility of silk, combined with its tunable dissolution properties make it an ideal candidate for neural interfacing applications.

In addition to bio-resorbable substrate materials, dissolvable conductive materials, such as the melanin semiconducting films created by Bettinger et al, are also desirable for neural applications (Bettinger et al., 2009). While these types of devices may not be relevant for long-term neural implants,

they are extremely beneficial for neural regeneration purposes, in which electrical stimulation has been shown to promote axonal growth. In these applications, it is desired to stimulate nerves over the short term to promote re-growth, but removal of devices after tissue regeneration would cause undesirable trauma. Thus, completely dissolvable electronic devices would be ideal. Melanin is an excellent candidate for implantable resorbable electronic devices, since it is naturally present in the body, and so its presence should not cause an adverse tissue response. Although Bettinger et al have laid down the groundwork for these types of neural regenerative systems, much investigation is still required into making these types of devices completely functional.

Conductive Polymers

The use of conductive polymers in neural interfaces has rapidly advanced over the past several years, as these materials have been shown to have increased device flexibility, biocompatibility, and recording/stimulation capabilities (Cui and Martin, 2003; Widge et al., 2007). The bio-degradable complex polymer melanin is just one example of a conductive polymeric material, with polypyrrole (PPy), polythiopene (PTh), and polythiopene derivatives, such as poly(3,4-ethlyene dioxythiopene) (PEDOT) being the most popular non-resorbable alternatives (Green et al., 2008). The conducting capabilities of these materials are a result of conjugated double bonds present in the polymeric backbone and dopant ions introduced into the molecular structure (Green et al., 2008). When they are incorporated into neural interfacing devices, the flexibility and high surface area of these materials improve the conformity of the devices to neural surfaces, and increase tissue integration, which leads to enhanced recording and stimulation parameters, with extended device lifetime (Richardson-Burns et al., 2007a; Widge et al., 2007).

Khodagholy et al have demonstrated the use of poly(3,4-ethlyene dioxythiopene) poly(styrenesulfonate) (PEDOT:PSS) as a conductive coating for electrocorticographic recordings in rats (Khodagholy et al., 2011). This particular co-polymer was chosen for its biocompatibility, chemical stability, and commercial availability. Devices were fabricated on a Parylene C substrate, which was also

selected for its superior performance *in vivo*. The performance of arrays of gold electrodes coated with PEDOT:PSS was compared to that of bare gold electrode arrays, with the finding that the PEDOT:PSS coating enhanced signal resolution in the 1-10 Hz and 30 Hz bands.

Castagnola et al have also shown the use of PEDOT-carbon nanotube (CNT) coated micro-electrodes for use in micro-electrocorticography arrays (Castagnola et al., 2013). These devices were patterned onto a polyimide substrate and their viability was verified by recording of sensory evoked potentials in the rat cerebral cortex. The PEDOT-CNT coating was found to reduce the electrochemical impedance of the recording electrodes by about four orders of magnitude in comparison to un-coated gold electrode sites.

Although long-term studies are required to assess the bio-stability of conductive polymer coatings, these materials have shown great promise for increasing the recording and stimulation capabilities of neural electrodes. The majority of conductive polymer investigations have been directed at their use with intracortical devices (Ludwig et al., 2006; Xiao et al., 2004; Yang et al., 2005), however the two studies reported above outline their benefits for neural surface electrode arrays. In particular, the flexibility of these materials allow for the creation of increasingly conformal devices, which will enhance biocompatibility, improve recorded signal quality and longevity, and decrease the stimulation currents required to elicit behavioral responses.

Transparent Electronics

The development of optogenetics has revolutionized the way scientists study neural circuitry, while increasingly more sophisticated *in vivo* imaging modalities provide the tools necessary to understand the behavior of the multitude of cell and tissue types regulating neuronal function and the *in vivo* stability of neural interfaces. Whereas the transparency of penetrating probes is irrelevant since these devices are most often embedded deep within the tissue, the use of surface electrode arrays for optogenetic or imaging studies requires light transmission through the devices, to or from the underlying

nervous tissue. This necessity has ignited a wave of research into developing thin-film, transparent electrodes for neural interfacing.

Given that the use of transparent polymeric substrates, such as Parylene C and silicone, has been well established for neural devices (Grill and Mortimer, 1998; Hassler et al., 2011; P. Ledochowitsch et al., 2011; Schendel et al., 2013), the main challenge in the development of completely transparent neural electrode arrays is finding a suitable conductor material. Although conductive polymers, such as PEDOT, can be formulated to have transparent properties, there are many processing difficulties involved in obtaining viable transparent films with the appropriate conductivity (Ellmer, 2012; Ha et al., 2004). Therefore, these materials are more often used as coatings rather than solitary conductors. The most commonly used transparent conductive film to date is indium-tin oxide (ITO).

ITO has been demonstrated in neural applications for recording of both electrocorticographic potentials and retinal neural signals. Fabrication and bench-top validation of transparent ITO-based micro-ECoG arrays was achieved by Ledoschowitsch et al, followed by Kwon et al, who incorporated ITO electrode sites and miniature LEDs into a thin-film micro-ECoG platform for simultaneous stimulation and recording of optically evoked potentials in transgenic animal models (Kwon et al., 2012; Peter Ledochowitsch et al., 2011). ITO-based devices have also been designed by Gunning et al for recording of signals from retinal ganglion cells, but at this time have only been validated *in vitro* (Gunning et al., 2005). Transparent electrodes patterned onto contact lenses would have utility for monitoring eye electrophysiology via electroretinography (Selner et al., 2011), however the brittle nature of ITO limits its ability to conform to curved surfaces, such as contact lenses.

Recently, researchers have been making an effort to find alternative transparent conductors, due to the brittleness, cost, and processing difficulty of ITO films (Ellmer, 2012). Perhaps the most promising alternatives for neural applications are organic materials, such as carbon nanotube networks and graphene sheets (Alwarappan et al., 2009; Chen et al., 2008; Lin et al., 2009). These materials provide the flexibility and biocompatibility required for use in neural surface arrays, and are an improvement on the brittle ITO films.

Research Objective

Neural surface electrode arrays strike a delicate balance between *in vivo* reliability and recorded signal quality. Effective biomedical deployment of these devices requires both of these properties, and is a logical next step towards clinically approved brain-computer interfaces. This dissertation presents research on the development and evaluation of micro-ECoG arrays for neural interfacing applications. The problems discussed and addressed include: evaluation of the tissue response to epidurally implanted micro-ECoG arrays via *in vivo* imaging, determination of the most-suitable micro-ECoG substrate geometry for long-term *in vivo* device reliability, and the fabrication and validation of a completely transparent graphene-based micro-ECoG array, for optogenetic and neural imaging applications.

Dissertation Organization

This dissertation is organized into five main sections, some of which have been taken from previously published work, or work that is in preparation for publication. The introductory section above is a modified version of an invited review article entitled "Advanced Materials for Neural Surface Electrodes", which is in preparation by the author for submission to the journal "Current Opinions in Solid State and Materials Science".

Chapter 2 discusses the results of a study involving imaging of vascular growth around epidurally implanted micro-ECoG arrays via a cranial window. This chapter gives an overview of the cranial window implantation and imaging techniques. These methods were specifically modified for study of the tissue response to neural surface electrode arrays. Use of this method is reported throughout this dissertation, as a supplementary tool for evaluating micro-ECoG device patency *in vivo*. The content of Chapter 2 was taken from previously published work in the Journal of Neuroscience Methods, entitled "A cranial window imaging method for monitoring vascular growth around chronically implanted micro-ECoG devices".

Chapter 3 summarizes a comparison between the tissue responses to micro-ECoG devices using two different substrate footprints. The study focuses on determining the impact of device geometry on

scar tissue formation using the cranial window imaging method (Chapter 2), in conjunction with second harmonic generation imaging, optical coherence tomography, and traditional histological techniques. The study results improve the selection of ideal surface electrode array geometries for neural prosthetic applications. Chapter 3 has been recently submitted to the Journal of Neural Engineering for publication under the title "The effect of micro-ECoG substrate footprint on the meningeal tissue response".

In Chapter 4, the fabrication of a graphene-based, completely transparent micro-ECoG device is described. The viability of this device for *in vivo* experiments involving optogenetics and cranial window imaging is also demonstrated. The results of the study prove that the graphene-based device is a practical alternative for devices containing ITO, a more traditionally used transparent conductor, with lower flexibility and ever increasing cost. This work is in the final stages of preparation for submission under the title "Carbon Layered Electrode Array (CLEAR) Technology for Neural Imaging and Optogenetic Applications" to the journal: Nature Materials.

The final section, Chapter 5, draws conclusions and outlines future directions for this work. Appendices are also included which provide detailed descriptions of device fabrication processes, animal experimentation procedures, and additional supplemental material relevant to the reported studies.

2 CRANIAL WINDOW IMAGING OF MICRO-ECOG DEVICES

Abstract. Implantable neural micro-electrode arrays have the potential to restore lost sensory or motor function to many different areas of the body. However, the invasiveness of these implants often results in scar tissue formation, which can have detrimental effects on recorded signal quality and longevity. Traditional histological techniques can be employed to study the tissue reaction to implanted micro-electrode arrays, but these techniques require removal of the brain from the skull, often causing damage to the meninges and cortical surface. This is especially unfavorable when studying the tissue response to electrode arrays such as the micro-electrocorticography (micro-ECoG) device, which sits on the surface of the cerebral cortex. In order to better understand the biological changes occurring around these types of devices, a cranial window implantation scheme has been developed, through which the tissue response can be studied *in vivo* over the entire implantation period.

Rats were implanted with epidural micro-ECoG arrays, over which glass coverslips were placed and sealed to the skull, creating cranial windows. Vascular growth around the devices was monitored for one month after implantation. It was found that blood vessels grew through holes in the micro-ECoG substrate, spreading over the top of the device. Micro-hematomas were observed at varying time points after device implantation in every animal, and tissue growth between the micro-ECoG array and the window occurred in several cases. Use of the cranial window imaging technique with these devices enabled the observation of tissue changes that would normally go unnoticed with a standard device implantation scheme.

Introduction

The formation of scar tissue around chronically implanted neural micro-electrode arrays can significantly decrease the quality of the recorded signals, often rendering the devices unusable (Szarowski et al., 2003; Williams et al., 1999; Woolley et al., 2011). This well-known problem has led to a push towards less invasive neural implants, such as electrocorticography (ECoG), and more recently, micro-

ECoG (Figure 2.1), which sit on top of the cortical surface rather than penetrating into it (Gierthmuehlen et al., 2011; Kitzmiller et al., 2006; Thongpang et al., 2011; Viventi et al., 2011; Wang et al., 2009). These devices are thought to strike a potential balance between the spatial resolution necessary for performing brain computer interfacing (BCI) tasks and the long-term stability required for human implantation.

Due to their minimally invasive nature, it is thought that the tissue surrounding surface electrode arrays elicits very little response to their presence. However, although there has been extensive research into *in vivo* biological responses to penetrating neural micro-electrode arrays (MEAs) (Williams et al., 2007; Woolley et al., 2011), there has been little investigation into tissue responses to MEAs implanted on the surface of the cerebral cortex. The assumption that these devices elicit little tissue response is based on results from traditional histological studies of brains implanted with surface electrode arrays (Henle et al., 2011). In order to perform these types of studies, however, the brain must be removed from the skull, and in the process, the electrode array is also removed from the cortical surface, resulting in disruption of the dura mater and any blood vessels and tissues that have grown around the device. Fong et al have reported vascular changes occurring around clinically implanted macro electrocorticography grids for mapping of seizure onset zones (Fong et al., 2010). In order to verify whether similar tissue changes occur around micro-ECoG devices, an imaging technique that does not require explantation of the brain and device would be advantageous.

The cranial window imaging method has been used extensively for other *in vivo* biological studies, particularly for imaging of tumor formation and vascular dynamics (Brown et al., 2010; Fukumura et al., 2001; Villringer et al., 1994). This technique employs a glass coverslip, chronically implanted on the surface of the cerebral cortex, through which the cranial tissue can be observed over extended time periods, from weeks to months. Since micro-ECoG devices sit on the surface of the cerebral cortex, their implantation is amenable to this imaging approach.

The objective of this study was to use a cranial window imaging method to study the tissue reaction to implanted micro-ECoG devices. By placing a glass coverslip over the top of the micro-ECoG

device during implantation, a cranial window model was developed for imaging the tissue surrounding the implanted device. Use of this technique makes it possible to view the vasculature and other soft tissues that are often destroyed during traditional histological experiments, and also allows for observations of the tissue response at many different time points per animal, since the tissue can be imaged longitudinally *in vivo.* In this study we concentrate on the imaging of vascular responses to implanted micro-ECoG devices, as a first step towards chronic imaging of a multitude of different cell types.

Methods

Micro-ECoG Fabrication

The micro-ECoG array is shown in Figure 2.1 (a). The device consisted of 16 electrode sites encapsulated in a Parylene C substrate. 12 holes were present through the device substrate, between the electrode sites. The electrode sites were 200 microns (μm) in diameter and the spacing between the site centers was 750 microns. The devices were fabricated following the process described in Figure 2.1 (b) (Thongpang et al., 2011). A Parylene C layer was deposited onto a blank silicon wafer using a vacuum deposition system (PDS 2010 Labcoter 2, Specialty Coating Systems Inc.). Next, photolithography was used to define the electrode sites and traces onto the layer of Parylene. The wafer was then placed in a metal evaporation system and a chrome adhesion layer, followed by gold and platinum was deposited onto its surface to form the conductive layer. After the metal deposition, lift-off techniques were used to remove unwanted metal from the surface of the wafer, leaving behind only the desired electrode sites and traces. Another layer of Parylene was then deposited on top of the metal layer, insulating the traces. Next, reactive ion etching with oxygen plasma was used to define the outline of the device and open holes through the Parylene substrate, as well as to remove the Parylene over the electrode sites, revealing the metal beneath. Finally, the wafer was soaked in water, releasing the devices from the silicon surface. After the devices were released from the wafer, printed circuit board (PCB) connectors (Imagineering

inc., IL) were attached so that neural signals could be recorded from the electrode sites (Thongpang et al., 2011). The devices were then bench tested to verify electrode patency, and sterilized with ethylene oxide gas prior to implantation.

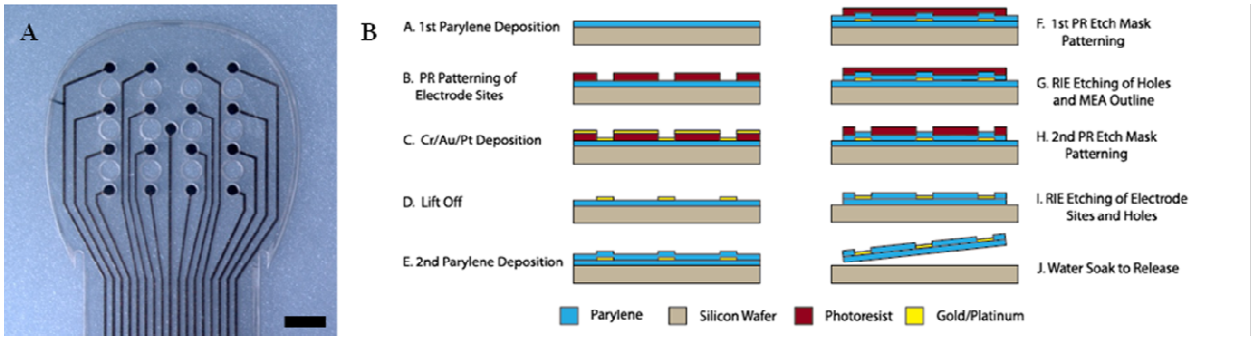

Figure 2.1. Micro-ECoG device and fabrication process. **(a)** The micro-ECoG device consisted of a Parylene C substrate with 16 Cr/Au/Pt electrode sites. 12 holes through the Parylene substrate are visible between the electrode sites. Scale bar represents 750 µm. **(b)** Micro-ECoG fabrication process. A: 15 µm of Parylene was deposited on a blank Si wafer. B: 1813 photoresist was used to pattern the electrode sites and traces onto the Parylene. C: 10 nm of chrome, 200 nm of gold, and 20 nm of platinum was deposited using an electron beam evaporator. D. Lift off techniques were used to remove the metal that was on top of the photoresist. E. 10 µm of Parylene was deposited onto the sample. F. Photolithography was used to create an etch mask. G. RIE was used to etch through the 1st 15 µm of Parylene, creating the holes and the outline of the micro-ECoG device. H. A second photoresist etch mask was patterned. I. RIE was used to etch the Parylene off of the electrode sites and finish etching through the holes and the MEA outline. J. The sample was soaked in water and the devices were released from the Si wafer.

Ethics Statement

All animal procedures were approved by the Institutional Animal Care and Use Committee (IACUC) at the University of Wisconsin - Madison. All surgical procedures and *in vivo* imaging sessions were performed under isoflurane gas anesthesia. All efforts were made to minimize animal discomfort.

Surgical Implantation Procedure

Male Sprague Dawley rats (n = 7, Charles River) weighing 250-300 grams were implanted with micro-ECoG devices and cranial windows. Prior to surgery, animals received subcutaneous injections of dexamethasone (2 mg/kg body weight, AgriLabs) to prevent swelling of the brain during surgery, buprenorphine hydrochloride (0.05 mg/kg, Reckitt Benckiser Healthcare Ltd.) for pain management, and ampicillin (50 mg/kg, Sage Pharmaceuticals) to prevent infection of the implantation site. Animals were anesthetized with isoflurane gas and held in a stereotaxic frame for the duration of the surgical procedure. Heart rate and blood oxygen level were monitored throughout the surgery using a pulse oximeter.

The micro-ECoG implantation scheme is diagrammed in Figure 2.2. A craniotomy was made on one hemisphere of the rat skull, over somatosensory cortex, using a #107 engraving cutter. Through this craniotomy, the micro-ECoG device was implanted epidurally, and a circular glass coverslip, 5 mm in diameter and 0.15 mm thick, was placed over the top of the electrode array. An epidural implantation scheme was chosen in order to minimize trauma to the tissue underlying the device. Once the device and coverslip were in place, the PCB connector and coverslip were affixed to the skull using UV curable dental acrylic (Fusio dental acrylic, Pentron Clinical). A ground wire was run from the PCB connector to two ground screws (stainless steel, 00-80x1/8 inch) drilled into the back of the skull using a #56 drill bit. A reference wire was run from the PCB connector to a reference screw affixed to the front of the skull, contralateral to the micro-ECoG device. The screws and wires were then covered in dental acrylic and the skin was sutured around the acrylic headcap. After surgery, animals received another dose of buprenorphine as well as ampicillin injections twice daily for one week.

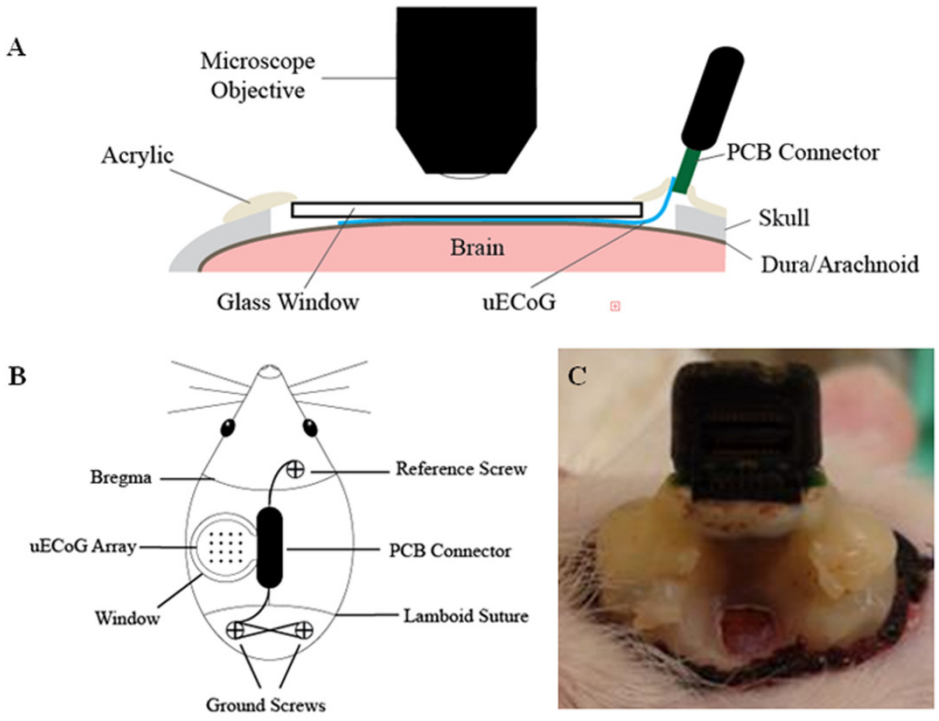

Figure 2.2. Cranial window implantation scheme. **(a)** Cross-sectional diagram of the window imaging implantation scheme, in which a glass cover slip was affixed over the top of an epidurally implanted micro-ECoG array. **(b)** Top view of the cranial window implant setup. **(c)** Rat implanted with a micro-ECoG array and cranial window.

In addition to the animals implanted with the micro-ECoG devices, four rats were implanted with control windows. For these animals, the surgical procedure followed that described above, except that no micro-ECoG devices were implanted and instead the glass coverslips were placed directly on top of the dura-mater. Screws were implanted in the control animals, just as in the animals that received devices, for headcap stability purposes as well as to mimic as closely as possible the surgical procedure for the micro-ECoG array implantation. Once affixed to the skull, the screws were covered in dental acrylic to form a smooth headcap.

To determine whether the tissue reaction could be a response to the presence of the window itself touching the dura mater, one of the control animals was implanted with a second control window, which sat up on the edge of the skull (with the diameter of the craniotomy smaller than the that of the window),

such that the surface of the glass was not at all in contact with the dura mater. The gap between the window and the brain was filled with sterile saline before the edges of the window were sealed. This window sitting up on the skull edge was implanted in addition to the standard control window that sat directly on the surface of the dura mater (with the diameter of the craniotomy larger than that of the glass window). The standard control window was located on the left hemisphere of the rat's brain, over sensory-motor cortex, while the control window sitting up on the edge of the skull was located over the sensory-motor cortex on the right hemisphere. The rest of the surgical procedure followed that described above.

Vascular Imaging

The brain vasculature was imaged through the cranial window, using an upright fluorescent microscope (Leica MZ 16F, Leica Microsystems). For each imaging session the animals were anesthetized using a combination of isoflurane gas and subcutaneously injected dexmedetomidine hydrochloride (0.1 mg/kg, Orion Pharma). Ear bars were inserted in order to hold the animal still and prevent breathing artifacts. Fluorescein isothiocyanate labeled dextran (FITC-dextran) (30 mg/kg, 2,000,000 average molecular weight, Sigma Aldrich product #52471) was administered via tail vein injection so that the blood vessels would fluoresce under blue (460-500 nm, GFP2 filter) light, as shown in Figure 2.3. FITC-dextran is commonly used for visualizing microcirculation *in vivo* (Foley et al., 2012; Garkavtsev et al., 2004; Kleinfeld et al., 1998). It is advantageous, because it remains in circulation unless there is a breach in the wall of the blood vessel, thus allowing one to discriminate between old blood that has congealed outside the vessel walls prior to FITC injection, and new blood that is actively leaking out of the vessels after the time of injection (Mayhan and Heistad, 1985). After the imaging sessions were complete, the animals received subcutaneous injections of atipamezole hydrochloride (0.3 mg/kg, Orion Pharma) to reverse the anesthesia.

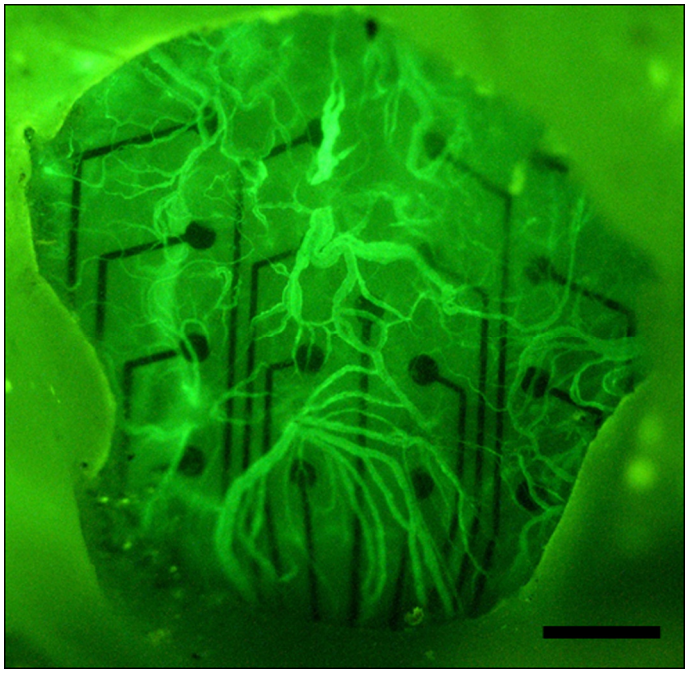

Figure 2.3. Example of observed vascular growth. Blood vessels growing over the top of an epidurally implanted micro-ECoG array 30 days after implantation. Image was taken using an upright fluorescent microscope with broad spectrum light and a GFP-2 filter. Rat was injected with 6 mg of FITC-Dextran dissolved in 0.5 ml saline solution. Scale bar represents 750 µm.

Electrode Site Impedance Measurement

To test the hypothesis that changes in the tissue surrounding the device would result in changes in the electrical recording capability, the impedance spectrum of each electrode site was measured on the same days that the cortical vasculature was imaged. Impedance spectra were obtained for each electrode site using a potentiostat (Autolab PGSTAT12). Animals were tested bi-weekly for up to 10 weeks post implantation, after which they were euthanized by cardiac perfusion.

Histological Analysis

The cortical vasculature was examined post-euthanasia to determine whether the presence of the micro-ECoG device had any detrimental effects on the vasculature deeper within the cortex, which could

not be seen through the cranial window. The vasculature was labeled following the protocol described by Li et al, in which a solution of lipophilic1,1′-dioctadecyl-3,3,3′,3′-tetramethylindocarbocyanine perchlorate (DiI) was injected into the circulatory system during cardiac perfusion of the animal (Li et al., 2008). After perfusion, the brain tissue was carefully dissected from the skull and sectioned into 200 µm thick coronal slices using a vibratome (Leica VT1200). The slices were then placed on slides and sealed following the method described in the Li protocol (Li et al., 2008). The slides were imaged under green (541-551 nm, G filter) light using the same fluorescent stereoscope described above.

Results

Longitudinal Tissue Response

The progression of vascular growth around an epidurally implanted micro-ECoG device is shown in Figure 2.4. Blood vessels began to grow through individual holes in the Parylene substrate of the device on day five, and continued to spread over the entire top surface of the micro-ECoG array over time. In this example, it appears that there had been a micro-hematoma on day 10. The dark areas in the image are indicative of old blood that had pooled beneath the window. On day 15, the bleed was still present, but 17 days after implantation it had begun to diminish, and by day 22 the hematoma had completely resolved itself. By 24 days after implantation of the micro-ECoG device, the vasculature had stabilized and no more significant blood vessel changes were observed. The stabilization of the vasculature approximately 24 days post implantation was consistent across all animals in the study. Additionally, the presence of micro-hematomas around the micro-ECoG device was observed in every animal; however, these hematomas did not always occur at the same time point after device implantation. For the animal shown in Figure 2.4, on days 3 and 15 the tail vein injection of FITC-dextran was not successful, so the images were taken in bright field.

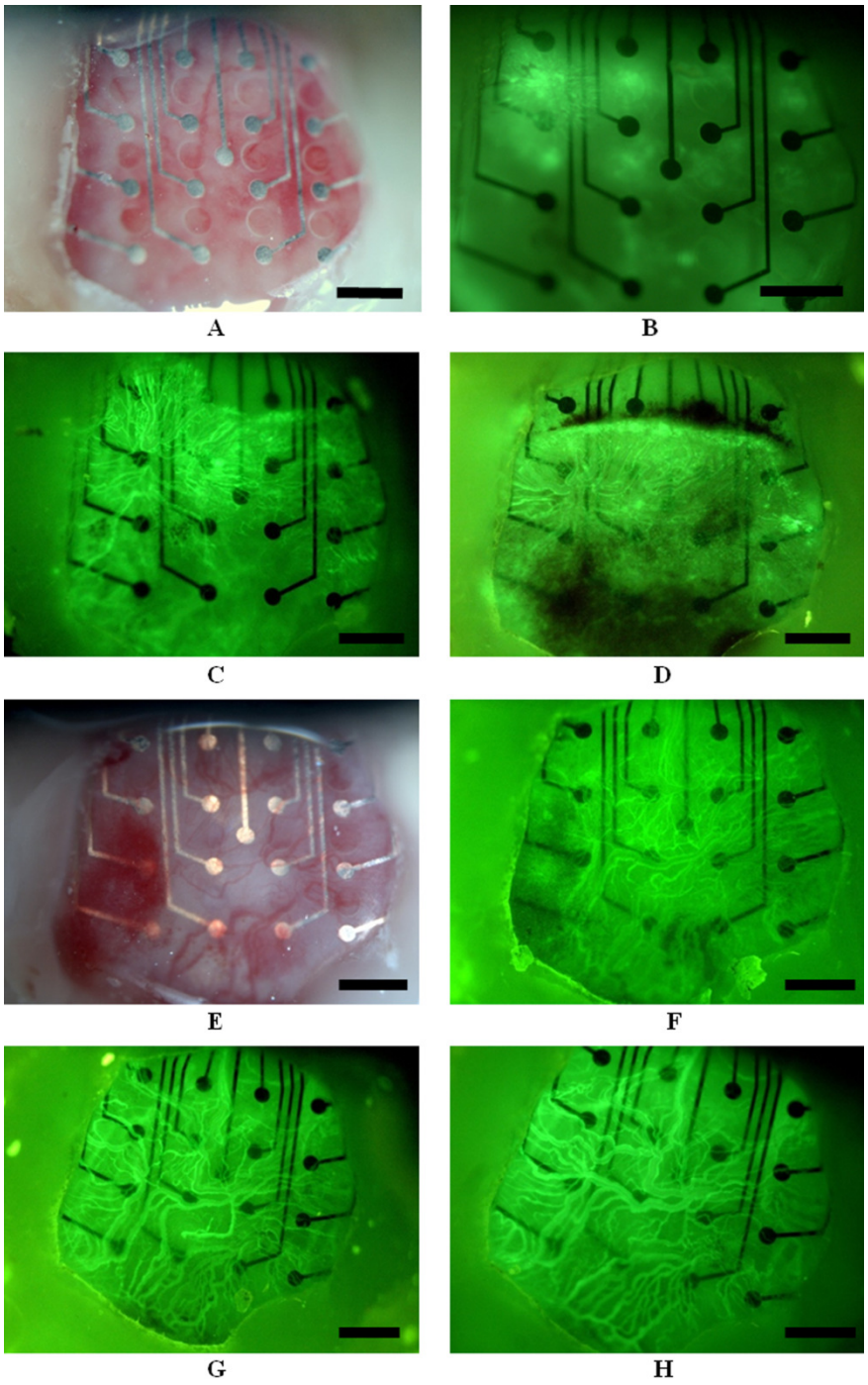

Figure 2.4. *In vivo* progression of vascular growth over an epidurally implanted micro-ECoG device. **(a)** 3 days post implantation. **(b)** 5 days post implantation. **(c)** 8 days post implantation. **(d)** 10 days post implantation. **(e)** 15 days post implantation. **(f)** 17 days post implantation. **(g)** 22 days post implantation. **(h)** 24 days post implantation. Scale bars represent 750 µm. At day 5 blood vessels begin to grow through

a hole in the upper left corner of the Parylene substrate. Over time, the vessels spread out over the entire top surface of the device. After 24 days, the vasculature seems to have stabilized, no more significant vessel changes occur after this point. Images in **(a)** and **(e)** were taken in bright field because the tail-vein injection of FITC-dextran was unsuccessful on those days.

Figure 2.5 shows examples of hematomas occurring in different animals at different time points after implantation. Generally, bleeds occurring within a few days of device implantation were more severe than those observed at later time points (15-20 days post implant). Most hematomas resolved themselves within one to two weeks, although some animals showed evidence of blood in the craniotomy for the duration of the experiment.

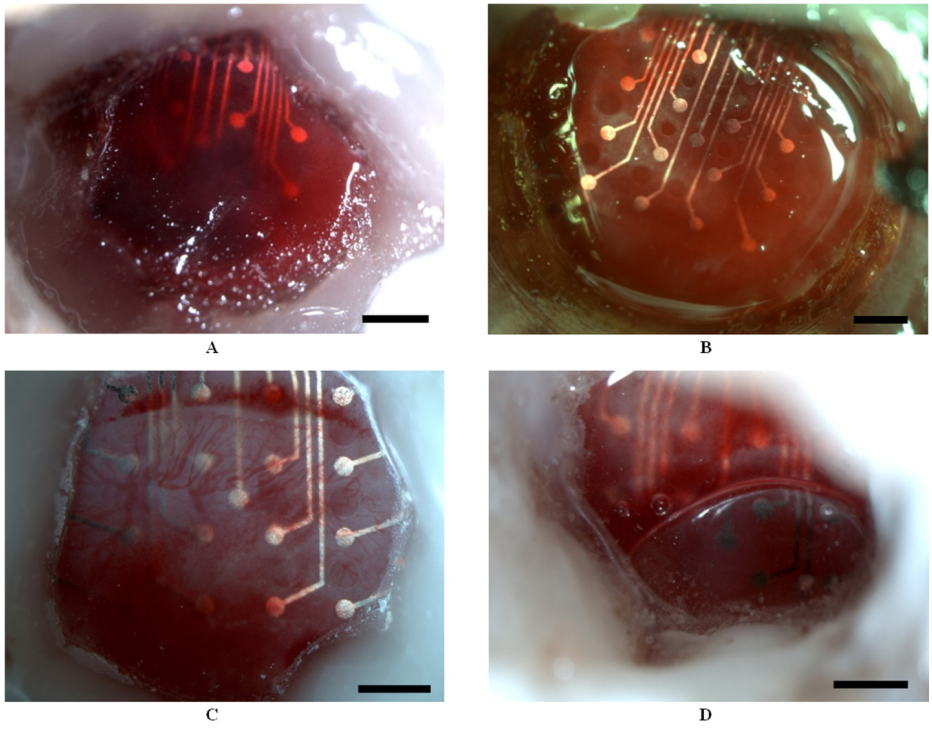

Figure 2.5. Micro-hematomas occurring in different animals at different time points after device implantation. **(a)** 2 days post implantation, **(b)** 3 days post implantation, **(c)** 15 days post implantation **(d)** 20 days post implantation. Scale bars represent 750 µm.

Animals were imaged for as long as their windows remained clear and the tissue vasculature was visible. In most cases this was for a period of one month. In some cases, however, the window was clear for longer than 2 months (Figure 2.6 (a) and (b)). In other instances, a white, highly neovascularized connective tissue grew between the micro-ECoG array and the window, obscuring the device (Figure 2.6 (c) and (d)). Upon removal of the brain from the skull after the animals had been euthanized, it was found that the connective tissue was mechanically solid when probed, which suggests that it is most likely ossified tissue or bone. This white tissue growth was found to occur anywhere from one to three weeks after implantation of the device.

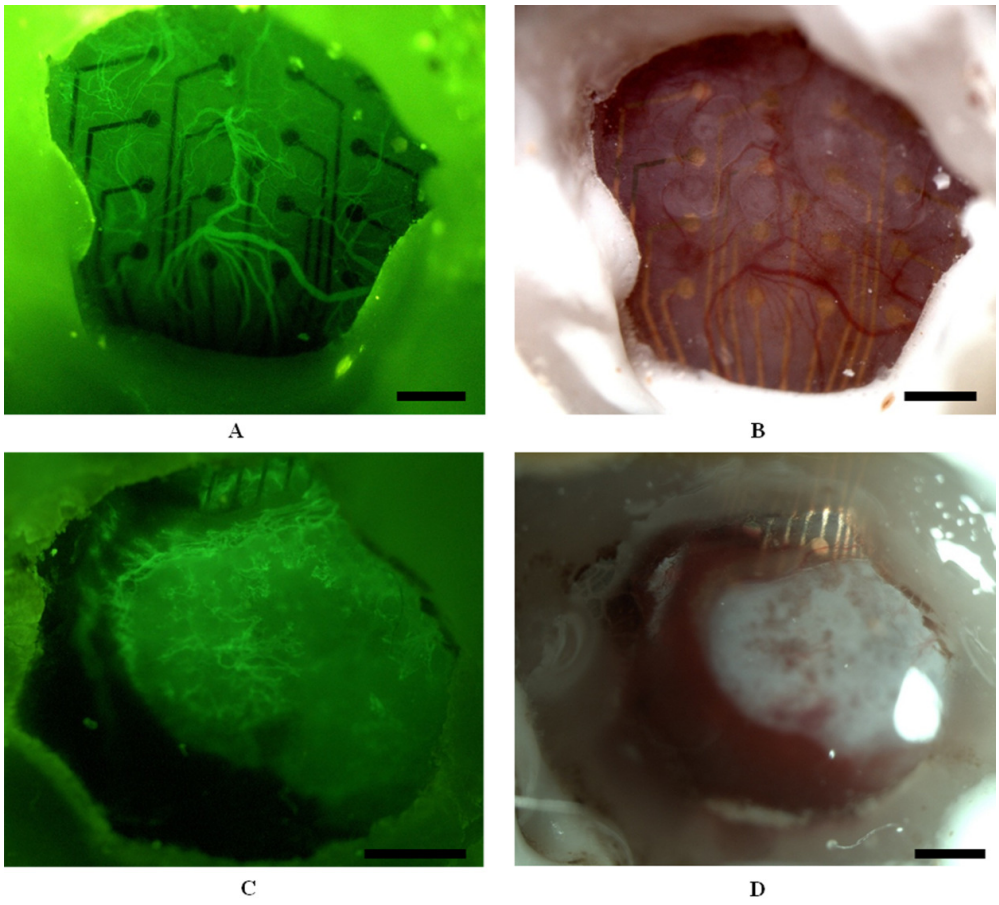

Figure 2.6. Cranial windows remain clear for varying lengths of time. **(a)** and **(b)** Images of the vasculature around a micro-ECoG device 2 months after implantation. **(c)** and **(d)** Images of the micro-

ECoG device 19 days after implantation. Scale bars represent 750 µm. Note the growth of opaque connective tissue over the majority of the cranial window.

Analysis of the data from the animals implanted with control windows revealed that white connective tissue began to form one week after surgery, even when there was no device present. Additionally, micro-hematomas were observed in each of the control animals at varying time points after the implantation procedure, just as in the animals implanted with micro-ECoG devices. The tissue response in an animal implanted with a control window can be seen in Figure 2.7.

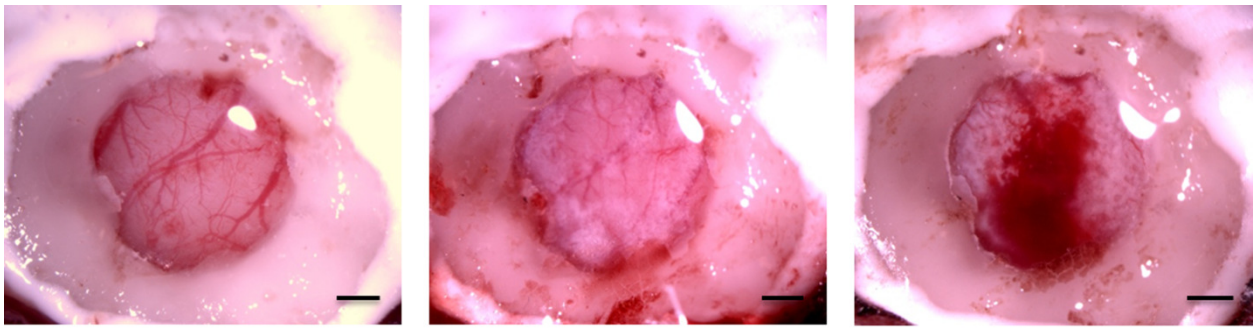

Figure 2.7. Tissue response to a control window. **(a)** 2 days post implantation. **(b)** 7 days post implantation. **(c)** 12 days post implantation. Scale bars represent one millimeter.

A comparison between the control window sitting directly on the dura-mater and that sitting up on the edge of the skull, such that it is not touching the dura-mater, is shown in Figure 2.8. It seems that, in both cases, the opaque white connective tissue formed beneath the cranial window, but in the case of the window sitting up on the edge of the skull, the tissue growth appeared to initiate from the bone edge, whereas, in the case of the window resting on the dura-mater, the reaction seemed to begin more towards the center of the window, away from the bone edge.

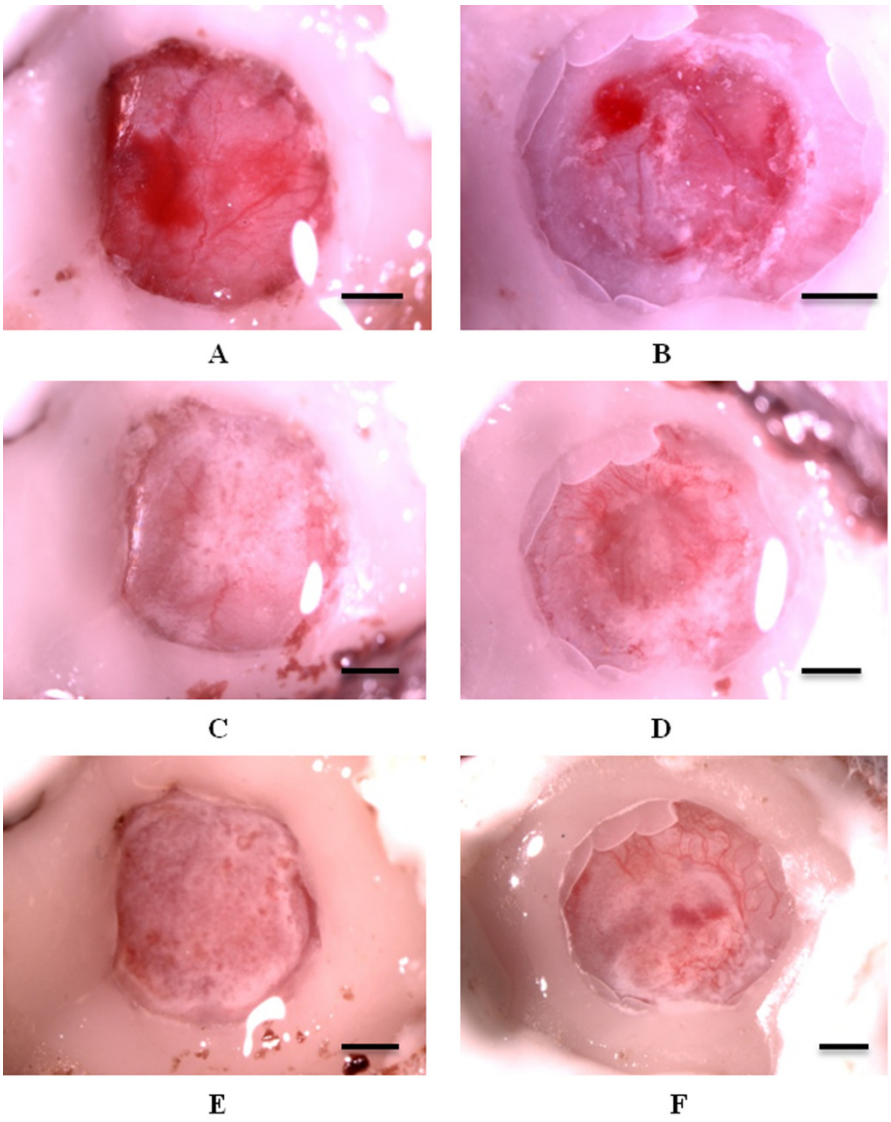

Figure 2.8. Normal control window vs. control window with edge sitting on skull. **(a)**, **(c)**, and **(e):** Normal control window 2, 7, and 14 days post implantation, respectively. **(b)**, **(d)**, and **(f):** control window with edge sitting on skull at 2, 7, and 14 days post implantation. Scale bars represent 1 mm.

Impedance Changes

Plots of the average change in impedance over time are shown in Figure 2.9 for both 1 kHz and 90 Hz frequencies. From these plots it is apparent that there is a general trend of a steep rise in impedance (between 150 and 300 kilo-Ohms) within the first 20 days after device implantation, after which the

impedance appears to plateau. This impedance change seems to be occurring within the same time period as the rapid tissue changes observed through the cranial window. The change in the impedance at a frequency of 1 kHz was analyzed in this experiment because the magnitude of the impedance at this frequency has been cited in the literature as a good benchmark for measuring overall tissue resistivity (Cui et al., 2001; Norlin et al., 2002; Williams et al., 2007). The impedance change at 90 Hz was analyzed because this frequency is within the range of physiologically relevant frequencies recorded by the micro-ECoG device, as local field potentials (LFPs) occur between 1 and 300 Hz. Both frequencies show a similar impedance trend.

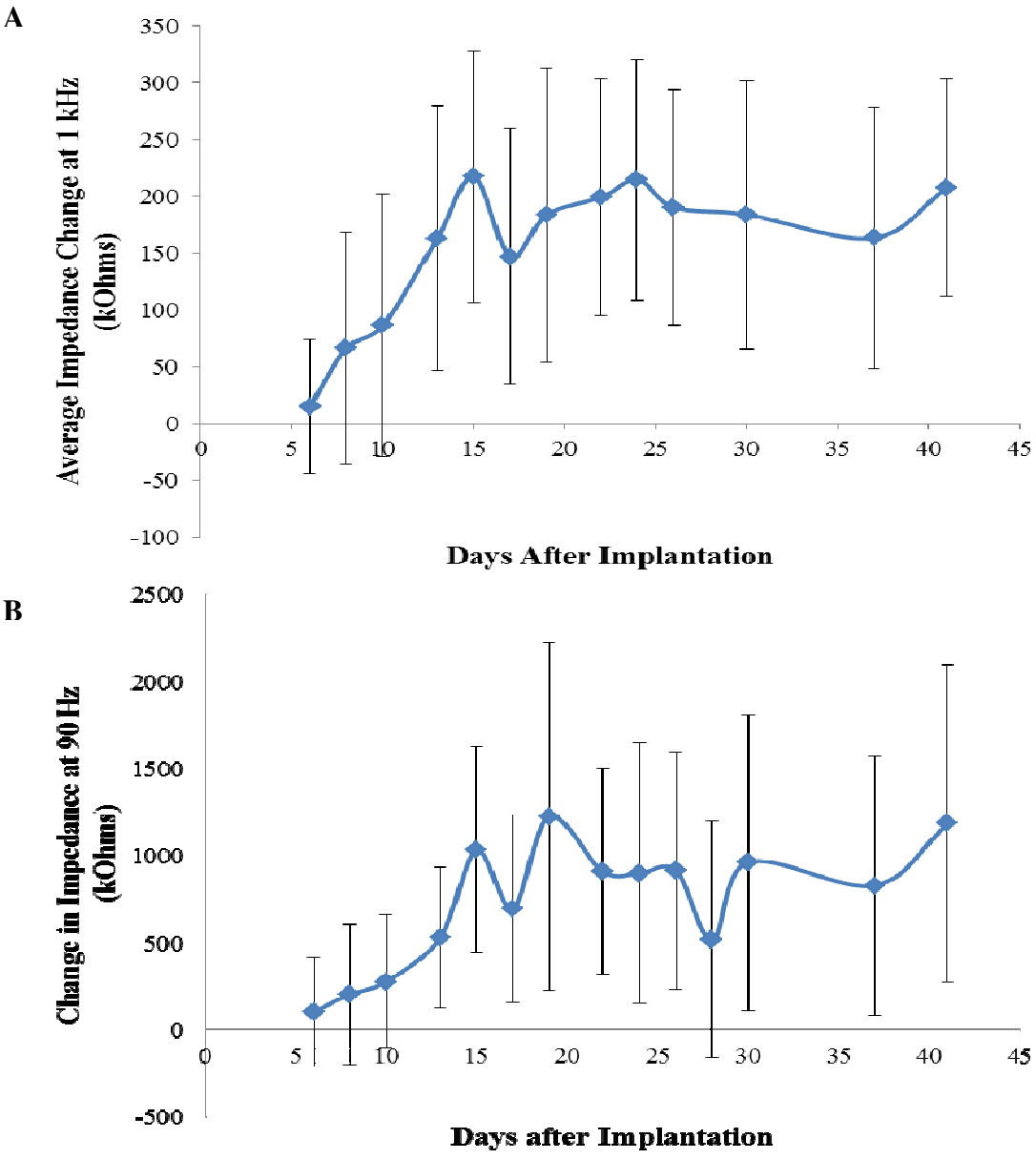

Figure 2.9. Impedance changes over time. Plot of average change in impedance (from initial impedance measurement after implantation) at 1 kHz (**a**) and 90 Hz (**b**) for four animals and all viable channels (60 channels) over time. Error bars represent +/- one standard deviation.

Histological Results

Histological analysis of the cortical vasculature after brain explantation revealed no significant vascular differences between brain regions away from the implantation site, brain regions beneath the control window, and brain regions beneath the micro-ECoG device (Figure 2.10).

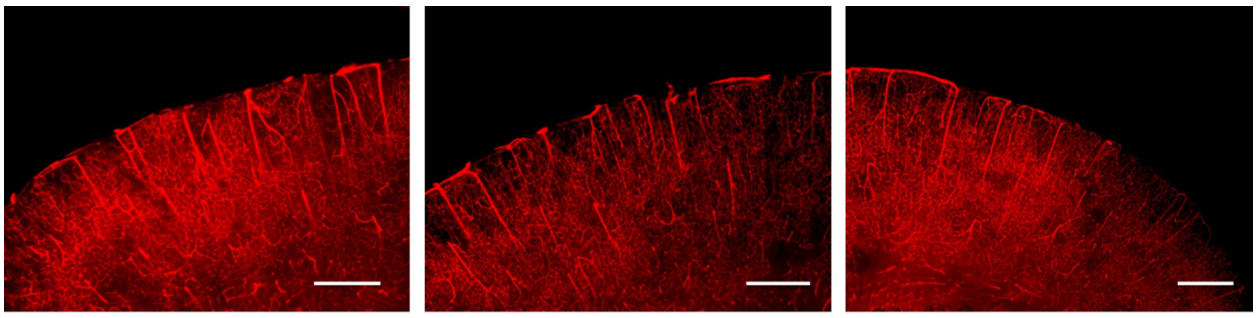

Figure 2.10. Cortical vasculature labeled with DiI in coronal brain sections. **(a)** Region away from implant. **(b)** Region beneath control window. **(c)** Region beneath Micro-ECoG device. Scale bars represent 500 µm.

Discussion

The goal of the current study was to develop a method for visualization of the tissue surrounding an implanted surface electrode array without disrupting the device-tissue interface. The cranial window imaging method proved very useful for this application. The majority of previous cranial window experiments have been carried out in mouse models and did not involve the use of implantable devices or devices placed on the cortical surface (Holtmaat et al., 2009; Trachtenberg et al., 2002). The mouse has been the preferred animal model for cranial window imaging because of the availability of many transgenic mouse strains which allow for the visualization of different cell types, including but not limited to microglia, astrocytes, and neurons. Additionally, because mouse bone is naturally thin and semi-transparent, a thin-skull preparation can be used, in which the cranial window is placed on top of a thinned layer of the skull, reducing the amount of trauma inflicted during surgery, yet still allowing the

brain tissue to be imaged (Drew et al., 2010; Marker et al., 2010). Discrepancies between the rat tissue response data reported in this paper and the findings from mouse cranial window imaging experiments could be due to a number of factors, including species differences, such as the skull and dural thickness, as well as experimental differences, such as the amount of dural trauma induced during surgery, the presence of the micro-ECoG device, and the duration over which the tissue response was monitored (Holtmaat et al., 2009). Although we are also working towards modifying the micro-ECoG arrays and the cranial window imaging method for a mouse model, the development of this technique for use in rats is beneficial for scaling up the dimensions of the micro-ECoG device towards the size that would be used in larger mammals and eventually in humans.

Administration of FITC-Dextran made it particularly easy to image the tissue vasculature; however visualization of different cell types is difficult with the current approach. Through use of the vascular imaging technique, rapid tissue changes were observed around the micro-ECoG devices following implantation, and we were able to track these changes over the course of the entire reaction cycle, after which the vasculature had stabilized. The observed tissue reaction was fairly consistent across all animals in the study, and the time-course of the rapid tissue changes seemed to align with the overall changes in the impedance, at both 1 kHz and 90 Hz frequencies. Although we are not correlating tissue changes and impedances around individual sites, there appears to be a general correlation between the overall device-level changes and the change in impedance. This is consistent with our previous results with penetrating devices that showed correlation between gross histological changes around implanted devices and their impedance at 1 kHz (Williams et al., 2007). Because there are many more factors involved in electrode site impedance than the vascular changes visualized in this experiment (Williams et al., 2007), more work is required to dissect the relationship between tissue growth and impedance at individual electrode sites.

Micro-hematomas were observed in every animal, including those implanted with control windows only, but the location of the hematomas and the time at which they occurred varied greatly. While the exact cause of these bleeds is unknown, a number of factors could have contributed to their

development, including irritation of the dural blood vessels during electrode placement, or shifting or swelling of the brain which resulted in increased pressure on the dural or cortical vessels due to the presence of the micro-ECoG device or the cranial window itself. Although the amount of brain shift which normally occurs in rats is quite minimal compared to that in primates, even pulsing of the brain from normal heart beat could be enough to irritate meningeal blood vessels, especially if those vessels were in contact with a sharp edge on the cranial window. Additionally, it is well known that in angiogenesis, the immature blood vessels are inherently leaky, due to the presence of vascular permeability factor (VPF), commonly referred to as vascular endothelial growth factor (VEGF), which is necessary to induce angiogenesis, but also results in a hyperpermeability of the newly formed vasculature (Dvorak et al., 1995). Whatever their cause, these hematomas could account for some of the changes in the electrode site impedance and the neural signals recorded from implanted brain devices (Vetter et al., 2004; Williams et al., 2007). Without the use of the cranial window imaging technique it would be almost impossible to detect these bleeds, due to their random and transient nature.

Growth of vascularized, opaque, connective tissue was observed in both the control animals as well as animals implanted with micro-ECoG devices. In some cases, the connective tissue formed below the micro-ECoG devices, while in others the tissue grew between the devices and the cranial window. The formation of new blood vessels as well as this connective tissue, even in the animal which was implanted with a control window that was not in contact with the dura mater (Figure 2.8), suggests that a tissue reaction occurs merely as a result of surgical trauma, and that no cortically implanted electrode array can be considered free from biological response (Xu et al., 2007). More investigation is necessary to determine the composition of the tissue and why it grows beneath the micro-ECoG device in some cases and above the device in others. At this point, it is postulated that this tissue formation is either in response to irritation of the dura mater or is a result of bone re-growth. The initiation of the connective tissue growth from the center of the craniotomy in some of the control cases was not unexpected, as the formation of "bony islands" in the center of cranial defects has been reported by several groups studying bone regeneration (Aronin et al., 2010; Levi et al., 2011; Oyama et al., 2010; Sohn et al., 2010).

Additional histological studies comparing tissue re-growth in animals implanted with control windows to that in animals with no windows implanted may be useful in determining the extent of the tissue response that can be attributed to the presence of the cranial window.

It was initially unclear how the presence of the device would affect the ability to image the cortical tissue. However, it was found that the Parylene substrate was sufficiently transparent to allow us to view the vasculature beneath the electrode array for the first few days after implantation (before vessels grow on top of the device and obstruct the view below). Figure 2.11 shows an example of vessels imaged beneath the micro-ECoG device. It was also postulated that, due to its hydrophilic nature, the electrode array could potentially stick to the glass surface instead of to the cortex, preventing some of the recording sites from contacting the neural tissue and precluding the growth of tissue around the entire device. The finding that the vasculature grows on top of the device, between the glass and the Parylene substrate, suggests that this was not the case.

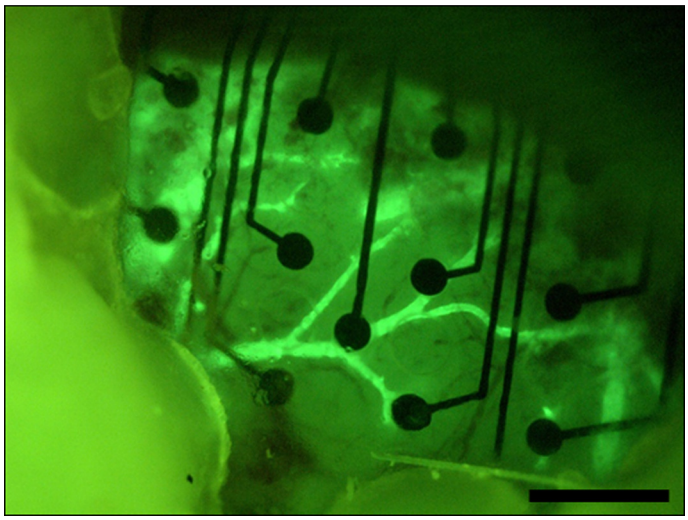

Figure 2.11. Vasculature beneath the array. Blood vessels visible beneath the micro-ECoG device two days after implantation. Scale bar represents 750 µm.

Although, the observed neovascularization was similar to that reported by Arieli et. al from their studies in monkeys (Arieli et al., 2002) and was, to some degree, expected, the growth of blood vessels

through the holes in the substrate of the device was not anticipated. These holes were originally incorporated into the device design for the purpose of inserting other types of neural probes through the micro-ECoG and into the cortex; however, the presence of the holes seemed to encourage tissue growth on top of the device. It is postulated that this may inhibit thickening of the dura mater and other tissues below the device, at the electrode-tissue interface, in turn helping to bolster recorded signal quality and longevity. Thus, a logical next step would be to investigate the effects of the Parylene substrate footprint on tissue growth around micro-ECoG devices. Additionally, since it is known that immature blood vessels are prone to leakage, it may be useful to explore the effects of anti-angiogenesis drugs applied at the implantation site on the tissue response to the micro-ECoG device and on the recorded signal quality (Brown et al., 1992). Small molecule inhibitors, such as thalidomide, are commonly used for angiogenesis prevention (Mabeta and Pepper, 2011; Segler and Tsimberidou, 2012).

It is important to note that the tissue reactions to the micro-ECoG devices studied in this experiment may not be directly comparable to the clinical ECoG grids currently used in humans. Current clinical grids consist of varying numbers of channels with a general spacing of 1 centimeter (cm) between sites and a general electrode site diameter of around 5 mm (Leuthardt et al., 2004). These grids are designed for mapping epileptic foci rather than brain computer interfacing applications, and thus require less spatial resolution. In addition, clinical ECoG arrays are not meant for long term implantation. They are generally only left in place long enough to determine the origin of a patient's seizures. Consequently, tissue integration may not be desirable in the case of these macro grids.

The purpose of this study was to determine the tissue response to micro-ECoG devices for brain computer interfacing applications, since these devices must be designed for long-term reliability *in vivo*. In the case of micro-electrode arrays for BCI applications, integration of the device and tissue may help to anchor the array in place, and thus minimize micro-motion which could potentially result in cortical trauma and signal instability. Therefore, the angiogenesis and overall tissue response observed in these window experiments could potentially prove to be therapeutic in the case of surface electrode arrays (Murphy et al., 2004). That being said, there have been some recent efforts to utilize micro-ECoG for

human seizure detection (Stead et al., 2010), and the electrodes used in this study may prove clinically useful for this application, as the tissue in-growth could serve to stabilize the brain-electrode interface. It is not yet known what kind of damage would occur upon removal of the devices, but it may prove to be minimal, as the in-growing vessels are quite small. Evidence of similar small vessel damage has been found upon removal of macro-ECoG grids (Fong et al., 2012), and is well tolerated.

The cranial window imaging method has proven to be a useful tool for understanding the behavior of tissue surrounding implanted electrode arrays, but there are some limitations to this technique. Perhaps the most significant limitation is that we can very clearly image the tissue growing on top of the array, but cannot see what is occurring beneath the electrodes, at the electrode-tissue interface. In order to determine what is going on at the site of the neural recordings, other imaging techniques, such as traditional histological methods or multi-photon microscopy, which can penetrate more deeply into the tissue, would be necessary. Histological analysis of the cortical vasculature of the animals used in this study revealed no significant differences between the vasculature directly beneath the micro-ECoG device and that below the control window or away from the implantation site altogether. This finding corroborates the theory that the majority of the tissue reaction to these surface electrode arrays is occurring in the meninges. However, the current setup is limited to observing the tissue vasculature, and further investigation is necessary into the response of different cell types, such as astrocytes and microglia. Although not apparent in the still photos, individual cells were visible through blood flow video recordings, suggesting that this technique could be easily modified to view individual cell types with the use of appropriate fluorescent dyes and transgenic animals. One additional shortcoming of this technique is that the presence of the cranial window itself appears to initiate a tissue response. Further histological comparison studies will be necessary in order to determine the time-course of the tissue response to the micro-ECoG device with and without the presence of the cranial window.

The cranial window imaging method provides insight into the transient changes occurring at the surface of the brain. Future studies, which incorporate the window imaging method in conjunction with electrophysiological recordings and supplementary imaging modalities, will help increase the

understanding of why these tissue changes occur and how they correlate with variations in electrophysiological data.

Conclusion

The cranial window imaging method has proven a useful technique for monitoring the tissue response to surface electrode arrays *in vivo*. Use of this technique has revealed the presence of micro-hematomas around every implanted device, but at varying time points. These hematomas could be contributing to changes in the recorded signal over the course of the implant lifetime, and would not be observable using traditional histological techniques. Moving forward, additional studies are necessary in order to determine the effect of the device substrate footprint on the tissue response, as well as to adapt this technique for visualization of different cell types and determine the relationship between cortical tissue changes and recorded signal quality.

3 MICRO-ECOG SUBSTRATE FOOTPRINT COMPARISON

Abstract. There is great interest in designing implantable neural electrode arrays that maximize function while minimizing tissue effects and damage. Although it has been shown that substrate geometry plays a key role in the tissue response to intracortically implanted neural interfaces, there has been minimal investigation into the effect of substrate footprint on the tissue response to surface electrode arrays. In this study, the cortical tissue response to two micro-electrocorticography devices with differing geometries was evaluated. The first device had each electrode site and trace individually insulated, with open regions in between, while the second device had a solid substrate, in which all sixteen electrode sites were embedded in a continuous insulating sheet. These devices were implanted bilaterally in rats, beneath cranial windows, through which the meningeal tissue response was monitored for one month after implantation. Electrode site impedance spectra were also monitored during the implantation period.

It was observed that collagenous scar tissue formed around both types of devices. However, the distribution of the tissue growth was different between the two array designs. The data suggests that an open architecture device would be more ideal for neural recording applications, in which a low impedance path from the brain to the electrode sites is critical for maximum recording quality.

Introduction

Due to the extended time periods over which they must be implanted, microelectrode arrays (MEAs) for brain computer interfacing (BCI) applications must be designed for long-term reliability *in vivo*. One approach to creating more reliable MEAs has been to alter the substrate geometry. Previous studies have shown that devices with a more open architecture elicit a smaller inflammatory response than devices with solid substrates (Seymour and Kipke, 2007), presumably due to the open architecture devices having less foreign material present and allowing for diffusion of soluble factors from one side of the device to the other (Kim et al., 2007; Seymour and Kipke, 2007). These studies, however, have been performed on MEAs which penetrate the cerebral cortex. Recently, the finding that these types of

penetrating arrays can cause significant glial scarring, which often results in a degradation of signal quality (Schwartz et al., 2006), has led to a push towards less invasive surface electrode arrays, such as the micro-electrocorticography (micro-ECoG) device (shown in Figure 3.1(a)) (Henle et al., 2011; P. Ledochowitsch et al., 2011; Thongpang et al., 2011; Viventi et al., 2011). Micro-ECoG devices have shown great promise due to their flexibility, substrate transparency, recording longevity, and improved signal information (Richner et al., 2014; Thongpang et al., 2011; Viventi et al., 2011; Williams et al., 2013), but further studies need to be done to test which type of micro-ECoG design gives maximum function with minimal inflammation. In particular, the impact of the footprint of these devices on the tissue response has not been previously examined.

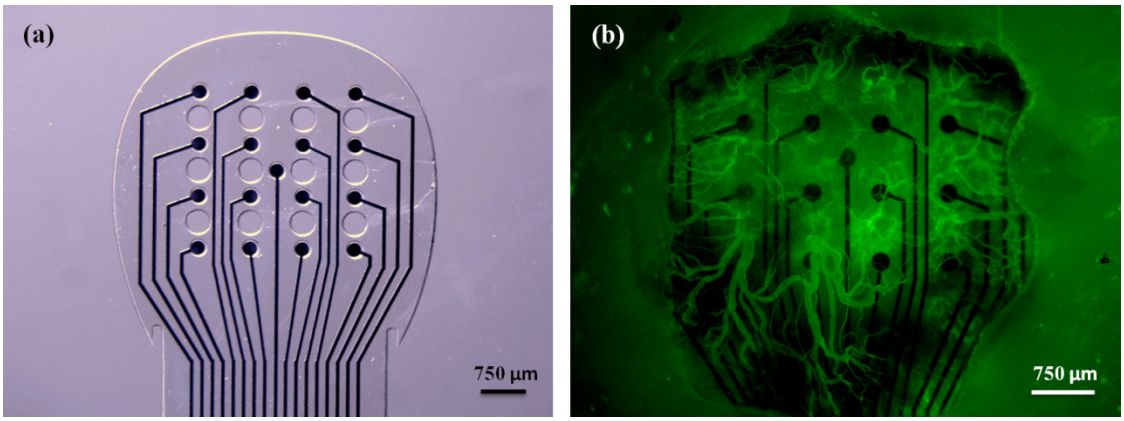

Figure 3.1. Fenestrated micro-ECoG array used in previous imaging studies. **(a)** Fenestrated micro-ECoG device used in previous cranial window imaging studies. Note the holes through the Parylene substrate (in between the electrode sites). **(b)** *In vivo* image of vascular growth around a fenestrated micro-ECoG device 30 days after implantation. Taken using a Leica MZ 16F fluorescent stereoscope with a GFP2 filter and broad spectrum light. Animal was injected with 6 mg of FITC-Dextran in 0.5 ml saline, to promote vascular fluorescence.

Although it has been generally assumed that cortical surface arrays do not elicit a significant biological response, our former study has revealed substantial vascular changes occurring around the

implanted devices (Schendel et al., 2013). In this study, micro-ECoG devices were implanted beneath cranial windows, enabling long-term *in vivo* imaging of the cortical tissue response and observation of delicate interfacial tissues that are often destroyed during traditional histological analyses. It was discovered that new blood vessels grew up through holes in the micro-ECoG device and spread laterally over the entire top surface of the array, as seen in Figure 3.1(b). This finding, and the previous findings that devices with less substrate may cause a more minimal tissue response, led to further questions about how the tissue response to the micro-ECoG device would compare to the tissue response to clinical ECoG devices, which do not have holes through the polymer substrate. In addition, these results prompted questions regarding how the surrounding tissue would respond to a surface electrode array with less substrate, in comparison to a device with more substrate material.

In this study, animals received bilateral micro-ECoG implants beneath cranial windows. On one hemisphere of the brain, a "mesh" micro-ECoG device was implanted, which had each electrode site and trace individually insulated, with open space in between the traces. The term "mesh" has been coined by Kim et al to describe a similar open architecture neural surface electrode (Kim et al., 2010), and so will be used throughout this paper to describe our minimal substrate array. On the other hemisphere, a solid micro-ECoG device was implanted, which had no holes through the Parylene substrate, similar to the layout of a clinical ECoG grid. The vascular response to each device was monitored over the entire implantation period by imaging through the cranial windows with a fluorescent microscope. Traditional histological techniques as well as optical coherence tomography (Huang et al., 1991) and second harmonic generation imaging (Campagnola et al., 2002) were used in conjunction with *in vivo* stereo fluorescence microscopy to further analyze the tissue growth around the implanted devices. In addition to the tissue response, the electrode site impedances were also compared between the two types of devices (solid vs. mesh), to evaluate the effect of the device geometry on its recording capabilities. The results of this experiment will aid in determining the ideal geometry for cortical surface microelectrode arrays, in terms of biocompatibility and signal stability.

Methods

Device and Fabrication

Micro-ECoG devices were fabricated following the protocol described previously (Schendel et al., 2013; Thongpang et al., 2011). In this case, since two electrode arrays were to be implanted in a single animal to allow for direct comparison, both the mesh and the solid micro-ECoG devices were affixed to a single printed circuit board (PCB) connector, with the mesh device on one side of the connector and the solid device on the other side (Figure 3.2). Since the brain hemispheres are relatively symmetrical in terms of anatomy and function, implanting these arrays on the left and right hemispheres, respectively, should not have a confounding effect on the electrode site impedance spectra or on the tissue response to the devices.

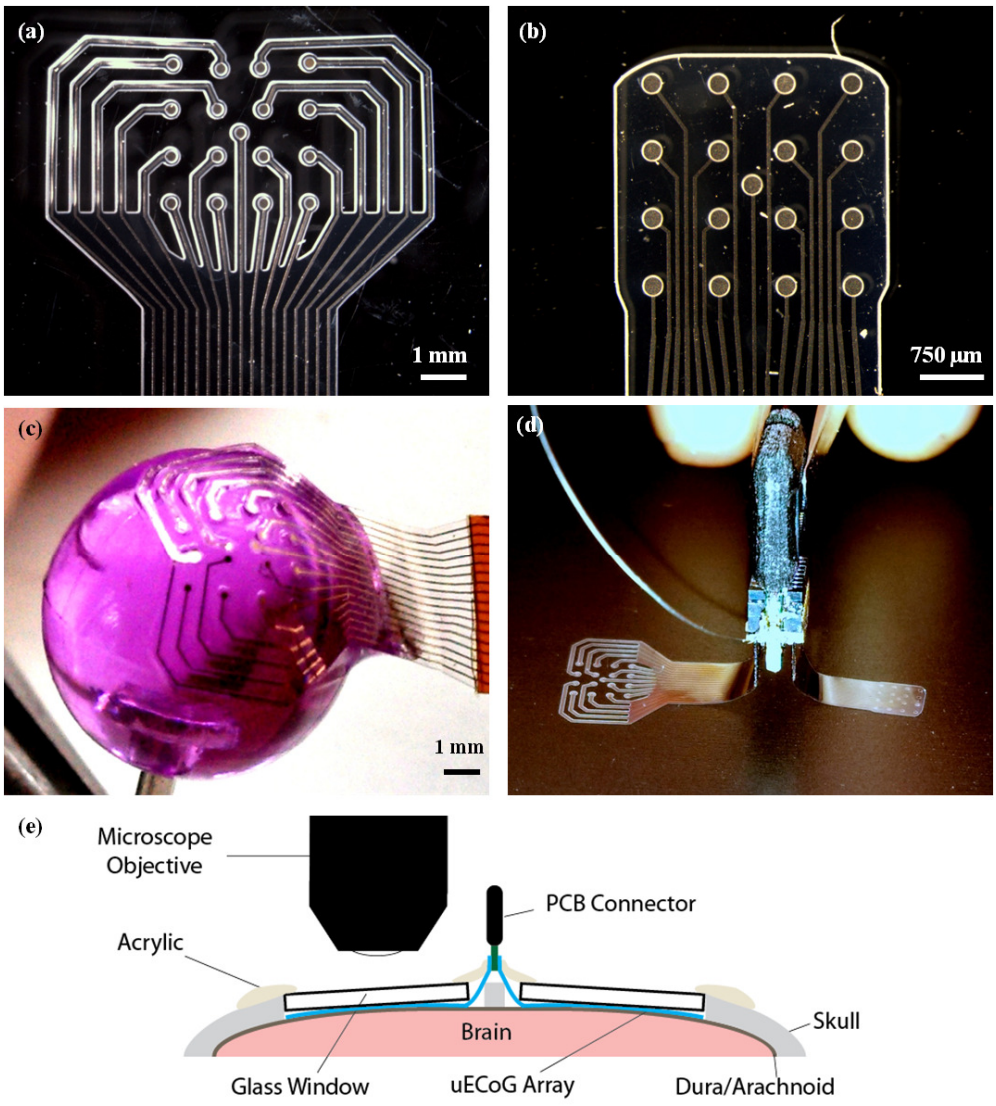

Figure 3.2. Electrode array designs and implantation layout. **(a)** Mesh micro-ECoG device. **(b)** Solid micro-ECoG device. **(c)** Demonstration of the flexibility of the mesh micro-ECoG array. The device is adhered to the head of a thumbtack. The tack head was dipped in water and the hydrophilic nature of the substrate allowed it to conform to the rounded surface. **(d)** Bilateral device with mesh and solid micro-ECoG arrays attached to a single PCB connector, as was implanted in each animal. **(e)** Cross-sectional schematic diagram of the implantation layout.

The layout of the solid micro-ECoG device was identical to that of the standard, fenestrated micro-ECoG array reported previously (Schendel et al., 2013), except that there were no holes through the Parylene substrate. In the mesh device, since each individual trace was insulated separately and enough insulation was required to create a tight seal around the traces and electrode sites, the total size of the array, in terms of the surface area of cortex it would cover, was larger than that of the fenestrated and solid micro-ECoG devices. However, the areal density, or the ratio of the amount of material touching the brain to the total surface area the device covers, was much smaller (Table 3.1). Additionally, in order to make room for the extra insulation material, the spacing between sites on the mesh device was 1 mm, as compared to 750 μm in the other two devices. Since this experiment was not concerned with comparing the spatial behavior of the signals recorded by the two types of devices, the difference in electrode site spacing does not impact the results.

Table 3.1. Summary of surface area data for mesh, solid, and fenestrated Micro-ECoG devices.

Device Type	Total Area In Contact with Brain (mm^2)	Total Implantation Area (mm^2)	Areal Density
Mesh	11.09	29.42	38%
Fenestrated	7.84	8.53	92%
Solid	8.53	8.53	100%

Ethics Statement

All animal procedures were approved by the Institutional Animal Care and Use Committee (IACUC) at the University of Wisconsin - Madison. All efforts were made to minimize animal discomfort.

Surgical Implantation

Male Sprague Dawley rats (n = 6) received bilateral implants, with the mesh micro-ECoG device on one hemisphere of the brain and the solid micro-ECoG array on the other hemisphere. A schematic of the implantation layout is shown in Figure 3.2(e). The surgical implantation procedure followed that described in the previous cranial window imaging paper (Schendel et al., 2013). Briefly, the rats were anesthetized with isoflurane gas, and received subcutaneous injections of buprenorphine hydrochloride (0.05 mg/kg, Reckitt Benckiser Healthcare Ltd) for pain management and dexamethasone (2 mg/kg, AgriLabs) to prevent brain swelling. Craniotomies were made on both hemispheres of the skull with a #107 engraving tool. Using a hand drill and a #56 drill bit, holes were drilled through the skull for the placement of screws, to which wires were connected from the PCB connector of the device, to act as ground and reference. The micro-ECoG device was affixed to a micro-manipulator and stereotactically lowered onto the surface of the brain, with the mesh device in one craniotomy, the solid device in the other, and the connector in the middle, along the sagittal suture. After the devices were in place, cranial windows were positioned over the top of each device. Due to the larger surface area of the mesh micro-ECoG, an 8 mm diameter glass coverslip was used to form the cranial window, so that the full array was within the viewing area, while a 5 mm diameter glass coverslip was used in the case of the solid micro-ECoG array. Both coverslips had a thickness of 0.15 mm. Once the cranial windows had been placed on the devices, small pieces of Gelfoam (Pfizer Injectables) were arranged in any gaps between the edges of the craniotomies and the glass coverslips, and then UV curable dental acrylic (Fusio, Pentron Clinical) was applied to seal the coverslips to the skull. Next, the ground and reference screws and wires, as well as the electrode neck and base of the connector were covered in dental acrylic to form a smooth cephalic implant. The skin was then sutured around the cephalic implant, and the animal was revived and allowed to recover. After surgery, animals received additional doses of buprenorphine and dexamethasone, for pain management, as well as ampicillin (50 mg/kg, Sage Pharmaceutical) injections, twice daily, for one week, to prevent infection.

Vascular Imaging

Animals were imaged biweekly for at least one month after device implantation, or for as long as the cranial windows remained clear. For each imaging session, animals were anesthetized with a combination of dexmedetomidine (0.05-0.5 mg/kg, Orion Pharma) and 1% isoflurane gas. To minimize breathing artifacts, the rats were held in a stereotactic frame using ear bars, after application of 2% topical lidocaine ointment to the inner ear. An upright fluorescent stereoscope (Leica MZ 16F, Leica Microsystems) was used to image the tissue response to the implanted electrode arrays. Fluorescein isothiocyanate labeled dextran (30 mg/kg, average molecular weight 2,000,000, Sigma Aldrich product #52471) was injected via the tail vein in order to enhance the ability to visualize the vasculature, by causing the vessels to be fluorescent under blue light. Both bright field and fluorescent images of the cortical tissue response were captured. In addition, blood flow was visible with the aid of the FITC-Dextran injections, and thus some blood flow videos were also recorded. After the imaging session was complete, the animals were taken off the isoflurane and received subcutaneous injections of atipamezole hydrochloride (0.3 mg/kg, Orion Pharma) to reverse the dexmedetomidine anesthesia.

Impedance Spectra and Baseline Signal Recording

Impedance spectra were taken for each electrode site on the same days on which the vasculature was imaged (Williams et al., 2007). Impedance spectrum data was collected using a potentiostat (Autolab PGSTAT12). Real and imaginary impedance values were evaluated at 30 different frequencies, from 10 Hz to 30,937 Hz, using a two-electrode method with the bone screws implanted in the skull acting as the ground. Animals were awake and behaving for the collection of the electrode site impedance spectra.

Histological Analysis and OCT Tissue Thickness Quantification

After data collection was complete, animals were euthanized by cardiac perfusion, following the protocol outlined by Li et al, in which a lipophilic1,1′-dioctadecyl-3,3,3′,3′-tetramethylindocarbocyanine perchlorate (DiI) solution was injected transcardially during the perfusion, in order to fluorescently label

the tissue vasculature (Li et al., 2008). Once perfused, the brains were dissected and sliced into 200 µm thick cortical sections using a vibratome (Leica VT1200). Microscope slides of the tissue samples were then prepared following the procedure described in the Li protocol (Li et al., 2008). The slides were imaged under green (541-551 nm) light, since this is the excitation wavelength of the DiI. The Leica fluorescent stereoscope described above was used for analysis of the cortical slices.

In addition to examination of the cortical vasculature, histological evaluation of the scar tissue surrounding the micro-ECoG devices was also necessary. After brain removal, bright field and fluorescent images were taken of the underside of the skull, where the electrodes were affixed. After this initial evaluation, the electrode and surrounding tissue were cut away from the skull and cranial window, for histological analysis. The samples were then imaged using second harmonic generation (SHG) with a Prairie Ultima Intravital Multiphoton microscope (Prairie Ultima IV, Prairie Technologies). All SHG images were collected at an excitation wavelength of 890 nm with a Zeiss 20x 1.0NA Plan-Apochromat Water objective (WD 1.7) and a narrow band SHG filter (445/40, Chroma) to isolate the SHG signal from background fluorescence. This method allowed for the determination of whether a collagen signal was present in the tissue surrounding the devices (Provenzano et al., 2009). Following SHG imaging, select tissue samples were sectioned and stained with hematoxylin and eosin (H&E), to determine the tissue morphology.

It was also desired to quantify the thickness of the tissue that had grown both above and below the implanted devices. Since traditional histological methods involve the use of alcohols, which dehydrate the tissue, causing non-uniform shrinkage, it was necessary to find a different, high-resolution method for thickness quantification. Ultimately, optical coherence tomography (OCT) was chosen, due to its ability to quickly and non-destructively image the device-tissue interfaces and produce a cross-sectional view through the entire sample (something that was not possible using SHG optical sectioning, due to the large sample thicknesses). A custom spectral domain OCT (SD-OCT) system (1300 nm wavelength, 200 nm source bandwidth) was used for this application. Two-dimensional cross-sectional images were taken of

each electrode/tissue sample, and the thickness of the tissue above and below each device was measured in a minimum of three positions per animal, and averaged.

Results

Chronic in vivo Imaging Results

The progression of tissue growth around mesh and solid devices in one representative animal is shown in Figure 3.3 Column (a) shows images taken of the mesh micro-ECoG device, in bright field microscopy. Column (b) shows the solid micro-ECoG device in bright field. Columns (c) and (d) display fluorescent images of the mesh and solid devices, respectively. Note the formation of opaque, fibrous tissue around the mesh device only one week after implantation. This tissue appears to be initially avascular, but as it continues to thicken around the device, a vasculature forms, as can be seen in Figure 3.3, Day 28. In Figure 3.3(b), the white areas around and below the device on day 2 are not tissue growth, but remnants of bone from the drilling of the craniotomy, which became trapped beneath the micro-ECoG device during implantation. In the case of the solid device, the opaque, white tissue appears to thicken beneath the device for a few days before beginning to wrap around the edges of the device and spread onto the top surface.

In one animal, an accidental tear in the dura occurred on the hemisphere on which the mesh electrode array was implanted, as a result of the implantation surgery. It was discovered that the opaque, fibrous tissue formed only in the regions of the window in which the dura mater was intact, as shown in Figure 3.4. Since portions of this animal's window remained clear due to the dural tear, the animal was imaged for over one year after implantation of the devices. Even 419 days after implantation, the scar tissue had not completely encapsulated the device, and regions of the cerebral cortex were still visible, as shown in Figure 3.4(c) and (f).

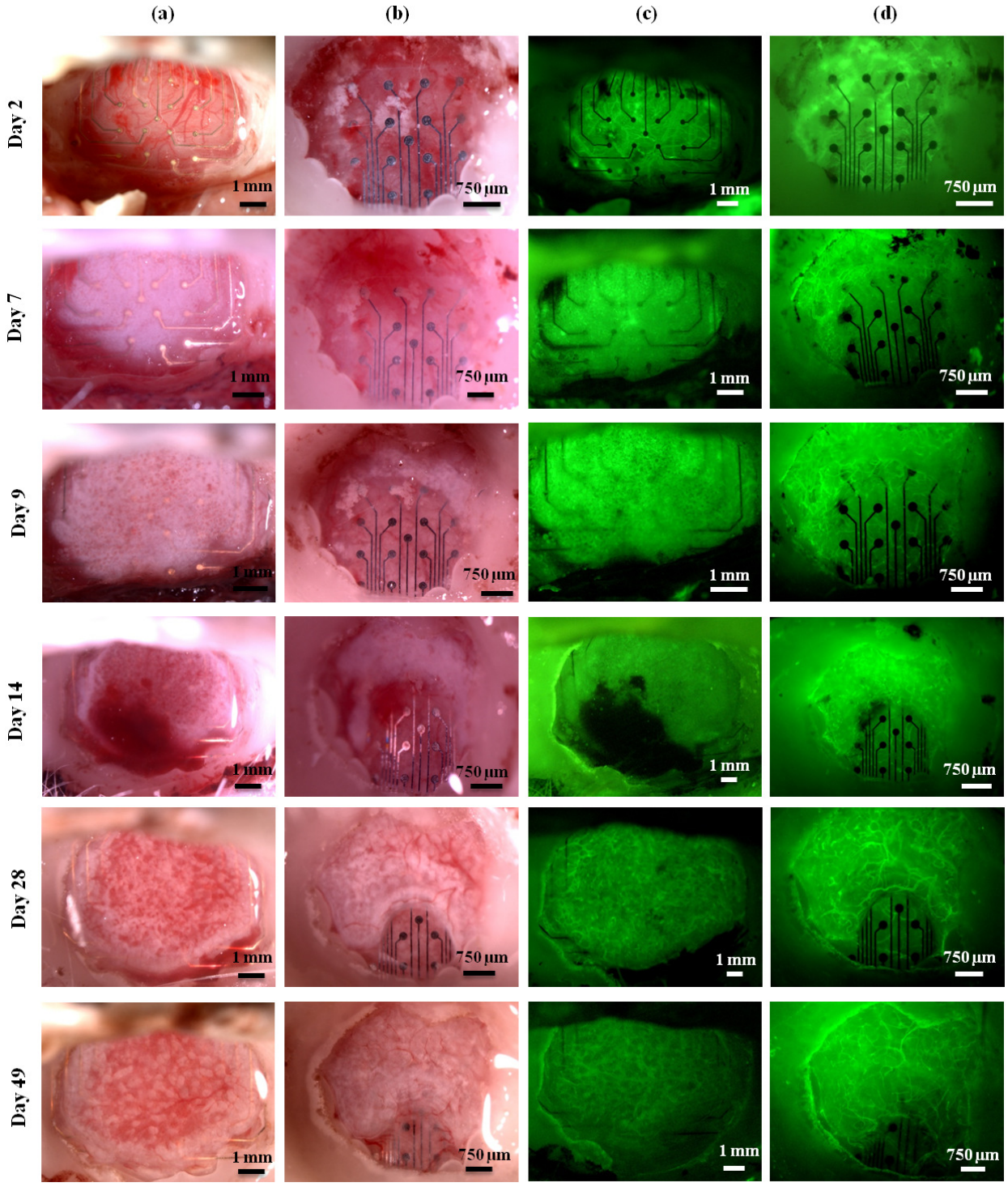

Figure 3.3. The progression of tissue growth over time for mesh an solid devices. Columns **(a)** and **(b)** contain bright field images of the mesh and solid devices, respectively. Columns **(c)** and **(d)** contain

fluorescence images of the mesh and solid devices, respectively. Images shown are for mesh and solid devices implanted in a single animal.

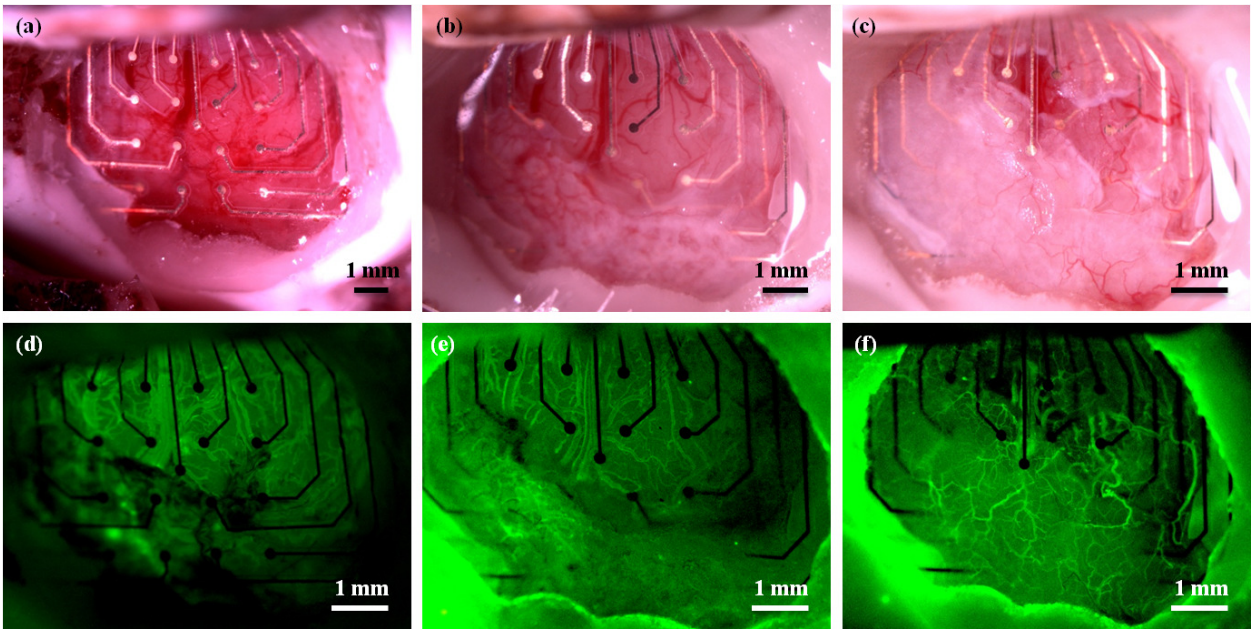

Figure 3.4. Images of a mesh electrode implanted in an animal with a dural defect. **(a)** Bright field image 1 day after implantation. **(b)** Bright field image 45 days after implantation. Note the formation of opaque, white tissue in the dural regions, but not in the area where the dura was removed. **(c)** Bright field image 419 days post implantation. **(d)**, **(e)**, and **(f)** Fluorescence images 1, 45, and 419 days post implantation, respectively.

Scar Tissue Characterization

Transcardial perfusion with DiI solution was used to fluorescently label the cortical vasculature for *ex vivo* analysis. Figure 3.5 shows fluorescent and bright field images of the electrodes and surrounding tissue in the same animal represented in Figure 3.3. Figure 3.5(b) and (c) are images taken of the underside of the mesh device, after brain removal, while Figure 3.5(e) and (f) are images taken of the underside of the solid device after brain removal. From these images, it is apparent that the mesh

electrode sites are much more clearly visible than the electrode sites on the solid array, suggesting that more tissue has formed beneath the solid array than beneath the mesh.

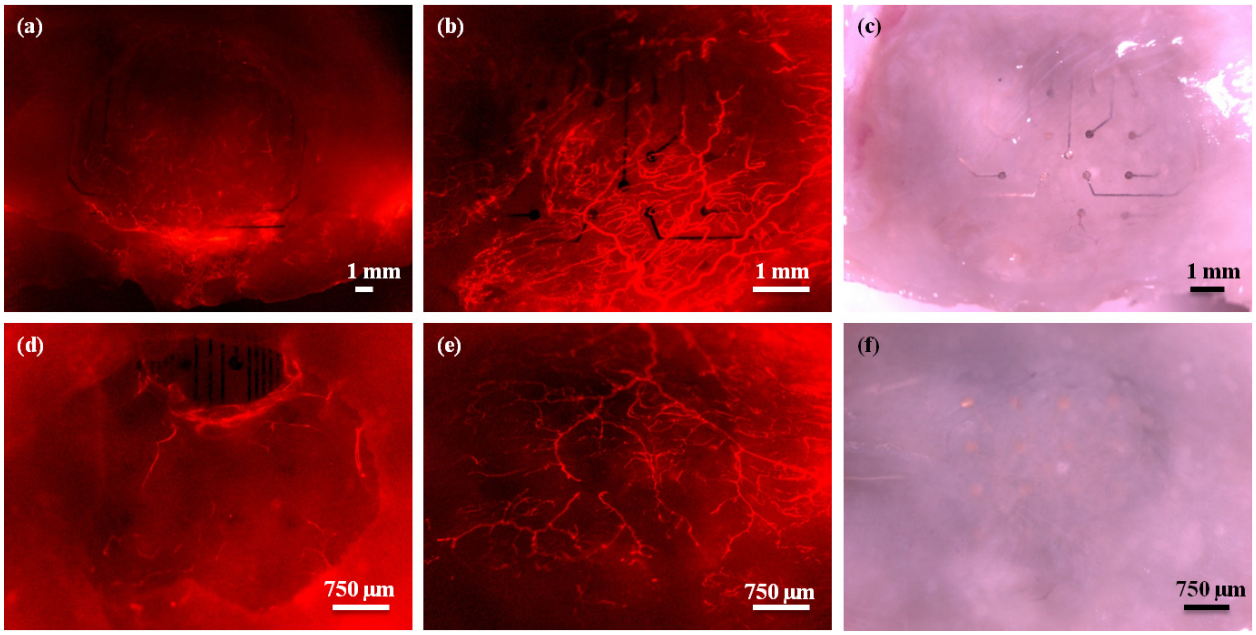

Figure 3.5. Electrodes and surrounding tissue in one animal after perfusion with DiI to stain the tissue vasculature. **(a)** Fluorescence image of the mesh device through the cranial window. **(b)** Fluorescence image of the underside (the region in contact with the cortex) of the mesh device after brain removal. **(c)** Bright field image of the underside of the mesh device. **(d)** Fluorescence image of the solid micro-ECoG device through the cranial window. **(e)** Fluorescence image of the underside of the solid device after brain removal. **(f)** Bright field image of the underside of the solid micro-ECoG device. Note that the electrode sites are clearly visible in the images of the underside of the mesh micro-ECoG device, but are difficult to see in the case of the solid device. Animal was perfused 112 days after implantation.

In order to definitively determine whether the tissue growth between the brain and the electrode array was thicker in the case of the solid device, it was necessary to quantify the amount of tissue growth above and below the devices. To do this, an SD-OCT system was used to obtain cross-sectional views of the electrode arrays and surrounding tissue after the animals had been perfused. Multiple measurements

were taken at different positions within each sample, of the tissue thickness above and below the micro-ECoG devices. In order to determine the actual tissue thickness, it was necessary to divide the thickness measured from the OCT images by the refractive index of the tissue. The tissue refractive index was calculated following the method described in Appendix C. After determination of the actual tissue thickness based on the refractive index, thickness averages were calculated for each animal, as well as across all animals. Figure 3.6 (a)-(e) shows a summary of the OCT thickness measurement results for the mesh and solid devices. Tissue samples from the previous study, in which fenestrated micro-ECoG devices were implanted beneath cranial windows (Schendel et al., 2013), were also analyzed using the OCT system, to determine how the tissue distribution around the fenestrated arrays compared with the mesh and solid devices. The previous micro-ECoG window imaging study also incorporated a subset of "control" animals, which were implanted only with cranial windows, but no devices. These animals also experienced tissue growth beneath the windows, and the thickness of this tissue was analyzed and compared to the total tissue growth thicknesses for the other three types of implants. The average results of these comparisons are shown in Figure 3.6(f).

In addition to quantifying the thickness of the tissue around the micro-ECoG devices, it was also desired to determine the type of tissue that was present. It was initially postulated that this tissue could be composed of collagen, since collagen has been shown to be a major component of scar tissue in most parts of the body (Bailey et al., 1975; Risling et al., 1993; Sun and Weber, 2000; van Zuijlen et al., 2003). Although collagen has not been found to be present in scar tissue growth around indwelling neural implants, this may be because the brain does not have much native collagenous tissue, and so it is not often investigated. The meninges, however, have large collagen components, in particular within the dura mater, which is largely composed of collagen fibers (Jimenz Hamann et al., 1998; Protasoni et al., 2011). Additionally, collagen deposition has been found to occur in the meninges following subarachnoid hematomas (Sajanti et al., 1999). Therefore, the assumption that collagen would be a key player in scar formation, especially in the case of an implant in contact with the dura mater, was not unfounded.

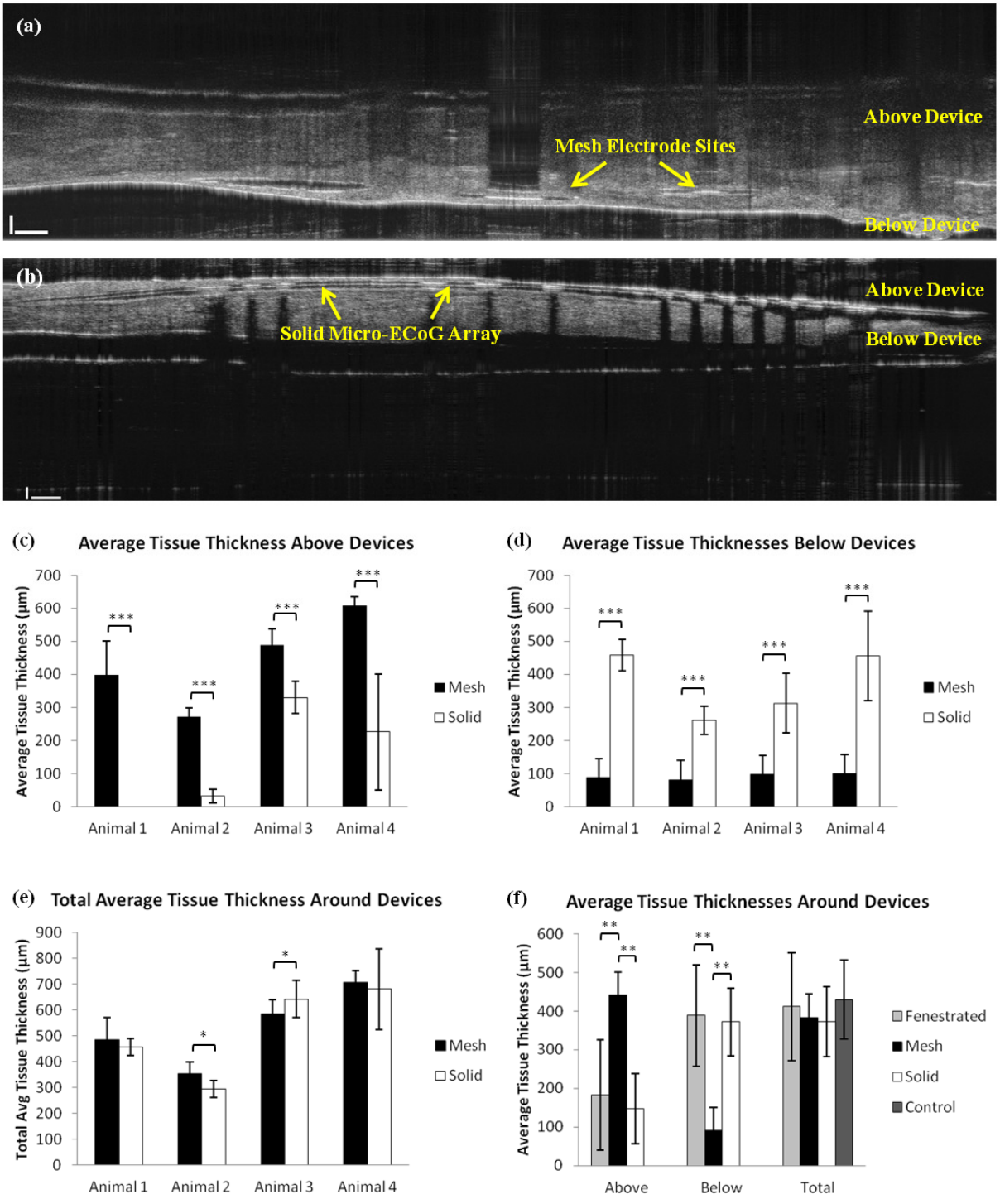

Figure 3.6. OCT tissue thickness data. **(a)** Cross-sectional OCT image of a mesh device and surrounding tissue. **(b)** OCT image of the solid device and surrounding tissue. **(c)** Plot of average tissue thickness above (between the device and the window) mesh and solid devices in four different animals. **(d)** Plot of

average tissue thickness below (between the electrode array and the brain) mesh and solid devices in four different animals. **(e)** Plot of total average tissue thickness surrounding the mesh and solid devices in four different animals. **(f)** Plot of average tissue thickness above and below devices, as well as the total average tissue thickness in the fenestrated, mesh, solid, and control cases. (*P < 0.05, **P < 0.01, *** P < 0.001).

Second harmonic generation (SHG) imaging and traditional histological staining (H&E) were used in conjunction, to establish whether collagen was present in the scar. Figure 3.7(a) and (b) shows SHG images of the tissue surrounding the mesh and solid micro-ECoG devices, respectively. It is apparent from these images that an SHG collagen signal was present in the scar tissue. Collagen fibers appear to align slightly with the curve of the mesh electrode site in Figure 3.7(a), and have wrapped around the edge of the Parylene insulation, spreading both below and above the electrode site and trace. On the left side of the image, a portion of the dura mater, which adhered to the scar tissue upon removal of the brain from the skull, is visible. The collagen fibers of the dura mater appear to be longer and more aligned than those of the scar tissue. The tissue beneath the solid micro-ECoG device, shown in Figure 3.7(b), appears to be thicker and slightly less well-aligned than that around the mesh device.

Figure 3.7(c) and (d) shows images of H&E sections of the scar tissue surrounding a fenestrated micro-ECoG device. The open regions in the center of the tissue shown in Figure 3.7(c) are the areas where the micro-ECoG device had been, as it was dislodged from the microscope slide during the staining procedure. The darker stained tissue near the edges of the image is bone tissue, while the lighter tissue in the center is composed of collagen fibers. The fenestrations through the micro-ECoG device are also visible from this image, and it appears that the collagen has grown completely through these fenestrations and onto the topside of the device. Figure 3.7(d) shows a higher magnification view of the collagen tissue surrounding a small segment of the micro-ECoG device that remained intact during staining.

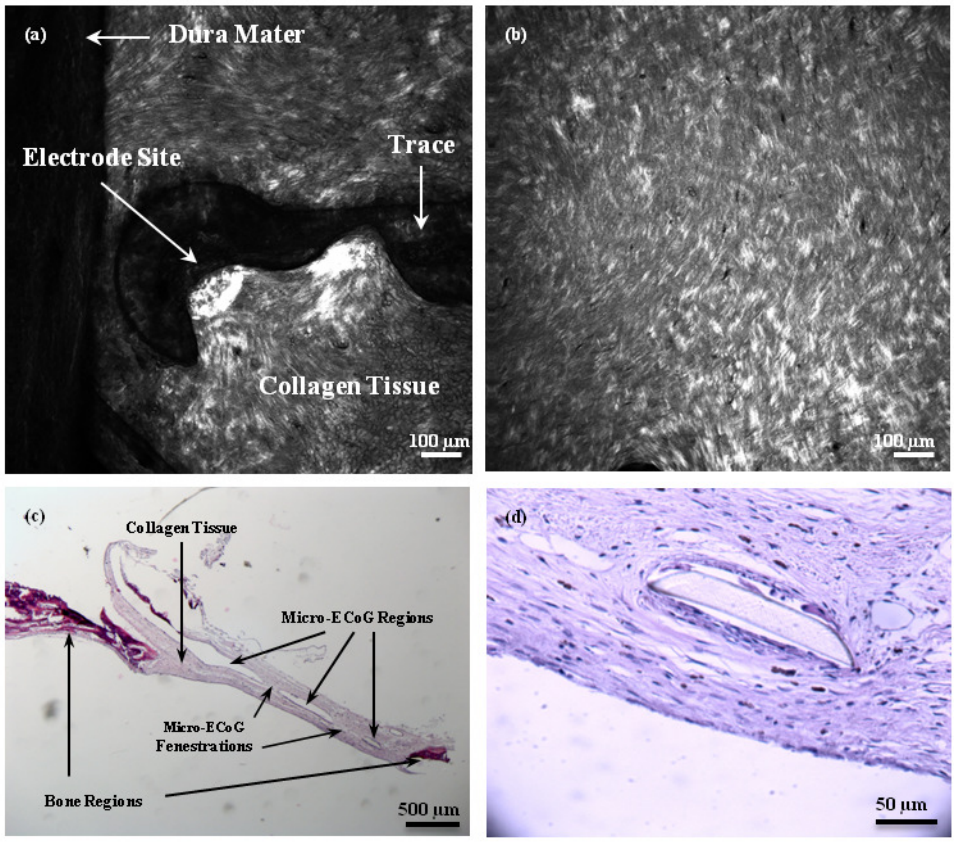

Figure 3.7. SHG and H&E images of scar tissue surrounding Micro-ECoG devices. **(a)** SHG image of scar tissue around one electrode site and trace of a mesh device, looking from the underside of the skull, with the brain removed. **(b)** SHG image of scar tissue beneath a solid micro-ECoG array. **(c)** Bright field image of an H&E-stained cross-section of tissue surrounding a fenestrated micro-ECoG device. Darker stained sections on the edges of the sample are representative of bone tissue, while the lighter regions in the middle are collagen fibers. The open regions in the center represent the place where the micro-ECoG was. The device pieces floated out during the staining procedure. **(d)** Higher magnification image of collagen tissue surrounding a portion of the micro-ECoG device that remained intact during staining.

Longitudinal Impedance Analysis

To determine the effect of tissue growth around the micro-ECoG devices on recorded signal quality, electrode site impedance spectra were measured in conjunction with the cranial window imaging of the tissue response. Figure 3.8(a) shows the average change in the 1 kHz impedance between the first

and final days of implantation for the mesh and solid devices implanted in four different animals. It is apparent from this plot, and the plot of the average impedance for all four animals over time, shown in Figure 3.8(b), that there is not a significant difference between the impedance changes of the two types of devices. The dip in the average impedance change between 30 and 35 days after implantation was attributed to normal day-to-day fluctuations seen in all animals. It is postulated that if all animals had been tested out past this time point the impedance would rise again.

In one case, where the animal was tested for over a year, the average impedance of the mesh device was consistently lower than that of the solid device, after the first twenty days of implantation. A plot of this data is shown in Figure 3.9. Based on the results from this one animal, it is postulated that the reason that no significant impedance difference was observed between the mesh and solid devices over time in most of the animals, was that impedance measurements were only taken for a period of 30 to 40 days, in most cases, and it appears from the plot that most of the significant difference occurs after about 30 days of implantation. Therefore, in the future, it may be necessary to take impedance measurements over a longer period of time in order to see significant results.

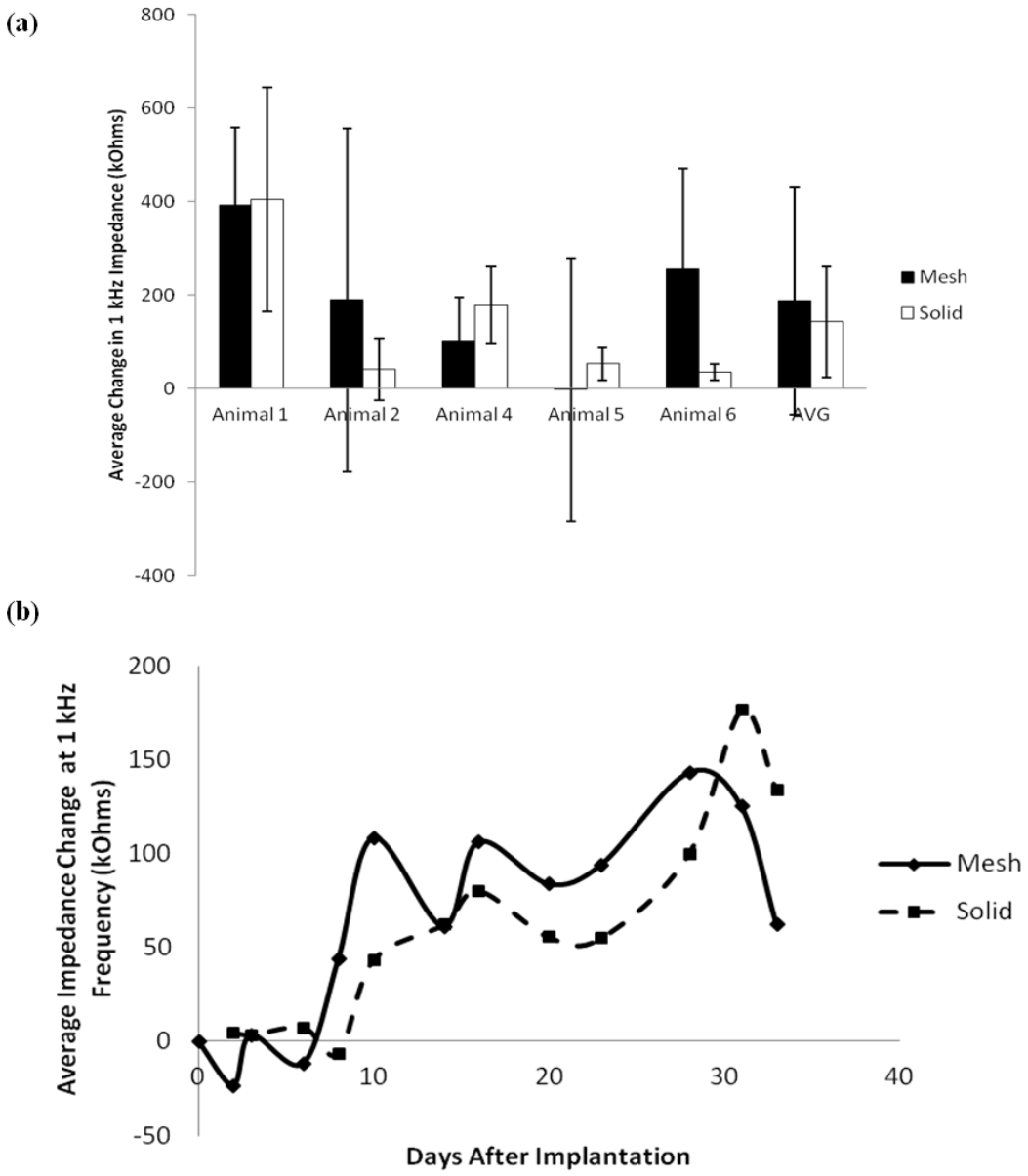

Figure 3.8. Average impedance change data for mesh and solid devices. **(a)** Average change in impedance for mesh and solid devices in four animals on the final day of implantation. Error bars represent +/- one standard deviation. **(b)** Total average change in impedance for mesh and solid devices for four animals. Change in impedance was calculated from the first impedance measurement after implantation and averaged over all 16 channels on each device. If channels had 1 kHz impedance values greater than 1000 kOhms they were considered to be dead channels, and thus not included in the average.

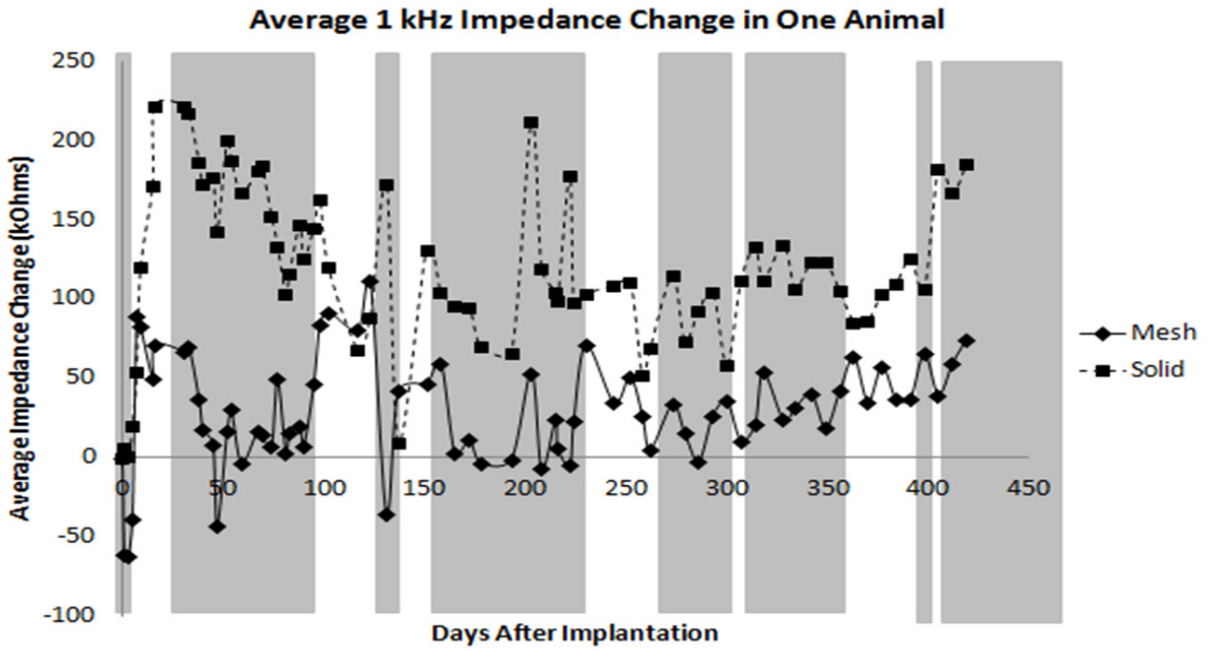

Figure 3.9. Average longitudinal 1 kHz impedance data for mesh and solid micro-ECoG devices implanted in a single animal for over one year. Shaded regions represent time periods where there was a statistically significant difference in the mesh and solid impedance values ($p < 0.05$, student's t test). This data suggests that perhaps major differences in the mesh and solid impedance values may not be noticeable until greater than one month after implantation. Change in impedance was calculated from the first impedance measurement after implantation and averaged over all 16 channels on each device. If channels had 1 kHz impedance values greater than 1000 kOhms they were considered to be dead channels, and thus not included in the average.

Discussion

This study demonstrates that the tissue response to epidurally implanted micro-ECoG arrays differs depending on the substrate geometry. Chronic cranial window imaging of the two types of devices revealed that scar tissue began to grow up between the traces of the mesh devices as early as seven days after implantation. Due to the open architecture of the mesh device, the tissue vasculature was able to

wrap around each individual electrode site and trace, as shown in Figure 3.10. In the case of the solid devices, since the tissue had no immediate pathway to the top surface of the array, it thickened beneath the devices for several days. In some cases it would eventually wrap around the edges of the device and spread over the top surface of the array, as shown in Figure 3.3, but in many cases the tissue growth remained beneath the device for the duration of the implantation period.

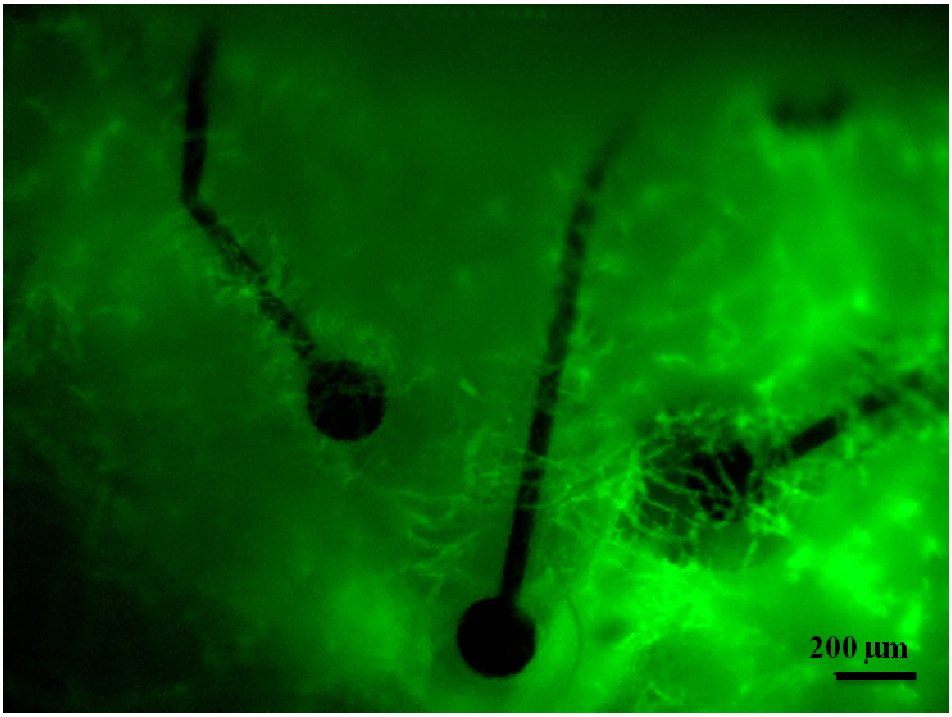

Figure 3.10. Blood vessels wrap around the individually insulated electrode sites and traces of the mesh micro-ECoG device. Image taken 6 days after implantation.

OCT analysis of the tissue surrounding the implants demonstrated that the total thickness of the tissue growth was not significantly different between each of the four conditions (mesh, solid, fenestrated, and control window), but that the distribution of the tissue varied. The tissue thicknesses above and below the devices were significantly different between the mesh devices and the solid and fenestrated devices, however, there was no significant difference between the thickness distributions for the fenestrated and solid devices. These results can be at least partly explained by looking at the percentages of the cortical area covered by each type of device, as shown in Table 3.1. Although the mesh device covers much more

total surface area than the fenestrated or solid devices, the percentage of the implantation area covered is much smaller than that of either the fenestrated or solid devices, since the mesh devices require a larger craniotomy. This suggests that it is not the total amount of area covered by the device that determines the tissue thickness distribution, but the amount of open area through which the tissue can grow to the other side of the device.

Second harmonic generation imaging revealed the presence of collagen in the intact scar tissue, and additional immunohistology confirmed that the bulk of the scar was composed of collagen fibers and was not bone. Further analysis will be necessary in order to determine the type of collagen present, as well as whether the fiber length or alignment differs between the different types of devices.

Astrocyte and microglia antibody staining was also performed on the brain of the animal which was implanted for one year, to determine whether there was a glial response to the presence of the array. Figure 3.11 shows cortical sections of brain beneath the mesh and solid devices, stained with GFAP (for astrocytes) and Iba1 (for microglia) antibodies. From the images, it is apparent that there was an astrocytic response to the devices, but not a significant response from the microglia. Future studies involving chronic *in vivo* imaging on a cellular level using techniques such as multi-photon intravital imaging (Potter et al., 1996; Tozer et al., 2005; Tremblay and Majewska, 2011) would be beneficial to gain a complete understanding of the tissue response to these implanted arrays, as well as to lend a better understanding to the electrode site impedance data.

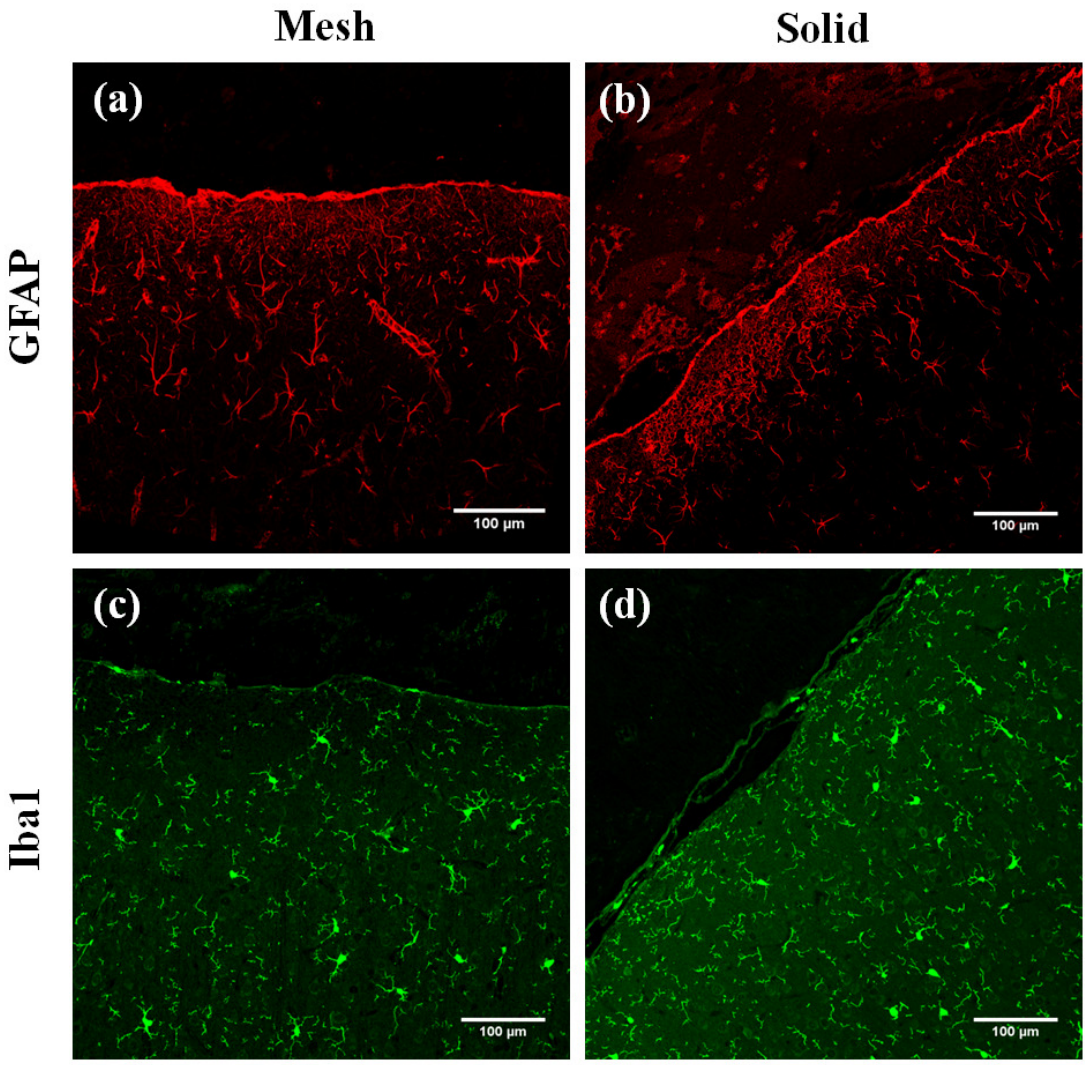

Figure 3.11. Astrocyte and Microglia staining of cortical brain tissue sections below mesh and solid devices. **(a)** GFAP antibody staining of astrocytes in brain tissue below mesh device. **(b)** GFAP staining of astrocytes in brain tissue below solid micro-ECoG device. **(c)** and **(d)** Iba1 antibody staining of microglia in brain tissue below mesh and solid devices, respectively.

Although most of the impedance data revealed no significant differences between 1 kHz impedances for the mesh and solid devices, differences were observed in the animal implanted for an extended period of time. This suggests that perhaps impedance stabilization occurs over a time course longer than one month after implantation. This could be due to consolidation of the collagen layers over

time (Daniels et al., 2003), or due to changes on a more cellular level (i.e. the astrocytic response mentioned above), which were not observable via the cranial window imaging method. In the animal with the dural tear, a tissue ranking system was developed, to correlate the amount of scar tissue around a particular electrode site with the electrode site's 1 kHz impedance. The correlation is shown in Figure 3.12, and indicates that electrode sites with larger amounts of surrounding scar tissue have more variable, and perhaps higher, impedance values. Additional studies involving purposely creating dural tears during electrode implantation or subdurally implanting micro-ECoG arrays, would not only aid in understanding the nature of the collagen scar tissue formation and whether it is purely a dural response, but would also allow for more thorough tissue-impedance correlation studies, since the presence of the dural tear seemed to create more variability in the tissue response.

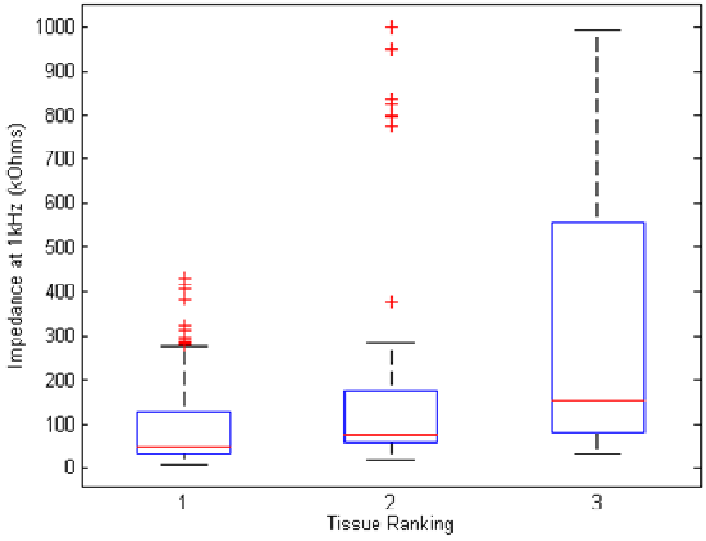

Figure 3.12. The correlation between the amount of tissue around an electrode site and its 1 kHz impedance. One animal, which was implanted for one year and had variable tissue growth around different electrode sites was analyzed. One representative image was selected from each imaging session over the entire implantation period. Images were randomized and given to an individual who would rank each electrode site with a value of 1, 2 or 3. Tissue rankings were defined by the following criteria: 1: No

visible scar tissue around the electrode site. 2: Some scar tissue visible around the electrode site, but site is still clearly visible through the cranial window. 3: Electrode site completely obscured by scar tissue.

Overall, the results of this imaging study corroborate the previous studies, which have found that devices with open architecture are more ideal neural platforms (Kim et al., 2007; Seymour and Kipke, 2007). However, it must be noted that in the current study, the mesh device did not elicit a smaller tissue response, but instead a more ideal distribution of the scar tissue for our application. The presence of significantly thicker tissue between the recording sites and the brain could have a detrimental impact on the ability of the device to record neural signals, since the tissue would create a greater distance between the electrode sites and the neurons they are recording from, as well as an insulating barrier that would hinder the transmission of the neural signals. Although, these experiments did not demonstrate a stark impact of tissue thickness on recorded signal quality, it must be noted that this study was performed in rats, which have very small tissue thicknesses compared to humans. In a human model, the tissue distribution would likely have a much larger impact on the quality of the recorded signals, due to an increased tissue thickness for the neural signals to travel through (Bundy et al., 2014). Development of substrate geometries which result in tissue thickening on top of the device and remaining thin below it, such as in the case of the mesh micro-ECoG array, allow for the device-anchoring benefits of having tissue integrated within the array, while minimizing the unfavorable signal quality degradation.

The results of this study inform future work, which will first be directed at determining the role of the dura mater in this scar tissue formation, through dural resection prior to device implantation. In addition, the longitudinal response of other cell types, such as astrocytes and microglia, to neural interfaces implanted on the surface of the brain will be investigated through the use of multi-photon intravital imaging techniques. Additional studies could incorporate the delivery of drugs and other factors to the implant site, to evaluate their impact on scar tissue formation and recorded signal quality. Some substances which may be of interest to explore include collagenase, to suppress collagen formation, VEGF, to stimulate angiogenesis, and Thalidomide, to inhibit angiogenesis. The delivery of these

substances to the implant site may lead to a better understanding of the role of specific tissue types (i.e. collagen and vascular tissue) in scar formation.

Conclusion

In vivo imaging of the mesh and solid micro-ECoG devices via the cranial window implantation scheme revealed the growth of a collagen scar tissue around both electrode arrays over a period of one month after implantation. With the aid of optical coherence tomography, it was found that the distribution of this collagen scar tissue was significantly different between the two types of devices, with the results suggesting that a more open architecture device would be beneficial for minimizing the amount of scar tissue formation between the electrode sites and the brain. Future, longer-term studies will be necessary in order to definitively demonstrate the impact of device geometry on recorded signal quality, as well as the role of the dura mater. Development of cellular level *in vivo* imaging techniques will provide a more thorough understanding of all of the mechanisms involved in the tissue response to implanted electrode arrays.

4 CARBON LAYERED ELECTRODE ARRAY (CLEAR) TECHNOLOGY

Abstract. Optically transparent neural micro-electrode arrays are advantageous for electrophysiological studies involving optogenetics and cortical imaging. Here, we present a graphene-based, transparent micro-electrocorticography device and demonstrate its performance *in vivo*. CLEAR devices were fabricated with transparent electrode sites composed of 4 graphene monolayers and implanted epidurally in rats and mice. Device viability was evaluated via recording of spontaneous local field potentials, electrode site impedance spectra, and sensory evoked potentials. Additionally, optogenetic experiments and *in vivo* imaging of the cortical vasculature via fluorescence microscopy and optical coherence tomography were performed. The results of this study suggest that the CLEAR device has utility for many neural interfacing applications.

Introduction

With the advent of optogenetics and increasingly more *in vivo* imaging methodologies, there has been a large push to develop transparent electrode arrays for neural applications (Gross et al., 1985; Kwon et al., 2012; Peter Ledochowitsch et al., 2011). Previously, micro-electrocorticography (micro-ECoG) devices have proven useful for long-term neural recordings from the brain surface (Henle et al., 2011; P. Ledochowitsch et al., 2011; Rubehn et al., 2009; Thongpang et al., 2011; Viventi et al., 2011). These devices sit on top of the cerebral cortex rather than penetrating into it, reducing the amount of scar tissue formation and extending the recorded signal longevity. The flexibility of the micro-ECoG's polymeric substrate not only allows these devices to conform to the cortical surface, but also to move with the brain as it shifts within the skull, minimizing the amount of trauma caused by mechanical impedance mismatch. Moreover, the transparency of the polymer enables light delivery through the substrate to the underlying neural tissue, for optogenetic and intravital imaging experiments (Richner et al., n.d.; Schendel et al., 2013). Up until recently, however, micro-ECoG conductors have been composed of reflective metallic

materials, such as gold and platinum. Thus, although light is easily transmitted through the device substrates, optical stimulation or imaging through the electrode sites has not been possible.

In recent years, new micro-ECoG devices have been fabricated with transparent electrode sites (Kwon et al., 2012; Peter Ledochowitsch et al., 2011). To date, the most commonly used transparent electrode material has been indium-tin oxide (ITO) (Gross et al., 1985; Jo et al., 2012; Kwon et al., 2012; Peter Ledochowitsch et al., 2011). However, due to the limited availability of indium, the price of ITO is always increasing. In addition, obtaining a highly transparent, low resistivity ITO film most often requires sputtering and annealing processes occurring around 200-300^{o} C (Bender et al., 1999; Minami, 2008). Parylene C is a transparent polymer commonly used as a substrate material for neural surface electrodes due to its flexibility, biocompatibility, and dielectric properties. Its glass transition temperature is approximately 90^{o} C, while its melting temperature is around 290^{o} C (Noh et al., 2004). Therefore, although processing of ITO on Parylene C and other polymer substrates has been accomplished, it requires complex process modifications which can compromise the quality of the ITO films (Park et al., 2001; Pokaipisit et al., 2008). Furthermore, ITO is brittle under bending conditions, and so is not an ideal material for flexible electronic applications (Paetzold et al., 2003). In this study, we propose the use of graphene as a substitute for ITO in neural microelectrode arrays (MEAs).

Because of its excellent conductivity, transferability and strength, as well as its tunable electronic properties, graphene has been widely researched for a variety of applications, including transistors, solar cells, and electrodes for lithium ion batteries (Liao et al., 2010; Wang et al., 2010, 2008; Wu et al., 2008; Xia et al., 2009; Yang et al., 2010; Yoo et al., 2008). Additionally, there have been efforts to employ graphene for biological-based applications, such as DNA sequencing and bio-sensing (Alwarappan et al., 2009; He et al., 2010; Min et al., 2011; Postma, 2010; Schneider et al., 2010). Although the general biocompatibility of graphene is difficult to assess due to its inherent variability (Pinto et al., 2013; Zhang et al., 2010), there have been several studies which have reported chemical vapor deposited (CVD) graphene sheets to be biocompatible as well as to enhance cell adhesion, proliferation, and differentiation (Chen et al., 2008; Kalbacova et al., 2010; Li et al., 2011; Park et al., 2011). In addition, the transparency,

flexibility, and mass-producibility of CVD graphene sheets make them an ideal candidate for replacement of ITO in neural MEAs (Bae et al., 2010; Jo et al., 2012; Kim et al., 2009). Here, we report a fabrication method for a graphene-based carbon layered electrode array (CLEAR) technology for neural applications, and demonstrate its viability for electrophysiology, optogenetics, and *in vivo* imaging experiments.

CLEAR Device Fabrication

Following graphene characterizations using Raman Spectroscopy (as described in Appendix D), implantable graphene neural electrode arrays were fabricated on a 4-inch silicon wafer. Figure 4.1(a) shows a simplified schematic of the fabrication process. Briefly, wafers were coated with Parylene C films using a chemical vapor deposition process. Next, the connection pads and initial portions of the traces were patterned with gold via electron beam metal evaporation and lift-off techniques. The use of gold for the traces and pads was to ensure a good mechanical connection to the zero insertion force (ZIF) printed circuit board (PCB) connectors used for reading the brain signals into the computer (Imagineering Inc, Elk Grove Village, Illinois). The electrode sites and portions of the traces that were to be in contact with the brain were left for the consequent graphene transfer and patterning, such that the brain contact area of the electrode would be transparent. Following metallization, four graphene monolayers were transferred and stacked sequentially onto the wafer surface, using the wet transfer technique described in Supplemental Figure 1. A sacrificial layer of SiO_2 was then deposited to protect the graphene layers from being etched in subsequent reactive ion etching (RIE) steps. After that, the graphene was patterned to form the electrode sites using RIE, and another insulating layer of Parylene C was deposited. RIE was then employed to expose the electrode sites and pads, and form the array outlines. Finally, the devices were peeled from the wafer, the SiO_2 protection layer was removed by wet etching, and the devices were inserted into the PCB connectors.

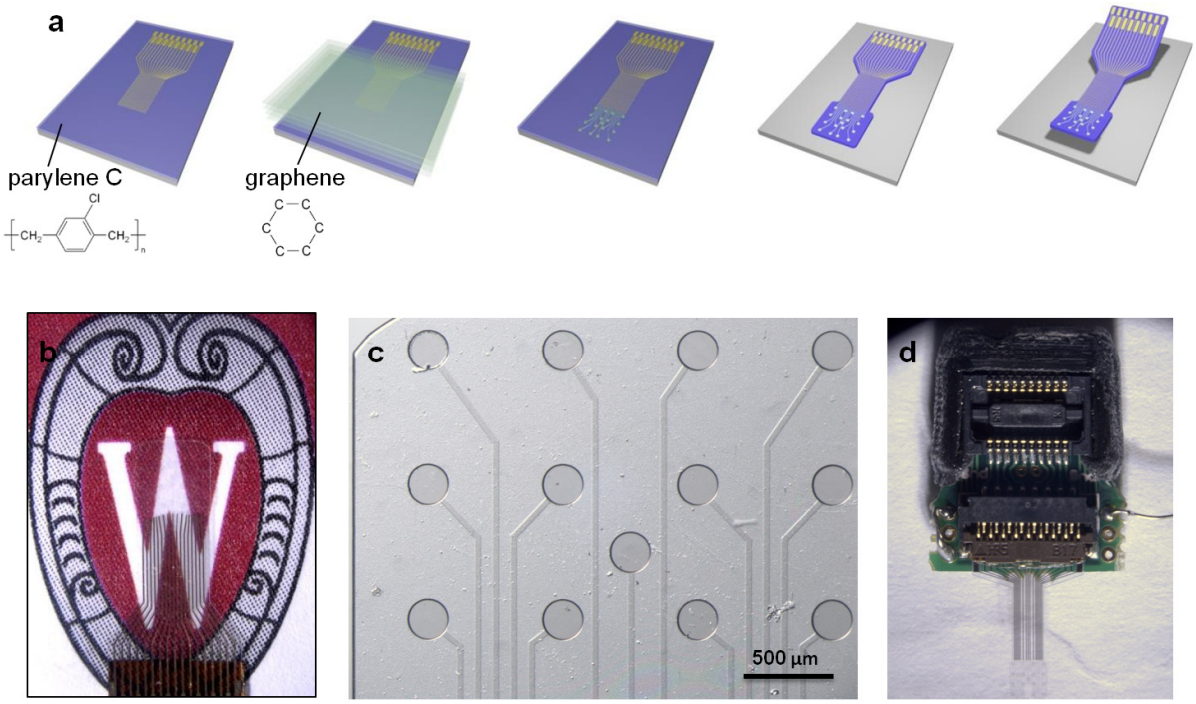

Figure 4.1. CLEAR Device. **(a)** Basic fabrication process. **(b)** Rat-sized CLEAR device. **(c)** Close-up of rat-sized device showing transparent graphene electrode sites and traces on a Parylene C substrate. **(d)** Mouse-sized CLEAR device with ZIF PCB connector.

Device Validation:

Electrical Impedance Spectroscopy

The patency of the completed devices was verified via electrical impedance spectroscopy. Impedance spectra were obtained for each electrode site using an Autolab PGSTAT12 potentiostat (Eco Chemie, Utrecht, Netherlands). Devices were connected to the Autolab machine via the PCB connectors, which were connected to a passive 32-channel Tucker-Davis Technologies (TDT) head stage. Impedances were evaluated at 30 different frequencies, ranging from 10 Hz to 30,937 Hz. If electrode sites had impedance values less than 600 kOhms at 1 kHz frequency, they were considered to be viable for implantation. 1 kHz frequency was selected for evaluation because it is known to be a common benchmark for neural impedance analysis (Norlin et al., 2002; Williams et al., 2007). Figure 4.2(a) shows

representative electrical impedance spectra for CLEAR and traditional platinum micro-ECoG devices tested in saline. It is apparent from the plot that the phase angle is higher in the case of the CLEAR device. This means that the value of the reactance is higher for the graphene sites than for the platinum. However, the average magnitude of the impedance at 1 kHz frequency was only slightly higher for the CLEAR device than for the platinum array (243.5 ± 5.9 kΩ for graphene vs. 188.8 ± 92.9 kΩ for platinum), and since the signal recording apparatus involves the use of a high impedance buffer headstage amplifier, the reactance difference should not affect the signal recordings.

Cyclic Voltammetry

In addition to impedance spectroscopy, cyclic voltammetry was performed on select CLEAR devices, as well as on devices with gold electrode sites, for comparison purposes. Cyclic voltammetry (CV) was also performed using the Autolab system. CV scans were taken from -0.6 V to 0.8 V with a step potential of 0.0105 V and a scan rate of 0.0500 V/s (Otto et al., 2006; Wilks et al., 2012). The voltage range was chosen so as to stay within the water window. Average CV curves for gold, platinum, and CLEAR devices are shown in Figure 4.2(b) and (c). The CV results for the platinum device were drastically different than those for either the gold or the CLEAR devices. Although this demonstrates that the platinum electrode sites have a greater charge carrying capacity, it does not rule out the use of CLEAR devices for neural interfacing applications. In fact, there was no significant difference between the average CV curves for the CLEAR and gold electrode sites. As gold has proven itself as a reliable material for recording electrode sites (Gross, 1979; Yuen and Agnew, 1995), this suggests that the graphene conductors will also be sufficient.

Photoelectric Testing

It was also desired to test the photoelectric effect of the graphene electrode sites, to verify that the CLEAR devices would be useful for optogenetic experiments. Optogenetics is a scientific method involving genetic modification of cells to incorporate light-sensitive proteins, such as channelrhodopsin

and halorhodopsin, into cell membranes (Deisseroth, 2011). These proteins act as light-activated ion channels, allowing the flow of specific ions into and out of the cell when subject to particular light wavelengths. Depending on the type of ion channel, the ion diffusion will either cause a depolarization or a hyperpolarization of the cell, which, in the case of neurons, causes excitation or inhibition of neural activity, respectively. This relatively new technique is revolutionizing the way researchers study neural networks, and the development of transgenic animals with optogenetic qualities has led to many enlightening behavioral neuroscience studies (Bernstein and Boyden, 2011; Cazorla et al., 2014; Tsai et al., 2009).

The invention of completely transparent neural surface electrode arrays enhances the researcher's ability to combine optogenetics with electrophysiology, by allowing for delivery of light stimuli through the array, directly to the region of the brain from which the recordings are obtained. However, if the magnitude of the artifact produced by shining light through the graphene electrode sites is too large, it would be difficult to distinguish optically evoked neural signals from stimulus artifacts, and thus the device would not be useful for optogenetic applications. To test photoelectric or other photochemical effects, the devices were placed face-down in saline solution and an optical fiber connected to a 100 mW, 473 nm diode LASER (Laserglow Technologies, Ontario, Canada), was used to shine light onto the backs of the electrode sites. The light pulses were delivered by applying 3 V to the LASER for 3 ms (up to 80 mW/mm^2). Figure 4.2(d) shows the electrical pulses elicited by the light impingent on graphene and Platinum sites. From the plot, it appears that the magnitude of the photoelectric effect is similar for both the graphene and the platinum sites, although the platinum electrode returns to baseline more quickly. In both cases, the stimulus artifact is less than 50 μV. Since cortical evoked potentials are generally in the range of 100 μV, this should not create a problem in an *in vivo* setting.

Transmittance Measurements

Another important characteristic for optogenetic application of the CLEAR device is the amount of light transmitted through the graphene electrode sites and Parylene substrate. Since the intention for the transparent device is that we can both image and project light onto the underlying brain tissue, it is important that a large percentage of the light impingent on the array is transmitted through the device. A plot of the percentage of light transmitted through a sample of 4 graphene monolayers on a Parylene C substrate versus wavelength is shown in Figure 4.2(e). The measurements were taken for light wavelengths from 300 to 1500 nm using a UV/Vis Spectrometer (Perkin Elmer). The sinusoidal shape of the transmittance curve is common for the Parylene C material (Yoo et al., 2012). An average of about 90% of the light impingent on the substrate is transmitted at the desired wavelengths (470 nm for excitation of channelrhodopsin and 570 nm for halorhodopsin). This is similar to what has been previously reported, and is sufficient for many optogenetic and imaging applications (Kim et al., 2009; Kwon et al., 2012).

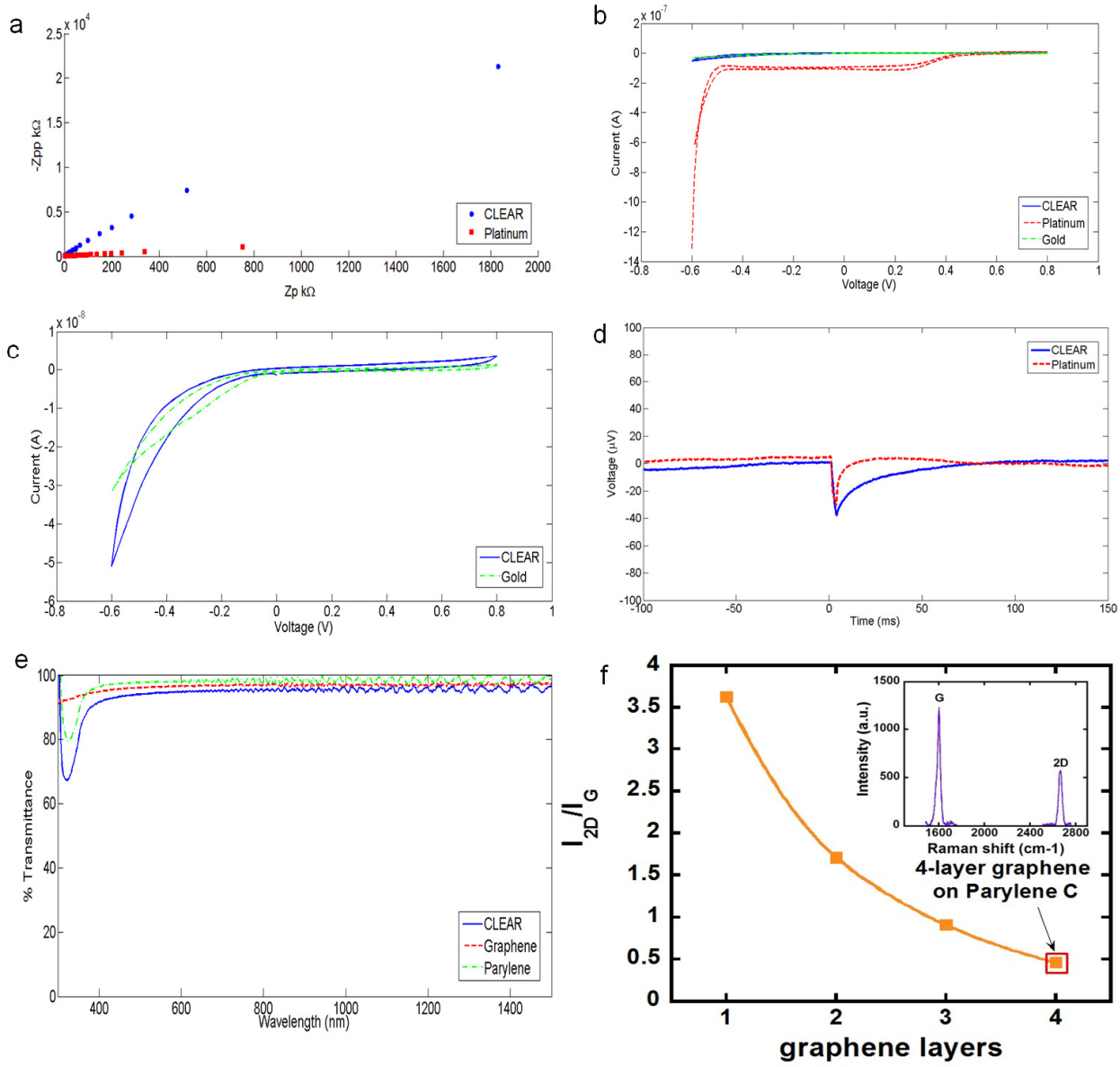

Figure 4.2. Electrode Characterizations. **(a)** Electrical impedance spectra for CLEAR and Platinum micro-ECoG devices in saline. X-axis represents real impedance, y-axis represents imaginary impedance. Each point was taken at a different frequency, between 10 Hz and 31 kHz. **(b)** Average cyclic voltammetry results over 16 electrode sites on CLEAR, gold, and platinum micro-ECoG arrays. **(c)** Average cyclic voltammetry results for 16 electrode sites on CLEAR and gold micro-ECoG arrays. **(d)** Average photoelectric effect test results for CLEAR and Platinum micro-ECoG devices, with light applied to a single electrode site on each device via a optical fiber attached to a blue LASER with an

application of 3V power for 3 ms. **(e)** Transmittance test results for four graphene monolayers on a 15 µm Parylene C film (CLEAR), for four graphene monolayers only (Graphene), and for Parylene C film only (Parylene). **(f)** Raman spectroscopy results for 1, 2, 3, and 4 stacked graphene monolayers.

In Vivo Evaluation

Electrophysiology

To demonstrate *in vivo* performance of the CLEAR devices, the arrays were implanted in two rats and two mice, one wild-type for imaging and one Thy1::ChR2 for optogenetic testing. Supplemental Table 4.1 describes the type of implantation performed in each case, as well as the type of data collected from each animal. All animal procedures were approved by the Institutional Animal Care and Use Committee (IACUC) at the University of Wisconsin-Madison. Surgical procedures and *in vivo* imaging sessions were performed under anesthesia, and all efforts were made to minimize animal discomfort.

Table 4.1. Summary of implantation schemes and experimental paradigms for each animal. R1 and R2 represent the rats and M1 and M2 represent the mice.

Animal	Implant Description	In Vivo Vascular Imaging	Impedance Spectroscopy	Baseline Signal Recordings	Electrical Evoked Potentials	Optogenetic Experiments	OCT
R1	Bilateral Rat Pt micro-ECoG and CLEAR device with gold traces	X	X	X	X		
R2	Rat CLEAR device		X	X	X		
M1	Completely Transparent Mouse CLEAR device (terminal)			X		X	
M2	Completely Transparent Mouse CLEAR device (terminal)	X					X

Following implantation of the devices, electrode site impedance spectra and baseline signal recordings were tested daily for the duration of the implantation period, in the case of the rats. Electrode site impedance spectra were generated using the Autolab PGSTAT12 described above. Baseline signal recordings were obtained using a TDT neurophysiology work system. Signals were recorded via a 32-channel active TDT headstage, plugged into the PCB connector. The headstage was connected to a TDT

PZ2 amplifier, which amplified the signal before sending it to the TDT RZ2 system, from which it was sent to the computer. Five minutes of baseline signal data was recorded during each session. Animals were awake and behaving for both the baseline signal recordings and the impedance spectra collection.

Average electrode site impedance changes (measured from the first day of device implantation) for CLEAR and platinum micro-ECoG arrays implanted in the same animal are plotted over time in Figure 4.3(a). Both devices experienced a steep rise in impedance within the first 10 days after implantation, most likely due to the initial tissue response to the implanted arrays (Williams et al., 2007). After this initial sharp increase, the impedances appear to have plateaued, with some minor day-to-day fluctuations. The shape of these impedance curves is characteristic of epidurally implanted micro-ECoG devices (Schendel et al., 2013). There was no statistically significant difference between the impedance changes for the CLEAR and platinum micro-ECoG devices over the entire implantation period, suggesting that the CLEAR device will perform as well as the platinum device over the explored time period.

Figure 4.3(b) shows power spectra for the baseline local field potentials recorded by single channels on the CLEAR and platinum micro-ECoG devices. As with the longitudinal impedance data, there is no significant difference between the signals recorded by the two different arrays.

In addition to baseline signal recordings and impedance spectroscopy measurements, both rats were tested for electrical evoked potentials. In these experiments, the hind legs of the animals were stimulated with electromyogram (EMG) surface electrodes placed over the sciatic nerve. Stimuli consisted of 1 ms biphasic electrical pulses, with amplitudes varying from 1-3 mA. Evoked potentials were recorded with stimuli applied both ipsilateral and contralateral to the implanted devices, in order to verify that the result was, in fact, the somatosensory response to the electrical stimulus. If this was true, evoked potentials would be seen only when the stimuli were applied contralateral to the implanted electrode array, due to the crossing of the neural pathways in the brain stem and spinal cord. Figure 4.3(c) shows a summary of the evoked potential results for the CLEAR device at two stimulation levels. In general, the results displayed in Figure 4.3 show that the graphene electrode sites are capable of recording

both spontaneous baseline activity and evoked neural signals with the same level of clarity as the platinum sites, and generally similar impedance behavior and stability over time.

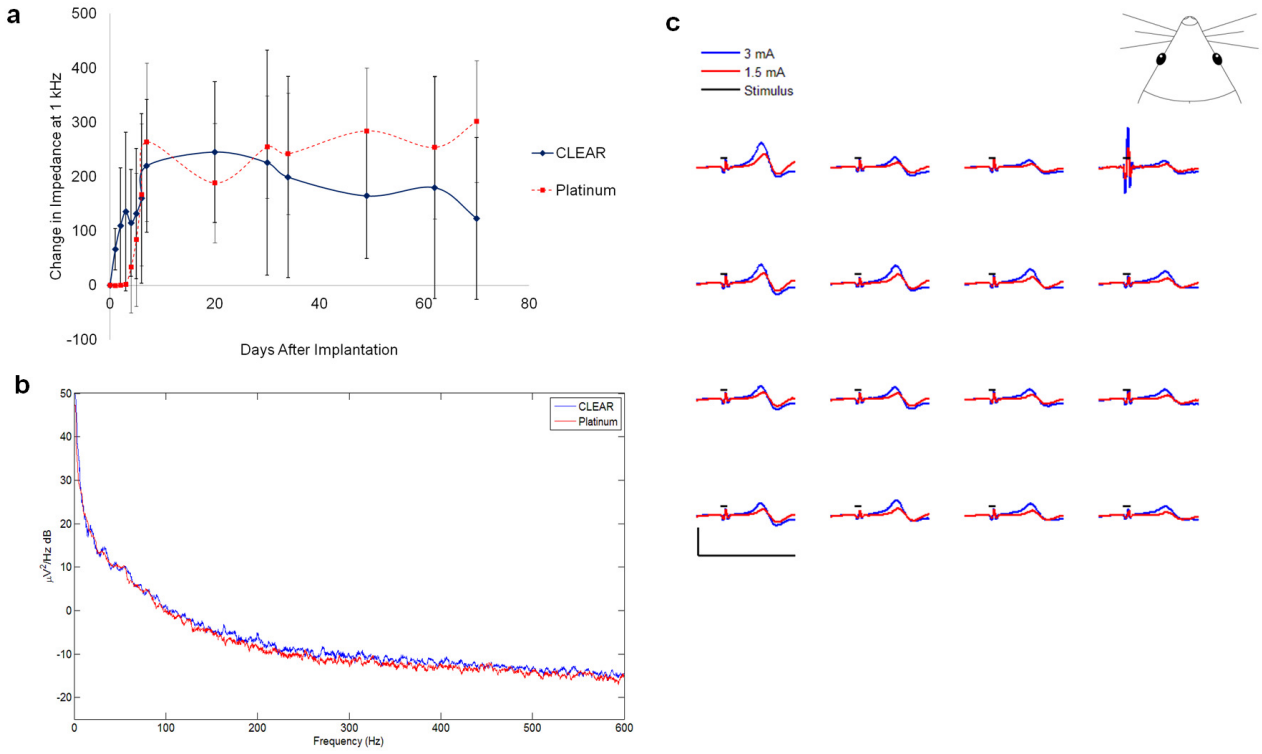

Figure 4.3. *In vivo* recorded signal characterization. **(a)** Average longitudinal 1 kHz impedance values for CLEAR and platinum micro-ECoG devices implanted in the same animal. **(b)** Baseline signal power spectra for the CLEAR and platinum devices. **(c)** Sensory evoked potentials recorded by the CLEAR device, via electrical stimulation of the sciatic nerve on the hind leg of the rat, contralateral to the array. Stimuli were applied for 1 ms at 3 mA and 1.5 mA current levels. X-scale bar represents 50 ms, y-scale bar represents 100 µV.

Optogenetics

One Thy1::ChR2 mouse was implanted with a CLEAR device for the purposes of optogenetic evaluation. This mouse had neurons expressing the Channelrhodopsin-2 protein, making them susceptible to excitation when in contact with blue (473 nm) light. The electrode was implanted on the cortex via the

previously described procedure, but in this case, no window was placed over the array. Instead, the brain was left open, and an optical fiber, attached to the LASER was brought into close proximity with the cortex (Figure 4.4(a)). The anesthesia was switched from isoflurane, which inhibits neural signaling, to a combination of ketamine (75 mg/kg) and dexmedetomidine (25 µg/kg). Concentrated blue light, with a maximum power of 80 mW/mm^2, was then directed onto various regions of the brain, through the CLEAR device (Figure 4.4(b)), while simultaneously recording the neural response to the optical stimulation. The average evoked response is shown for three different stimulation levels in Figure 4.4(c). The initial peak is the stimulus artifact resulting from the photoelectric effect, and the second, longer peak is the evoked neural response. The evoked response is clearly distinguishable from the stimulus artifact, suggesting that the CLEAR device is an acceptable technology for optogenetic experiments.

Once experimentation was complete, the animal was euthanized with an intraperitoneal injection of Fatal PLUS pentobarbitol solution, and a control experiment was conducted with the electrode on the brain of the euthanized animal, to verify that the signals recorded were from neurons affected by the light stimulation, and not due to the photoelectric artifact. From Figure 4.4(d) we can see that the signal magnitude is significantly lower for the recordings obtained from the post-mortem control experiment than for the signals recorded from the living animal. Furthermore, for the control, there was only an evoked signal on the channels which experienced direct light stimulation, whereas Figure 4.4(c) shows a large spatial distribution of the signals from the live animal. These results demonstrate that the signals in Figure 4.4(c) were evoked neural responses to the light stimulation, while those in Figure 4.4(d) were a result of the photoelectric artifact.

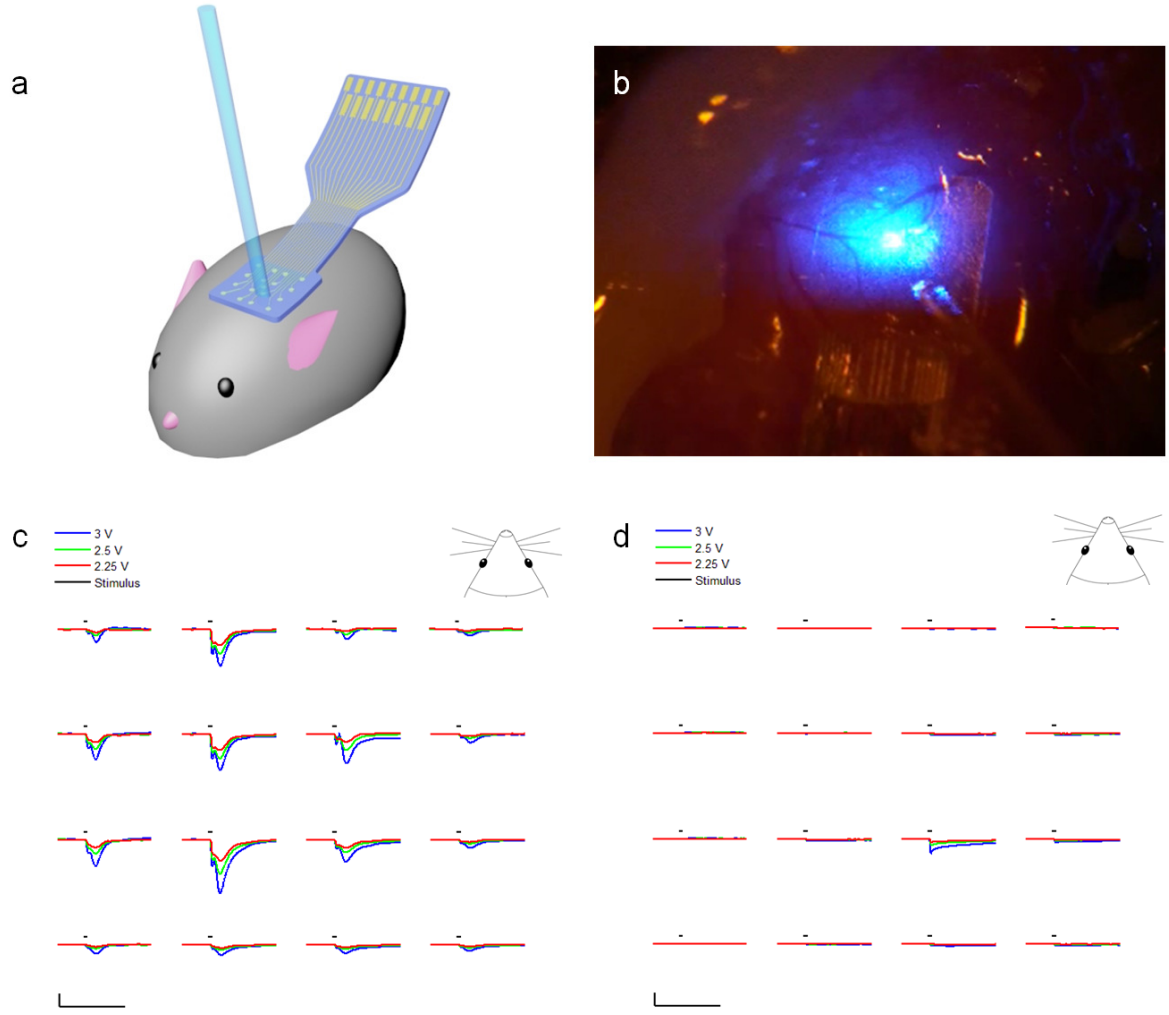

Figure 4.4. Optogenetic Experiment. **(a)** Schematic drawing of opto-experimental setup, showing the clear device implanted on the cerebral cortex of a mouse, with an optical fiber delivering blue light stimuli to the neural cells. **(b)** Image of a blue light stimulus being delivered via an optical fiber, through the CLEAR device implanted on the cortex of a Thy1::ChR2 mouse. **(c)** Optical evoked potentials recorded by the CLEAR device. **(d)** Post-mortem control data, with light impingent on electrode site 11, as is apparent by the stimulus artifact visible in the signal for that channel. X-scale bars represent 50 ms, y-scale bars represent 100 μV.

Cranial Window Imaging

A subset of the implanted animals was imaged via the cranial window imaging method previously described by Schendel et. al (Schendel et al., 2013). Representative images of the cortical vasculature through the CLEAR micro-ECoG device are shown in Figure 4.5 (a)-(d). Images in the left column were taken in bright-field, while those on the right were taken under blue (470 nm) light with the aid of a tail vein injection of FITC-Dextran to fluorescently label the vasculature. These images demonstrate the clarity of the graphene electrode sites and the ability to view the underlying cortex and cerebral vasculature through the CLEAR device. Blood flow video recordings taken through the transparent graphene electrode sites can be seen in supplemental figure S8. Figure 4.5 (e) and (f) shows cranial window images of a standard platinum micro-ECoG array, with the electrode sites and traces clearly visible.

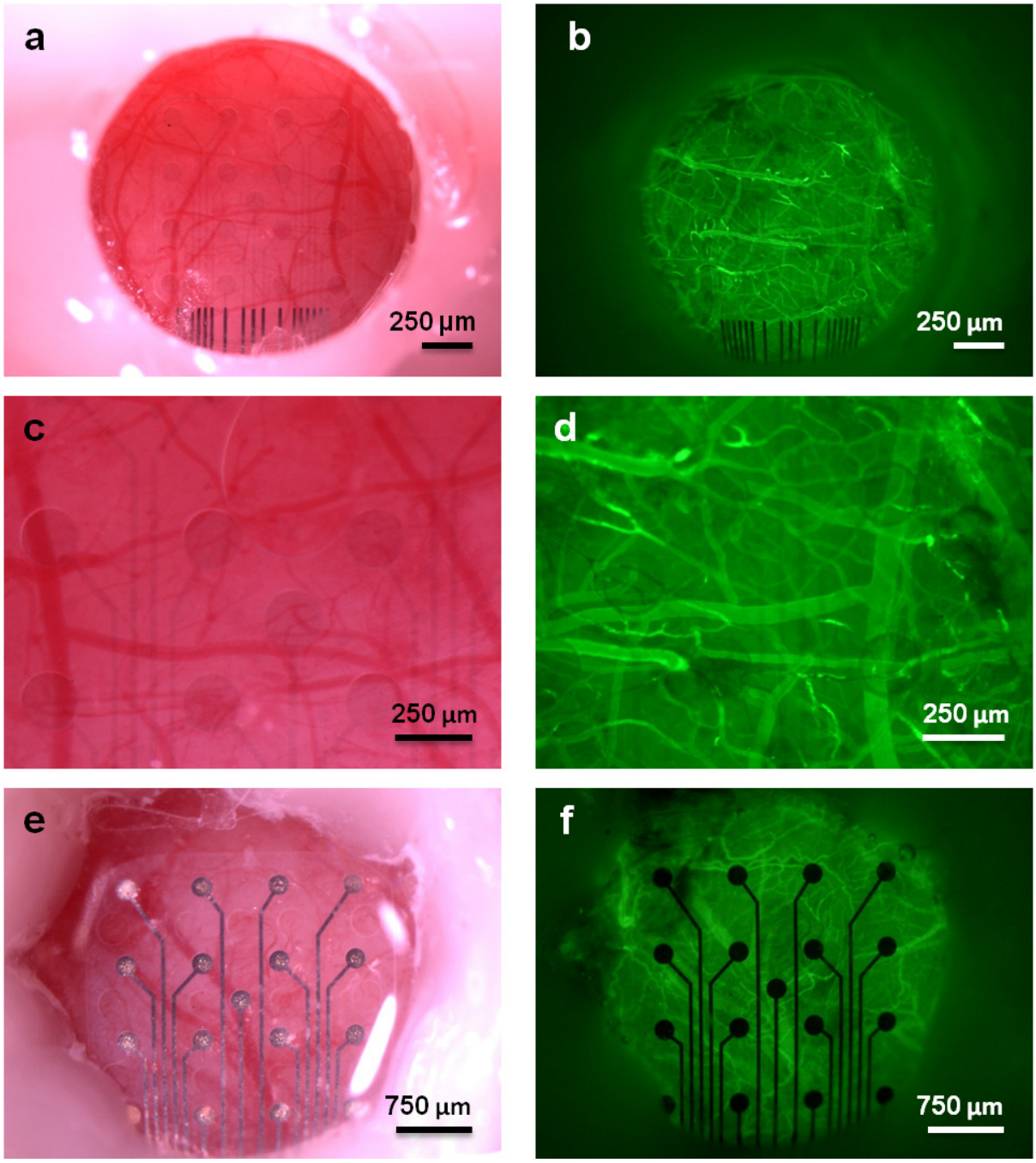

Figure 4.5. In vivo Imaging Results. **(a)** Bright-field image of a CLEAR device implanted on the cerebral cortex of a mouse beneath a cranial window. **(b)** Fluorescence image of same device shown in (a). Mouse was given an intravenous injection of FITC-Dextran to fluorescently label the vasculature. **(c)** and **(d)** Higher magnification bright-field and fluorescence images of same device shown in (a) and (b),

respectively **(e)** and **(f)** Bright-field and fluorescence images of standard rat-sized micro-ECoG array with platinum electrode sites, respectively.

Optical Coherence Tomography

In addition to fluorescence imaging of the cortical vasculature, angiograms and doppler blood flow images were obtained via optical coherence tomography (Figure 4.6). In the angiogram shown in Figure 4.6(a), interference from the gold traces is visible on the right side of the image, but neither the Parylene C substrate nor the graphene electrode sites and traces produced any artifacts.

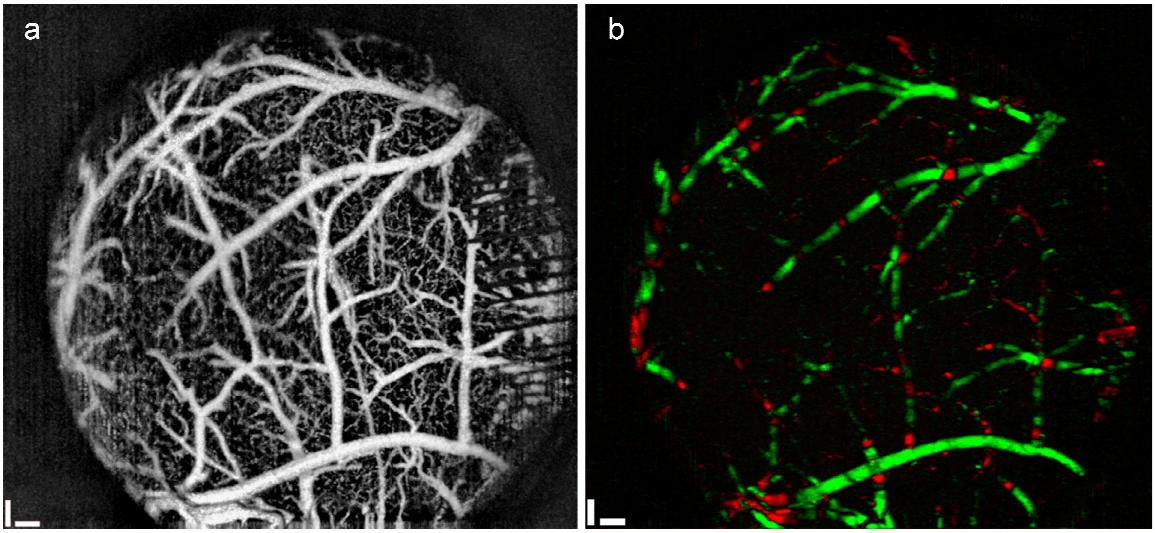

Figure 4.6. Optical coherence tomography through CLEAR device. **(a)** OCT angiogram showing cortical vasculature visible through CLEAR micro-ECoG device. **(b)** Doppler blood flow velocity image showing the directionality of blood flowing through the vasculature below the device. Green represents blood flowing towards the camera, and red represents blood flowing away.

Conclusion

The results of this study demonstrate that the CLEAR micro-ECoG device is capable of recording neural signals with the same degree of clarity as the platinum array, in addition to allowing for optogenetic stimulation as well as both fluorescent and OCT imaging through the transparent electrode sites. The longitudinal impedance response of the CLEAR device was not significantly different than that of the platinum micro-ECoG array for a period of 70 days after implantation. Baseline neural signals and sensory evoked potentials were both successfully recorded with this device, and although there was a distinct photoelectric effect as a result of the optical stimuli, the stimulus artifact was distinguishable from the evoked neural response, just as in the case of the electrically evoked potentials shown in Figure 4.3(c). Fluorescence and OCT images were obtained through the graphene electrode sites with no perceptible artifact in the OCT signal. Although future studies will be necessary to determine the long-term stability of this device, both in terms of biocompatibility and recorded signal quality, these findings, and previous studies reporting the biocompatibility of CVD graphene, suggest that the CLEAR array is a viable micro-electrode array for neural interfacing applications.

Detailed Methods

Device Fabrication

Silicon wafers were coated with 15 microns of Parylene C using a CVD process (SCS Labcoter 2 Parylene Deposition System). 10 nm of chromium (for adhesion) and 200 nm of gold were evaporated onto the Parylene substrate and patterned using lift-off techniques to form connection pads and the initial portions of the electrode traces.

Graphene sheets were grown on copper foil following the procedure described in Appendix D. After metal deposition, four monolayers of graphene (MLGs) were transferred onto the substrate following the procedure described in Figure 4.7. The stacked graphene was then coated with a 30 nm SiO_2 sacrificial layer, to protect against damage during subsequent reactive ion etching (RIE) steps. Next,

the graphene and SiO_2 layers were patterned via RIE with oxygen plasma, to create 16 electrode sites connected to each of the gold pads.

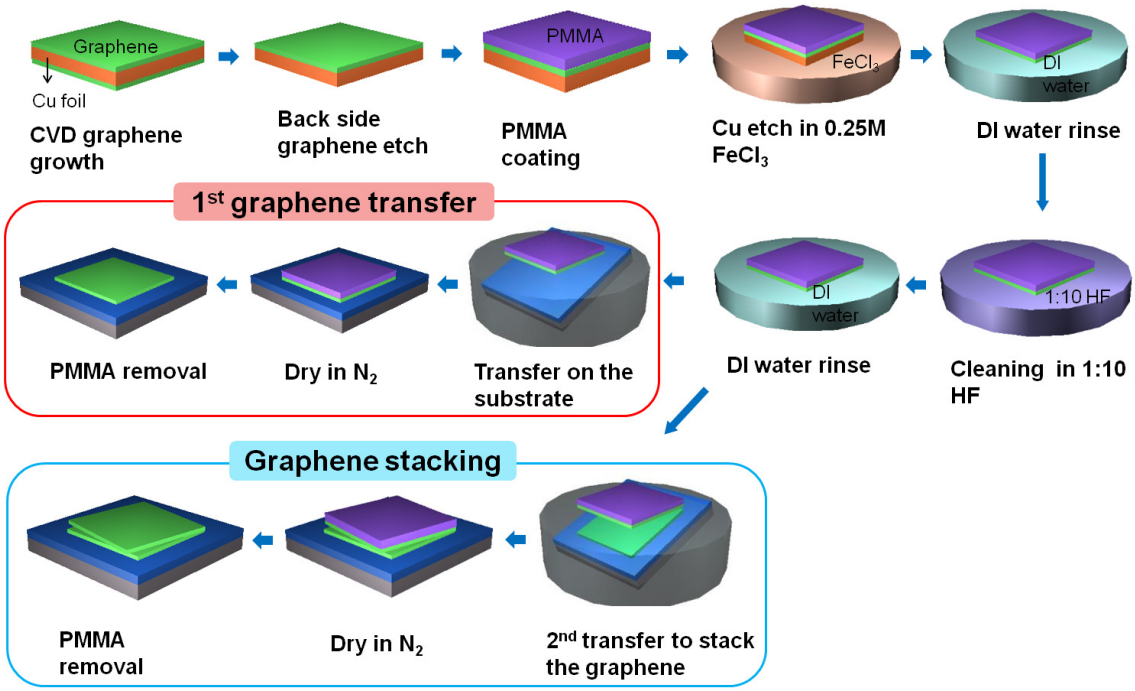

Figure 4.7. Graphene stacking process. The graphene stacking began with CVD graphene growth on a copper (Cu) foil. Mono-layer graphene was grown on both the top and bottom sides of the Cu foil. To utilize the top side graphene, back side graphene was etched using oxygen (O2) plasma (50W, 10 sccm O_2, 10 mTorr, for 1 minute). The top side graphene was coated by 950k PMMA (polymethyl methacrylate) C4 (MicroChem) to manipulate and protect the one-atom thick graphene. The Cu was etched in 0.25 M ferric chloride ($FeCl_3$) for 3 hours and rinsed in de-ionized (DI) water. The graphene was cleaned in 1:10 hydrofluoric (HF) acid for 1 hour to remove the copper composite residues and rinsed in DI water. The first graphene transfer was then performed on the desired substrate. SiO_2/Si substrates were used initially for fundamental characterizations and Parylene C/Si substrates for device fabrication. After drying the PMMA/graphene sample in a N_2 atmosphere dry box, the PMMA was removed using acetone and the sample was rinsed in DI water. Following the above procedure, the graphene stacking was performed on the previously graphene-transferred substrate. Multiple layers of graphene could be stacked on the desired substrate using this method.

Next, another 10 microns of Parylene C were deposited via CVD and patterned by photolithography and RIE, to create the array outlines and to open the electrode sites and pads. The arrays were released from the silicon wafer via immersion in de-ionized water. Finally, the protective SiO_2 layer was removed using 1:6 buffered oxide etchant (BOE). A polyimide stiffener was then bonded to the pad region of each device to increase the thickness of the array enough to ensure a good connection to the PCB. The detailed process diagram is provided in Figure 4.8.

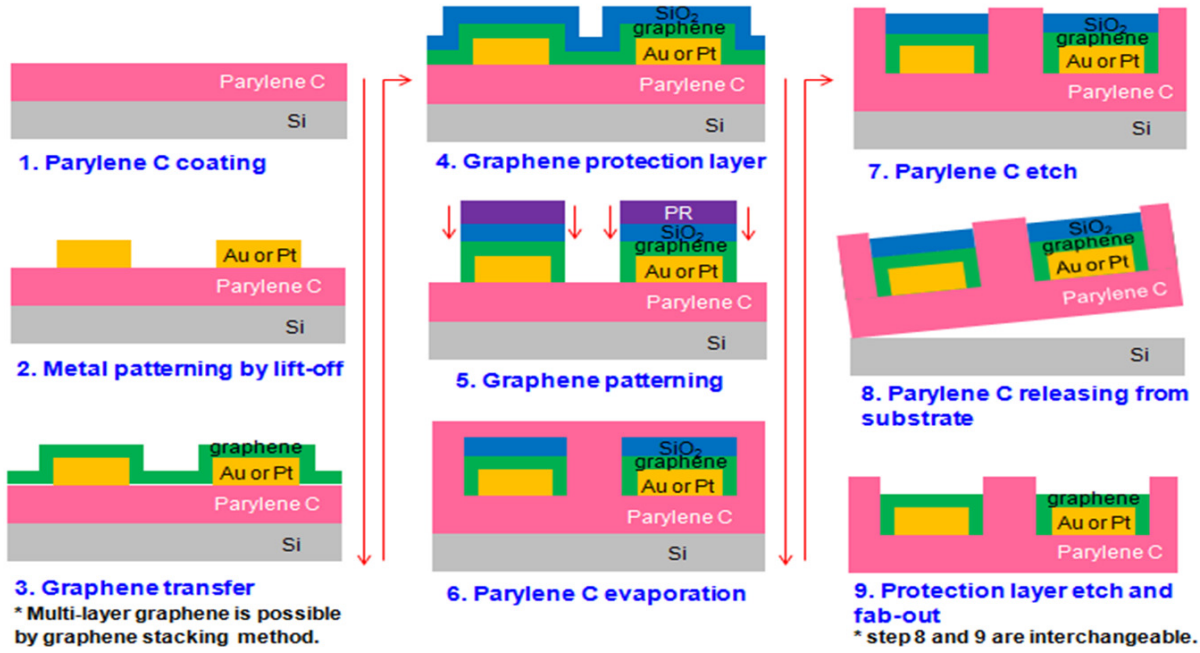

Figure 4.8. Detailed fabrication process flow illustration. Parylene C (15 μm) was coated on a 4-inch silicon (Si) wafer using Parylene deposition equipment (PDS 2010 Labcoter 2, Specialty Coating Systems Inc.). Electrode sites, traces, and pads were using Shipley 1813 photoresist and lift-off techniques. Gold (Au) metal was used with a chromium (Cr) adhesion layer. For the CLEAR device, only the pads and parts of the traces were patterned with metal, leaving the area of the device which would be in contact with the brain to be patterned with transparent graphene electrode sites and traces. Before graphene transfer, oxygen (O_2) plasma treatment was performed to transform the Parylene C surface from

hydrophobic to hydrophilic. Graphene was then transferred to the pre-patterned substrate using a wet transfer technique. To protect the graphene from possible damage during subsequent process steps, 30 nm SiO_2 was deposited using e-beam evaporation. Then, the SiO_2/graphene layers were patterned using photolithography and reactive dry etching. For the SiO_2 etch, reactive-ion etching (RIE) (Unaxis 790 dry etcher) was used with CF_4 gas at 45 sccm and O_2 gas at 5 sccm, 100W power, and 40mTorr pressure for 90 seconds. For the graphene etch, RIE with O_2 gas at 10 sccm, 50W power, and 10mTorr pressure was used for 60 seconds. After the photoresist was stripped, a second Parylene C layer (10 μm) was evaporated for encapsulation. The Parylene C was then patterned using two RIE steps with O_2 plasma. The first RIE step etched the device outline, and the second RIE step etched outline, holes, sites, and pads. Next, the wafer was soaked to release the devices from the silicon substrate. Finally, the SiO_2 protection layer was etched using 1:6 buffered oxide etchant (BOE) for 60 seconds, and the devices were rinsed thoroughly with DI water.

Surgical Implantation

The complete surgical implantation procedure has been described previously (Richner et al., n.d.; Schendel et al., 2013). Briefly, after receiving pre-operative injections of buprenorphine (for pain management) and dexamethasone (to prevent brain swelling), animals were anesthetized with isoflurane gas and their heads immobilized. Incisions were made over the top of the skull and craniotomies were made with an electric drill. Electrodes were stereotactically placed on the surface of the brain, over somatosensory cortex, and circular glass coverslips were applied over the top of the array, forming the cranial window. The edges of the coverslips were sealed to the skull using dental acrylic. Ground and reference wires were attached stainless steel screws, drilled into (rats) or glued to (mice) the skull. After everything was in place, the exposed screws were covered with dental acrylic to form a smooth cephalic implant. The skin was then sutured around the implant and the animals were revived. Animals received injections of buprenorphine post-surgery, as well as ampicillin antibiotic for one week following the implantation.

Electrical Evoked Potentials

In these experiments, the animals were anesthetized with dexmedetomidine hydrochloride (0.05 mg/kg, Orion Pharma), and their hind legs shaved. Two adhesive electromyogram (EMG) surface electrodes were attached to one leg at a time and held in place with tape. These electrodes were hooked up to a stimulation box (A-M Systems Isolated Pulse Stimulator, Model 2100) linked to the TDT RZ2 system via a BNC cable. The animal's electrodes were plugged into the RZ2 system via the TDT headstage and PZ2 amplifier. In this way, an electrical stimulus was sent to the animal's sciatic nerve from the RZ2 system, and the response in the somatosensory cortex was recorded through the CLEAR device and sent back to the computer. After completion, the animals were revived with an injection of atipamezole hydrochloride (0.3 mg/kg, Orion Pharma).

In Vivo Imaging

A full description of the *in vivo* vascular imaging procedure has been reported previously (Schendel et al., 2013). Imaging took place on a Leica MZ 16F stereoscope. Animals were anesthetized with a combination of isoflurane gas and dexmedetomidine, and kept on a heated water blanket. The animals' heads were stabilized to prevent breathing artifacts. Animals were injected with 12 mg/ml fluorescein-isothiocyanate labeled dextran dissolved in phosphate-buffered saline to make the blood vessels fluorescent under blue light. Bright field and fluorescent images were taken of the electrode arrays and surrounding brain tissue. Additionally, blood flow video recordings were acquired.

Optical Coherence Tomography

Angiograms were recorded by a homemade SD-OCT system with a 200 nm wide infrared source (THORLABS LS200B) a central wavelength of 1300 nm and an output power of 10 mW. The interference signal was projected onto an InGaAs 1024 pixel line CCD (GOODRICH LDH2) through a transmission grating (Wasatch Photonics, 1145 lines/mm). The system was designed to obtain 5μm axial

and 4μm lateral resolution with a 10x telecentric lens. To construct the angiograms a phase sensitive technique (Srinivasan et al) was applied to 10 cross sectional images taken at the same lateral position. Motion compensation and averaging were applied and the images were then stacked to create a 3D volumetric angiogram. A blurring kernel was applied to the 3D stack before performing a 2D maximum intensity projection.

Next, doppler blood flow data was collected. At each transverse position the interference pattern was recorded using the line CCD camera. Each A-scan was re-sampled to convert from wavelength to frequency space and its Fourier transform obtained. A complex B-scan was formed by concatenating positive frequencies, and was used to calculate the velocity profile.

5 CONCLUSIONS AND FUTURE DIRECTIONS

Conclusions

The work presented herein details specific protocols for the development and evaluation of micro-electrocorticography devices for neural interfacing applications. The focus of this research was to make design improvements to micro-ECoG devices which enhance long-term reliability and improve device functionality to meet the requirements of the field. In particular, *in vivo* evaluation of the chronic tissue response to epidurally implanted micro-ECoG devices has been discussed. An analysis of the impact of device geometry on scar tissue formation, and the fabrication and testing of a completely transparent, flexible, graphene-based micro-ECoG array were also presented.

The cranial window imaging study described in Chapter 2 outlines a method for the *in vivo* evaluation of tissue growth around chronically implanted surface electrode arrays. This method enables longitudinal observation of tissue growth, whereas traditional histological techniques only allow for evaluation at a single time point. In addition, the cranial window imaging technique is particularly advantageous for use with micro-ECoG devices, since they rest on the surface of the brain, and removal of the brain from the skull for traditional histological analysis can often result in the destruction of delicate interfacial tissues that grow around these types of devices. The initial study of vascularization around micro-ECoG devices implanted epidurally revealed the growth of blood vessels through fenestrations in the array substrates. This unexpected result sparked questions about whether tissue integration with these devices is beneficial or detrimental to long term device reliability and recorded signal quality, spurring the micro-ECoG footprint study presented in Chapter 3.

The cranial window imaging method was used to evaluate the tissue response to micro-ECoG devices with solid and open substrate geometries (Chapter 3). The results of this study revealed that the mesh-like micro-ECoG array allowed for easy tissue access to the top side of the device, while the solid electrode implantation resulted in thick tissue growth between the array and the brain. Although the

results of the electrode site impedance analysis did not indicate a difference between the impedance for the two types of devices, it is postulated that a longer-term study, or one performed in a larger animal model, would produce more significant results that might reveal impedance differences of a large scale. Based on the tissue thickness analysis results alone, it is proposed that an open-architecture geometry allowing for maximal tissue integration is beneficial for surface electrode array applications since the more open structure minimizes the thickening of tissue between the recording sites and the brain, which could cause a degradation of signal information.

Although the cranial window imaging method proved extremely useful for the observation of tissue growth around the micro-ECoG devices with platinum electrode sites, the development of the CLEAR device described in Chapter 4 greatly improved the ability to image tissues beneath the arrays. This will be especially useful for future studies involving analysis of the relationship between blood flow and neural activity, when it is desired to observe changes immediately below the recording sites. Additionally, Chapter 4 reports the successful use of the CLEAR device with optogenetic techniques, an application that has tremendous utility to current neuroscience researchers. Overall, the substitution of graphene for ITO as a transparent conductor in micro-ECoG arrays allows for the creation of more flexible devices with a simplified fabrication process.

Future Directions

The research described in this dissertation provides valuable insight into potential improvements for surface electrode array technology, however there is always room for further advancement. The reported work incites numerous questions and ideas for future studies focused on enhancing micro-ECoG biostability and function. Reported below are just a few possibilities. Each of these discussed possibilities is accompanied by promising initial research that should help frame further planning and experimentation.

Collagen Characterization

The results of the cranial window imaging studies reported in Chapters 2 and 3 revealed the formation of scar tissue around epidural micro-ECoG arrays. Histological analysis of this scar tissue using second harmonic generation imaging and H&E staining demonstrated that the tissue was collagenous in nature. To gain a better understanding of the benefits and downfalls of this tissue formation and what mitigation strategies would be appropriate, we must first improve our understanding of the composition of the tissue and the impact of the presence of the device on its formation. To do this, two separate approaches are recommended. First, antibody staining of the tissue could be performed to determine the type of collagen present, and second, collagen fiber behavior could be analyzed in terms of fiber length, alignment, and density, in samples from each of the different types of device implantation schemes (mesh, solid, fenestrated, and control) as well as in samples of cranial bone and dura mater, for comparison.

It is well-known that different types of collagen are present in different tissues (Brass et al., 1992; Chapman et al., 1990; Protasoni et al., 2011; Roggendorf et al., 1988). For example, granulation tissue is composed mainly of type III collagen, while type I collagen makes up mature scar tissue (Bailey et al., 1975; Gabbiani et al., 1976). Knowledge of the type of collagen present could be extremely beneficial to knowing whether the body is accepting the device or trying to wall it off from the surrounding tissues, and for determination of the maturity and health of the scar tissue (Bailey et al., 1975). Performance of the collagen type analysis would require the purchase of antibodies for each of the types of collagen to be assessed, and the development of immunohistochemical protocols for tissue staining. Comparison of the types of collagen present in the scar tissue surrounding micro-ECoG implants to those present in the dura mater, bone, and control window scar tissue could provide additional insight into the nature of the tissue response.

In addition to the deposition of particular collagen types, the morphology of collagen fibers has also been used as a readout for patient prognosis in cancer and other diseases (Danielson et al., 1997; Özer et al., 1999; Shirani et al., 2000). Therefore, it may be possible to glean information about device

suitability from knowledge of the collagen fiber architecture within the scar tissue. The CT-FIRE algorithm developed by Bredfeldt et al is a useful tool for extracting information about fiber angles, alignment, width, and length (Bredfeldt et al., 2014). This program has been used on some preliminary second-harmonic generation images of tissue samples from the animals used in this study. Figures 5.1 and 5.2 show examples of the algorithm output for images of scar tissue surrounding mesh and solid micro-ECoG arrays, respectively.

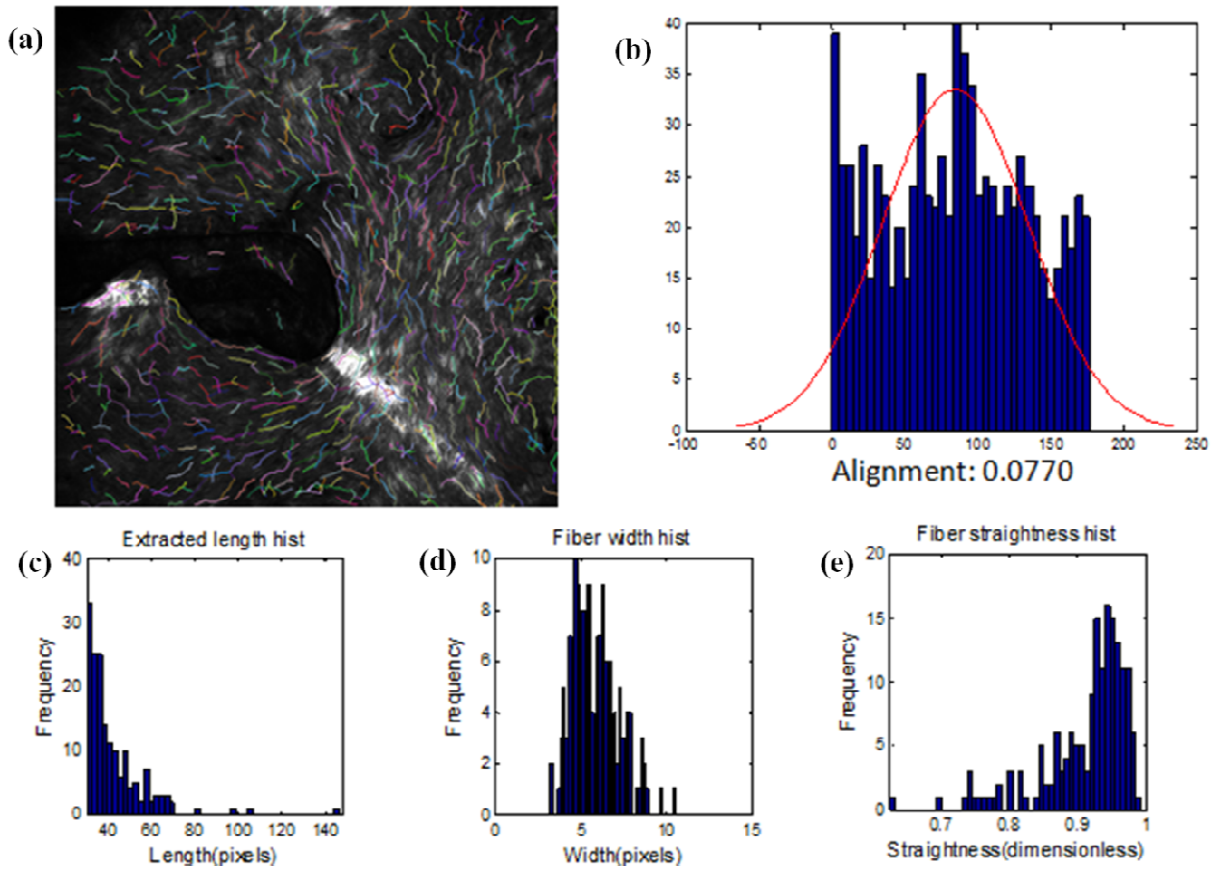

Figure 5.1. CT-FIRE analysis of collagen fibers in scar tissue around a mesh micro-ECoG trace. **(a)** Fibers extracted by the algorithm for analysis. **(b)** Alignment of fibers with respect to the positive x-axis. **(c)** Fiber length distribution **(d)** Fiber width distribution **(e)** Fiber straightness distribution.

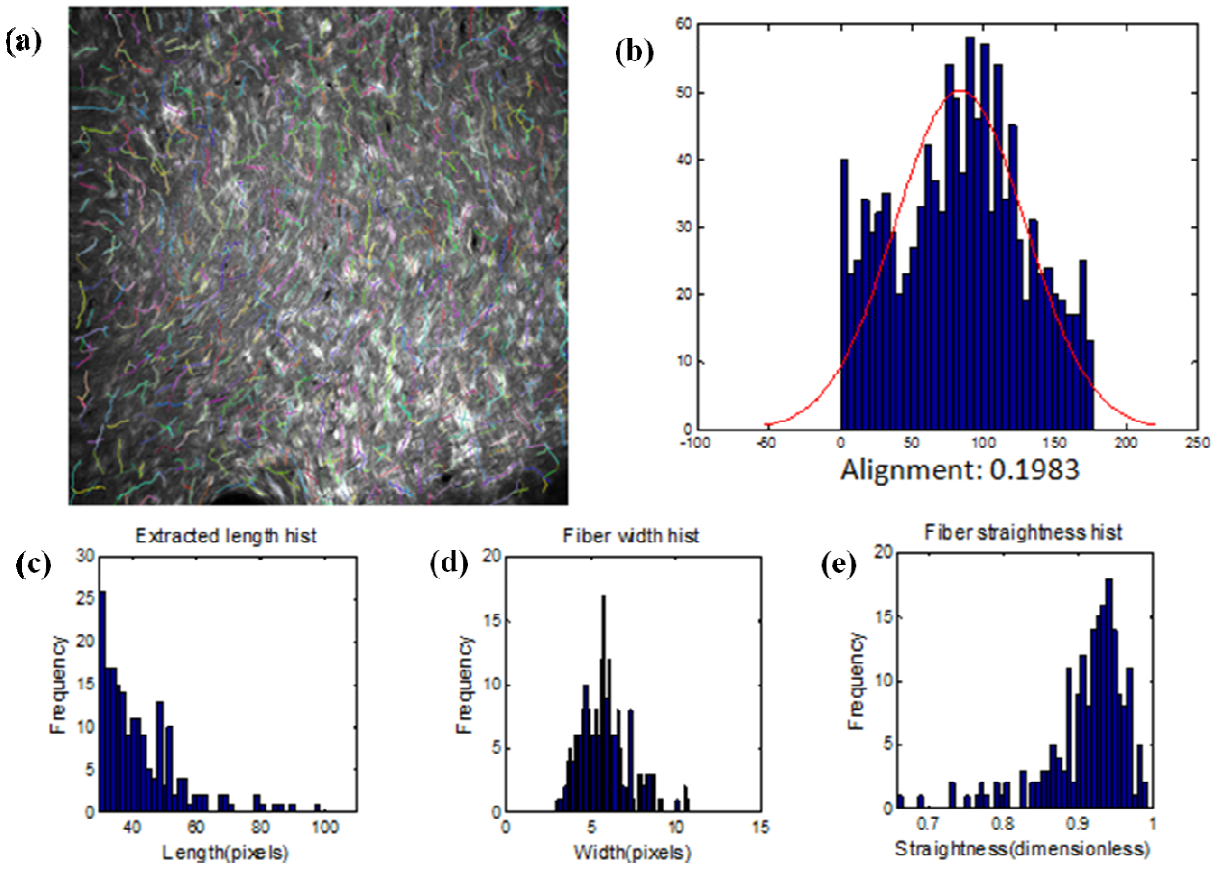

Figure 5.2. CT-FIRE analysis of collagen fibers in scar tissue around a solid micro-ECoG device in the same animal represented in Figure 5.1. **(a)** Fibers extracted by the algorithm for analysis. **(b)** Alignment of fibers with respect to the positive x-axis. **(c)** Fiber length distribution **(d)** Fiber width distribution **(e)** Fiber straightness distribution.

From the representative image analysis results in Figures 5.1 and 5.2, we can make a few observations. First, there appears to be a difference in alignment between the mesh and solid devices, both from the histograms in Figures 5.1(b) and 5.2(b) and the images themselves. It seems that the fibers in the tissue surrounding the mesh device may have some slight alignment with the outer edge of the substrate. To definitively determine whether this was true, it would be necessary to perform the analysis on a

particular section of the image near the edge of the device, to get a histogram for a more localized tissue region.

The next observation that we can make from these analyses is that the extraction of the collagen fiber data from the images is not 100% accurate. Looking at Figures 5.1(a) and 5.2(a), it is apparent that the fiber analysis algorithm has some difficulty in identifying the beginning and end points of all of the fibers, due to the complexity of the images. This means that, while the alignment data is probably fairly accurate, the fiber width and length information reported is inaccurate, due to the inability of the algorithm to identify the entirety of each fiber. Figure 5.3 shows the CT-FIRE analysis results for an SHG image of rat dura mater. The software does a better job of extracting these longer, more aligned fibers. This suggests that the algorithm has the potential for improved performance if the images analyzed were taken at a higher magnification, such that it is easier to identify each individual fiber.

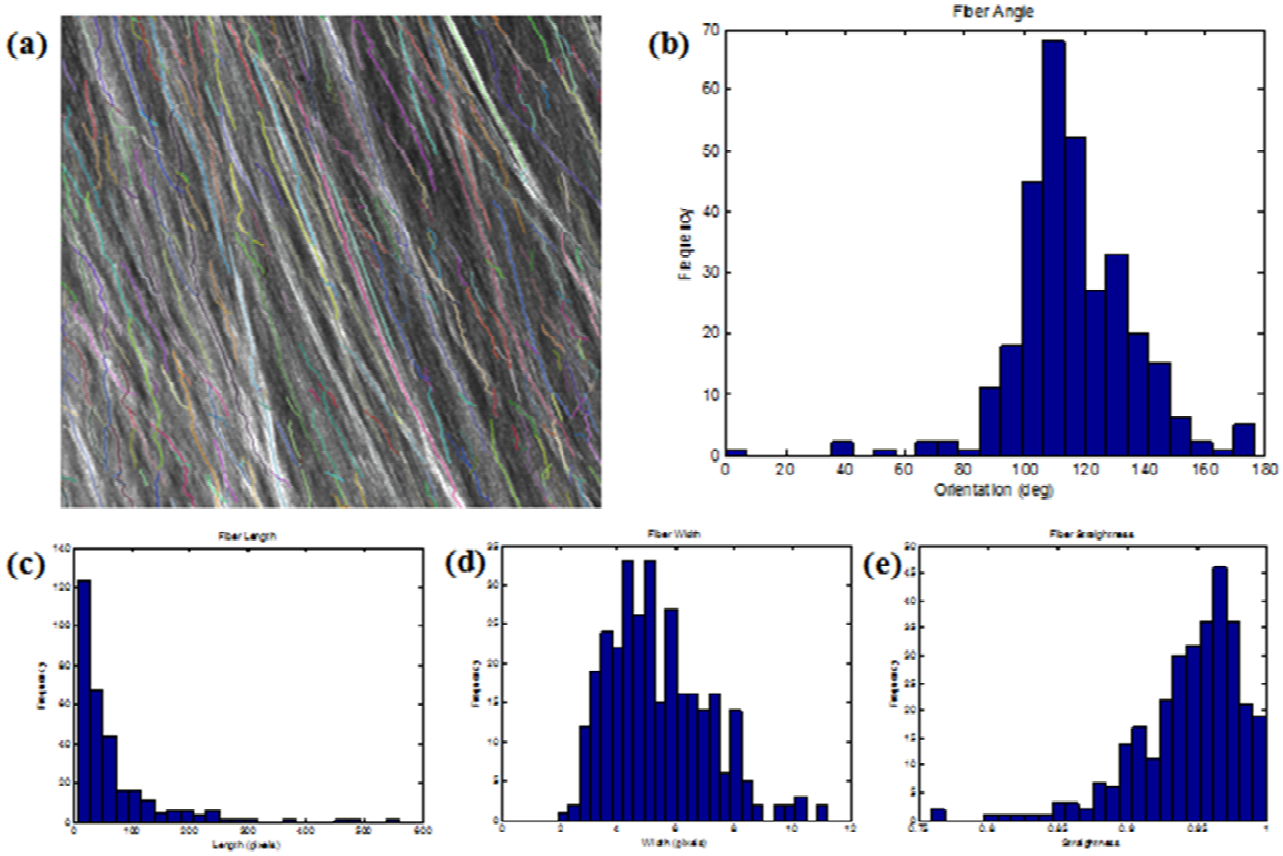

Figure 5.3. CT-FIRE analysis of dura mater. **(a)** Fiber extraction from SHG image **(b)** Fiber angle distribution. **(c)** Fiber length distribution (pixels). **(d)** Fiber width distribution (pixels) **(e)** Fiber straightness distribution.

Overall, the CT-FIRE algorithm could be an extremely useful tool for assessing the morphology of collagen fibers in scar tissue surrounding micro-ECoG devices. From these initial analyses, it appears that there could be a difference in the extent of collagen fiber alignment between two micro-ECoG devices of differing geometries, however many additional image sets will need to be analyzed to determine whether the difference is of any significance. In general, an assessment of the type of collagen present in the micro-ECoG scar tissue and its morphology could lead to the use of collagen information as a readout for determining the suitability of devices for neural interfacing applications.

Epidural vs. Subdural Implantation Comparison

Throughout the course of this study, a significant amount of time and effort has been devoted to the examination of collagen scar tissue formation around epidurally implanted micro-ECoG arrays, and strategies for minimizing the impact of this scarring on recorded signal quality. However, the results presented in Chapter 3, regarding the animal with the dural tear (Figure 3.4), suggest that this scarring could be strictly a meningeal response. Therefore, it would be of the utmost significance if a cranial window imaging study focusing on a comparison between scar tissue formation around subdurally and epidurally implanted arrays was performed.

Bundy et al have already performed a comparison of the effects of the human dura on the quality of macro and micro-electrocorticographic recordings (Bundy et al., 2014), with the finding that subdural implantation of macro-ECoG devices provided only small improvements in signal information, while epidural implantation of micro-ECoG arrays resulted in more significant signal quality enhancements. The results of this study solidify the existence of the already well-understood trade-off between

invasiveness and signal quality for neural MEA platforms. Although Bundy's study addresses in detail the electrophysiological aspects of this problem, it does not speak to the tissue response elicited by the differing device implantation schemes.

In a rat model, the effects of the dura mater on signal recording quality may not be as stark as in the human study, due to the thin nature of the rat meninges. However, a cranial window imaging study of the longitudinal tissue response to epidurally and subdurally implanted micro-ECoG arrays would lend insight into the types of tissue behavior which could be expected with long-term implantation of these devices. To achieve success with such a study, it may be necessary to enlist the aid of drugs or other methods to reduce bleeding during surgery and minimize the occurrence of blood pooling beneath the cranial windows following the durectomy. Overall, it should be possible to find simple mitigation strategies for this problem, and thus this study would be an easy follow up to the cranial window imaging studies reported in Chapters 2 and 3 of this manuscript. In addition, employment of the CLEAR device reported in Chapter 4 could also prove beneficial for assessing the tissue response occurring directly beneath the recording electrode sites, and could lead to an improvement on the data presented in Figure 3.12, which correlates the tissue growth around individual electrode sites with the electrical impedance data.

Drug delivery via Printing on Micro-ECoG Arrays

The results of the studies of vascular growth around chronically implanted micro-ECoG devices prompt the question of whether vascular growth is beneficial or detrimental to device function. Although we have tried to address this question through evaluation of the recorded signal quality by electrical impedance spectroscopy and baseline signal recordings, in conjunction with the cranial window imaging, there are many factors besides the growth of the vasculature around the implanted devices which could be contributing to signal quality changes. For example, there could be sub-cellular or cellular-scale reactions that cannot be visualized with the imaging techniques reported here. To isolate the vascular contribution

to electrode site impedance and signal quality changes, the application of drugs to impede or exacerbate angiogenesis could be utilized.

One method of delivering drugs directly to the area of interest is by adhering them to the surface of the implanted device. With the use of a SonoPlot microplotter (SonoPlot Inc, Middleton, WI), patterns of substances can be printed onto the surface of devices in a controlled manner. Preliminary tests have been performed in which inks and dyes have been printed onto the Parylene substrate of the micro-ECoG devices (Figure 5.4). The ability to pattern the drug onto the substrate is particularly advantageous if we want to avoid lowering the quality of the recorded signals, by applying the drug to the device substrate, but not the recording sites. Additionally, the impact of the vascular growth through the holes in the substrate could be evaluated by patterning angiogenic and anti-angiogenic substances only around the edges of the holes, and comparison studies could be performed in which half of the electrode is printed with drug, and the other half remains clear. One additional benefit to the SonoPlot technology is the ability to print substance gradients, in order to determine the effect of different drug concentrations and dosages.

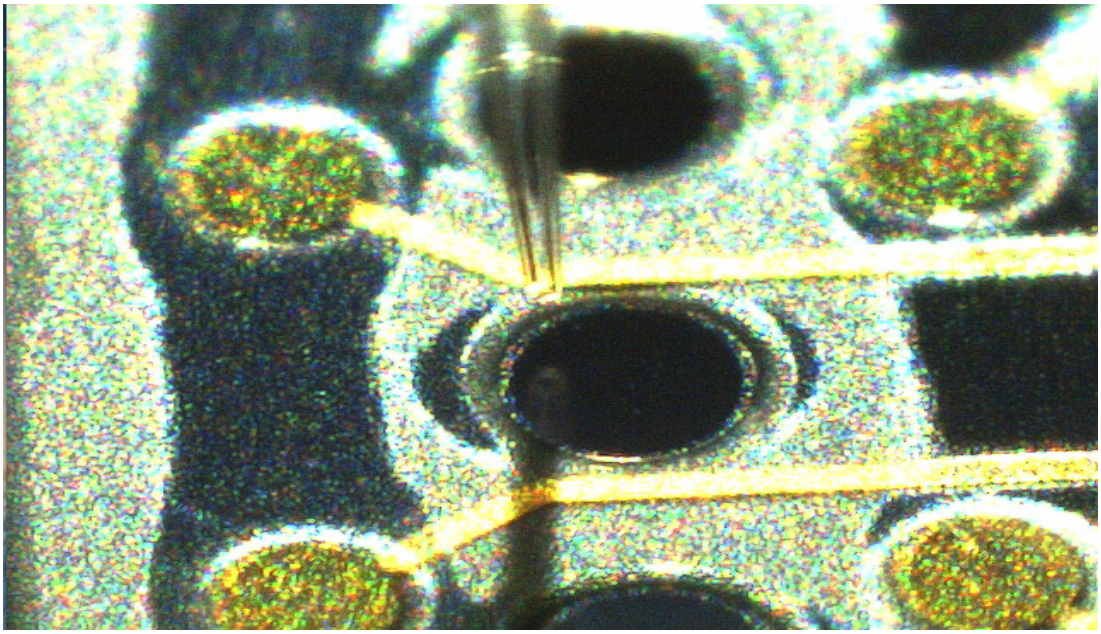

Figure 5.4. Image of the micro-pipette tip of the SonoPlot brought into close proximity with the substrate of the micro-ECoG device, in preparation to print liquid onto the surface of the device.

The delivery of safe drug dosages is a large concern in terms of targeted drug delivery (Freeman and Mayhew, 1986). To ensure that the desired substances are delivered in safe doses over an appropriate time period for the intended response, a controlled release system is necessary. Biodegradable polymers are commonly used vehicles for controlled drug delivery, which, as their name suggests, degrade over time when exposed to biological environments. These materials can be loaded with drug, which becomes entrapped between the crosslinks in the polymer chains. Once implanted in the body, the polymers begin to degrade, and the entrapped drug molecules diffuse out into the surrounding tissues. In this way, the amount of drug delivered to the tissue over time is better controlled than if the drug were to be directly applied to the tissue surface.

Poly(lactic-co-glycolic) acid (PLGA) is a biodegradable co-polymer commonly used for targeted drug delivery applications. PLGA is desirable for drug delivery because when it degrades it degrades into its monomeric elements, lactic acid and glycolic acid, which are both natural byproducts of metabolic processes, and so are not harmful to the body. Preliminary tests of the viability of PLGA for printing with the SonoPlot have been performed, and it was found that the viscosity of the PLGA liquid was conducive to SonoPlot patterning. In addition to printing tests, the adhesion properties of PLGA with the Parylene surface of the micro-ECoG devices were also evaluated. It was found that PLGA withstood initial saline soak tests at room temperature.

Additional research into the time-release characteristics of printed PLGA is necessary prior to deployment of this drug delivery method in an animal model. Next steps should include extended soak tests at body temperature to evaluate the dissolution rate. Following validation, drug-impregnated PLGA can be printed onto micro-ECoG arrays and implanted in rats beneath cranial windows, such that the effect of the drug on the tissue response to the implanted arrays can be monitored over time. Some drugs and factors that may be of interest for these studies include vascular endothelial growth factor (VEGF), which stimulates angiogenesis, Thalidomide, an angiogenesis inhibitor, and Clodronate liposomes, which can be used to induce apoptosis of macrophages and other phagocytic immune cells (D'Amato et al.,

1994; Gerhardt et al., 2003; Zeisberger et al., 2006). The use of the PLGA printing method to deliver these types of drugs and factors to the micro-ECoG implant site will allow for the ability to target specific cell types in our study of the tissue reaction to implanted surface electrodes, and will thus lead to a better understanding of the effect of individual cell and tissue types on recorded signal quality.

Integration of Microfluidics and Micro-ECoG

The integration of microfluidics and micro-electronics has proven advantageous for many applications, such as bio-sensing, cell electroporation, and drug delivery. In this section we discuss the incorporation of microfluidic channels into the micro-ECoG array for the purposes of focal brain cooling and cortical drug delivery.

Cortical Cooling Micro-ECoG Array Technology: The results of several research studies have demonstrated the use of focal brain cooling to reduce the amplitude of neural signals (Bakken et al., 2003; Bindman et al., 1963; Jasper et al., 1970; Lomber et al., 1999). The ability to reduce neural activity is not only useful as a research tool in terms of being able to study the function of different areas of the brain by reversibly turning them "on" and "off" (Lomber et al., 1999), but also for therapeutic applications, such as halting seizure activity, which is known to be caused by neural over-activity (Rothman et al., 2005; Tanaka et al., 2008). The integration of cortical cooling capabilities with micro-electrodes for recording neural activity would allow for a closed-loop system in which the beginnings of a seizure could be detected by the recording electrodes, and a command could be sent to open a gate and allow chilled fluid to flow through the micro-fluidic channel, cooling the brain and halting the seizure. In addition to studying neural function and creating a closed-loop seizure therapy device, a cortical cooling micro-ECoG device could be used in combination with the previously described cranial window vasculature imaging technique to study the effects of decreased cortical temperature on vascular perfusion and blood flow velocity, and ultimately their relationship with neural activity.

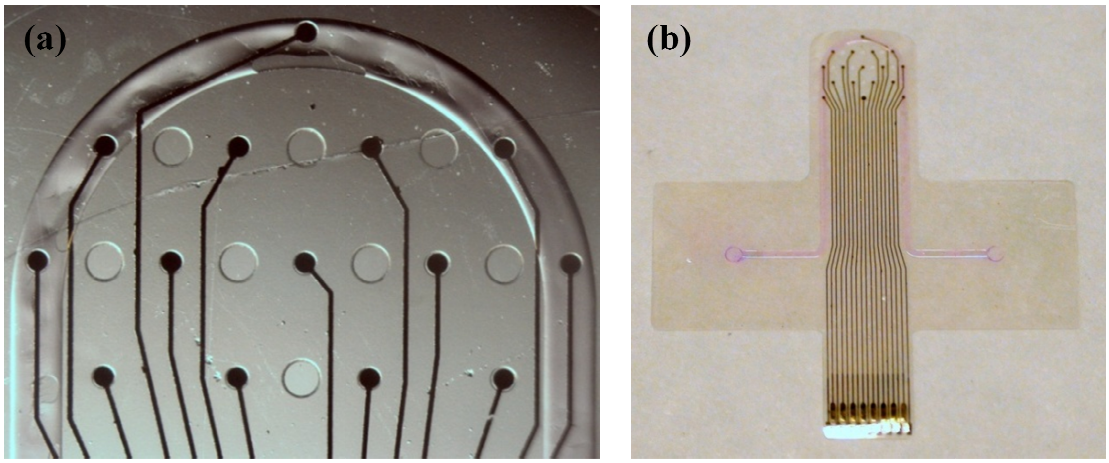

Figure 5.5. Cortical cooling micro-ECoG array. **(a)** Close-up of the cortical cooling device. Notice that some electrode sites sit atop the cooling channel, while others are far away, to determine the spread of the cooling effect on recorded neural activity. **(b)** Image of the entire device before the addition of the PCB connector and the nanoports for fluid injection.

Figure 5.5 shows an image of a prototype of the cortical cooling micro-ECoG device. Fabrication of the device was originally attempted with the use of a sacrificial photoresist layer to define the microfluidic channel (Takeuchi et al., 2005). However, it was found that the use of this technique was not ideal for the application, since it required long sonication times to remove the photoresist from the channel, resulting in bubbles between the Parylene layers and thus weak channels which were unable to withstand the pressures required to reach the appropriate flow velocities for cooling the brain.

To create stronger Parylene microchannels, a new fabrication method was adopted, as shown in Figure 5.6. In this process, a silicon mold was created by deep reactive ion etching (DRIE) a channel into a silicon wafer (Ziegler et al., 2006). The wafer was then coated with Chromium and Aluminum, which acted as a sacrificial layer and were dissolved away in the final step to release the devices from the silicon mold. Next, the wafer was soaked in a mixture of silane, de-ionized water, and isopropyl alcohol to promote adhesion between the deposited Parylene and the wafer substrate. This was necessary to

minimize bubble formation between Parylene layers and the substrate, since extraneous bubbles could lead to cracks, rendering the devices unusable.

After application of the adhesion promoter, 10 microns of Parylene were deposited onto the silicon mold as well as onto an unprocessed 3 inch silicon wafer, which was not exposed to adhesion promoter. After the Parylene deposition was complete, the mold wafer and the unprocessed wafer were sandwiched together with the Parylene-coated surfaces in contact. They were then placed in the Parylene bonding press (Figure 5.7), which consisted of two steel plates with bolts in each corner. A torque wrench was used to apply the same amount of pressure to each corner of the press. The amount of torque required on each bolt was calculated using Equation 5.1 (Ziegler et al., 2006):

$$M = F\mu\left(r + \frac{d}{2}\right), \qquad (5.1)$$

where M is the torque, F is the force required for bonding, μ is the coefficient of friction (taken to be 0.2 in this case), r is the radius of the screw head, and d is the diameter of the screw.

According to the literature, 4.9 MPa of pressure is sufficient to bond two Parylene layers (Ziegler et al., 2006). Using 3 inch wafers and 3/8 inch bolts, the required torque was computed to be 55.8 N-m, using Equation 5.1. Once the wafers were fixed in the bonding press, the press was set on the hotplate at 180^{o} C for two hours. After the device had cooled, the unprocessed carrier wafer was removed, leaving behind the Parylene layer that had been deposited onto it and creating a sealed micro-channel. Next, the electrode sites and traces were patterned onto the device and another insulating Parylene layer was deposited. Reactive ion etching (RIE) with oxygen plasma was used to etch away the Parylene, opening the electrode sites, and creating ports for the micro-channels. After etching was complete, the devices were released from the wafer by dissolution of the sacrificial aluminum layer. After the devices were fabricated, nanoports (Upchurch Scientific, N-333) were attached to the open ends of the micro-channels using two-part epoxy. These ports were used to connect tubing to the micro-channels so that the devices could be attached to a syringe pump, which would generate fluid flow through the channels.

Additionally, a PCB connector was attached to the device so that neural signals recorded by the electrode sites could be read into a computer.

Initial fluidic testing of devices fabricated with this process has revealed that the channels were able to withstand significantly higher flow rates than those devices fabricated using the sacrificial photoresist layer method. Electrical impedance spectroscopy results revealed that electrode sites were viable for recording neural signals (i.e. the impedances at 1 kHz frequency were less than 600 kOhms). These results are promising, however further bench testing will be necessary prior to *in vivo* implantation. For example, tests should be performed to determine the exact flow rates necessary to cool the brain by the desired amount to affect the neural signals. This could be done by measuring the temperature profile of a heated agarose gel when the cooling device is applied to its surface, or by creating a COMSOL model of the system. Additionally, the flow rate limit at which the channels burst should be determined such that the limit is not surpassed once the device is implanted in an animal. After all of the appropriate validation testing has been performed, this device has the potential to be a valuable tool for epilepsy therapy and the study of neural function.

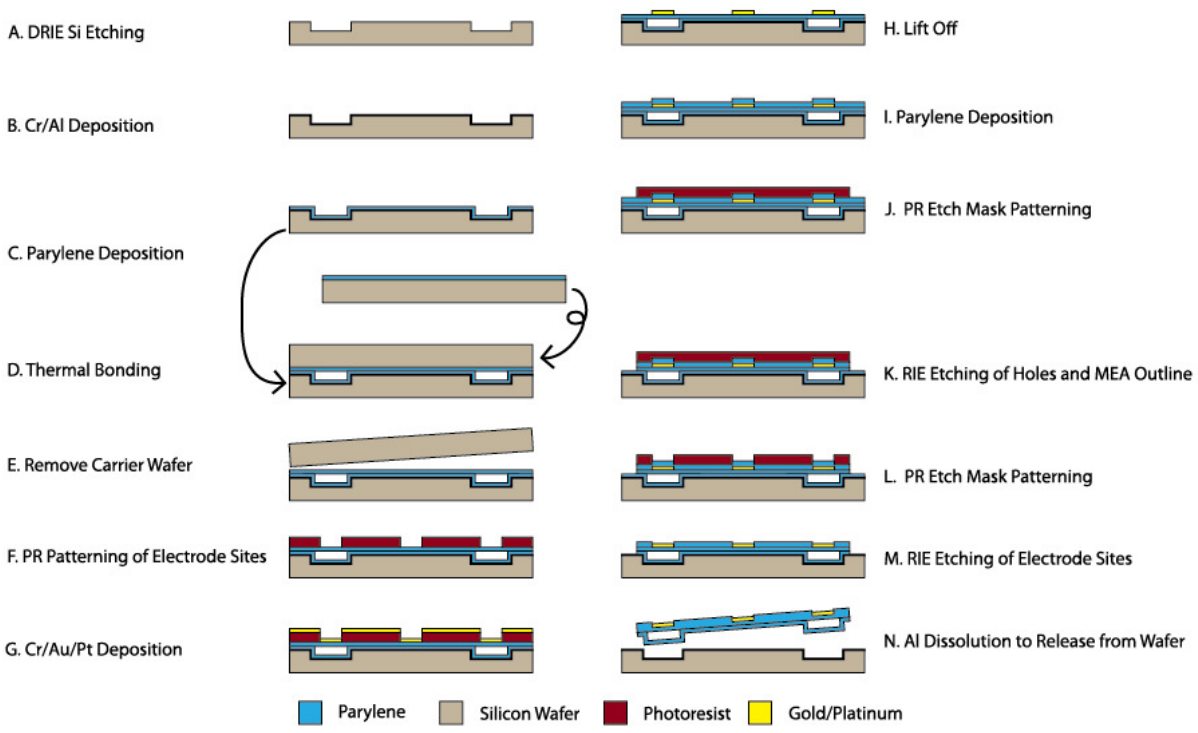

Figure 5.6. Fabrication process for the cortical cooling Micro-ECoG device. **(a)** Channels are etched into a silicon wafer using DRIE. **(b)** A sacrificial layer of Cr and Al is sputtered onto the wafer. **(c)** The etched wafer is coated with an adhesion promoter and 10 microns of Parylene is deposited onto the etched wafer as well as a blank silicon wafer. **(d)** The two wafers are sandwiched together between two steel plates and set on a hot plate for 2 hours at 180^{o} C. **(e)** The blank Si wafer is removed, leaving behind the Parylene layer, and thus forming the micro-channel. **(f)** Electrode sites and traces are patterned using Shipley 1813 photoresist. **(g)** 10 nm of chrome, 200 nm of gold, and then 10 nm of platinum are deposited using an electron beam evaporator. **(h)** Lift off techniques are used to remove the metal from the undesired areas. **(i)** A 5 micron layer of Parylene is deposited to insulate the traces. **(j)** An etch mask is patterned using AZ 4620 photoresist. **(k)** RIE is used to etch away Parylene, opening ports in the micro-channels and creating the outline of the device. **(l)** Another AZ 4620 photoresist etch mask is patterned. **(m)** RIE is used to open the electrode sites and finish forming the outline of the device. **(n)** Dissolution of the sacrificial aluminum layer is used to release the cortical cooling Micro-ECoG devices from the silicon wafer.

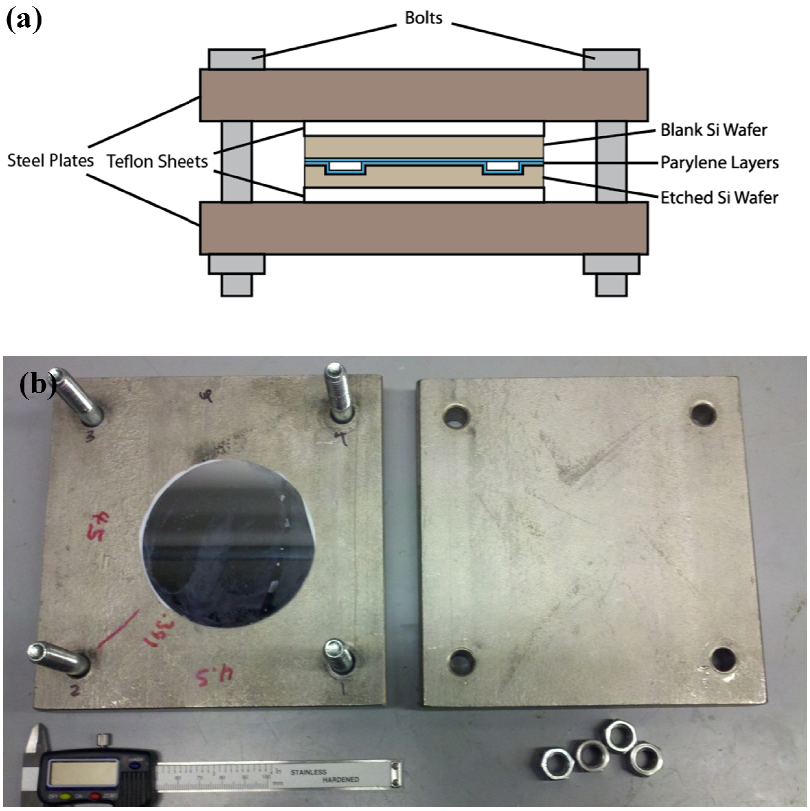

Figure 5.7. Parylene Bonding Press. **(a)** Schematic diagram of the Parylene bonding press. **(b)** Picture of the disassembled bonding press.

Microfluidic Micro-ECoG for Drug Delivery: The incorporation of microfluidic channels into micro-ECoG arrays can not only be used for isolated fluid flow over the surface of the brain to elicit temperature changes, but also for delivery of fluidic substances directly to neural tissue. Although the SonoPlot printing process described previously is a practical method for delivering drug to the implant site, it does have the downfall of only being able to apply the drug once, during the implantation surgery. A micro-ECoG device with an embedded perforated micro-fluidic channel could not only be used as a one-time use device into which drug (or drug-impregnated PLGA) is loaded prior to implantation and slowly diffuses out through holes in the channel into the surrounding tissue, but could also be employed as a re-loadable multi-use device, by attaching the nanoports described in the previous section, and using a syringe pump for controlled flow of drug through the channel and onto the cortical surface. Not only

would this re-usable drug delivery device allow for multiple drug delivery sessions, but it would also enable the administration of multiple drugs to a single animal.

Figure 5.8 shows an image of a microfluidic micro-ECoG device for drug delivery. The layout of the device is identical to that of the cortical cooling micro-ECoG device described in the previous section (Figure 5.5) , except that the microfluidic channel is perforated so that fluid could diffuse out of the channel and into the surrounding tissue. Although the design of this device is very similar to that of the cooling device, the fabrication process can be simplified by employing the use of a sacrificial photoresist layer to define the fluid channel, rather than using the Parylene bonding press method. This process modification can be made for two reasons; First, the holes in the channel allow for better perfusion of acetone during the sonication process to remove the photoresist layer. This means that the photoresist will be removed from the channel more quickly, and less sonication will be required, thus bubble formation between the Parylene layers will be less of an issue. The second reason for the process modification is that the addition of the holes decreases the pressure of the flowing fluid on the channel walls. Therefore, the channels for the drug delivery device do not have to withstand as much pressure as those for the cooling device, and thus the bond between the Parylene layers does not have to be quite as strong.

One batch of prototype devices has been fabricated using this method, however bench testing is required to verify the patency of these devices. Characterization of the fluid flow rates out of the channel will be necessary to determine the amount of drug delivered for a given syringe pump setting. This will be best validated by a combination of computer modeling and bench testing. Once the relationship between the syringe pump flow rate set-point, and the flow rate of drug through the channel perforations has been successfully characterized, the device could be implanted in an animal for cortical drug delivery studies.

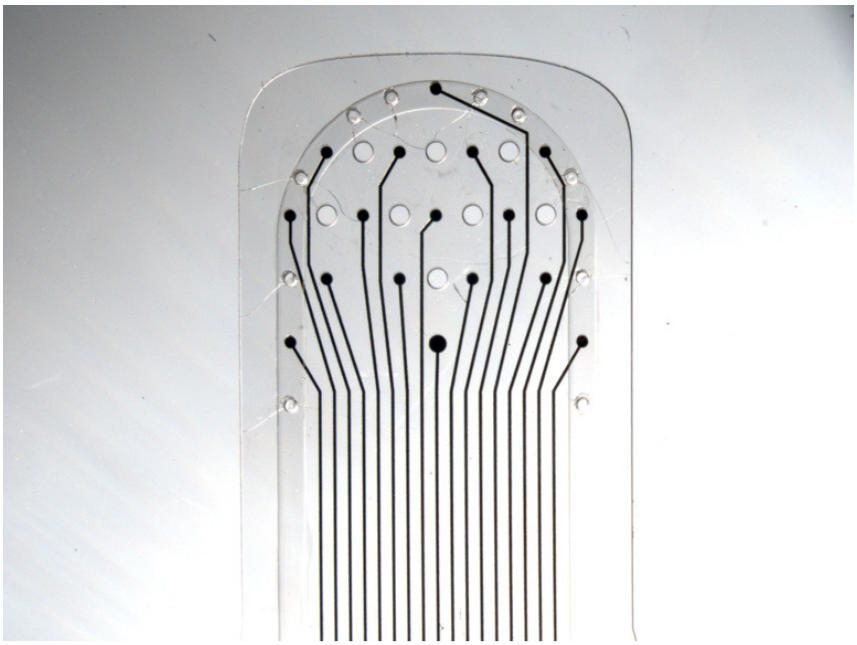

Figure 5.8. Microfluidic micro-ECoG array with perforated channel for cortical drug delivery.

CLEAR Contact Lens

Electroretinography is a widely used technology for monitoring retinal function (Marmor et al., 2004). This technique involves the placement of electrodes embedded into the surface of contact lenses onto the cornea, to measure electrical potentials which reflect retinal activity. Traditional electroretinography uses only a single electrode, but recently, multi-electrode devices have been fabricated using thin film Parylene technology similar to that employed in this study (Selner et al., 2011). This allows for the discernment of spatial variations in corneal potentials, which could lead to early detection of degenerative eye diseases.

Although the new multi-electrode electroretinogram (meERG) technology is a large improvement on traditional, single-electrode devices, the opaque metallic electrode sites positioned over the cornea partially occlude the vision of the patient, a potential confound for measurements involving electroretinogram recordings combined with visual tasks. This problem could be solved by the use of transparent conductive materials in meERG devices, however ITO, the traditionally used transparent conductive material is brittle, and not well-suited to conform to curved contact lens surfaces. The validation of the CLEAR device discussed in Chapter 4 demonstrates that flexible graphene sheets are a

viable alternative to ITO for biological thin-film transparent electronic applications. Since the CLEAR fabrication process is now well-established, the development of this technology for transparent meERG devices should easily follow, and would provide revolutionary enhancements to the existing meERG technology.

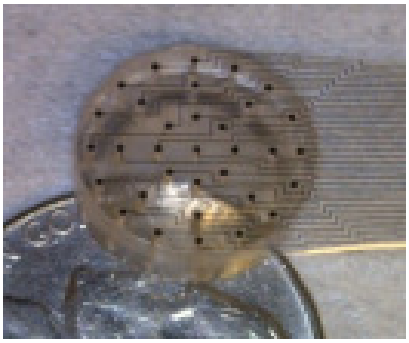

Figure 5.9. Multi-electrode electroretinogram device. (Selner et al., 2011)

Concluding Remarks

The continuously growing field of neural interfacing is an exciting area of research in today's science community. Constant improvements in the medical understanding of neural physiology combined with new and exciting technology advancements for the study of neural circuitry provide ample demand for neural interfaces with specialized functions tailored to a wide variety of applications. One particularly important focus for neural interfacing research that has gained popularity in the past few years has been the improvement of device biocompatibility and stability for applications requiring long-term implantation. Recently, micro-electrocorticography has emerged as a promising technology for neural prosthetic applications, as it strikes a delicate balance between invasiveness and recorded signal quality. The work presented here demonstrates device improvements for micro-ECoG interfaces to enhance long-term biostability as well as improve the properties of the devices to meet the requirements of today's research methodologies.

This work has not only demonstrated the use of two new micro-ECoG designs for enhanced long-term signal stability and for employment with optogenetic and imaging applications, but has also shown

an extremely valuable method for evaluating the *in vivo* tissue response to implanted arrays. Taken as a whole, these tools will be beneficial going forward, as they bring us one step closer to developing the ideal neural interface for chronic human implantation as part of a neural prosthetic system.

APPENDIX A DETAILED MICRO-ECOG FABRICATION PROCESS

Thin-film micro-electrocorticography arrays were developed in a cleanroom environment using micro-fabrication techniques involving chemical vapor deposition, photolithography, metalization, lift-off, and reactive ion etching techniques. The final devices were 25 µm thick and consisted of a Parylene C substrate with Chromium, Gold, and Platinum electrode sites. The detailed fabrication process is described in this appendix. Refer to Chapter 2, Figure 2.1 for a diagram of the process.

Required Materials:

- 4 inch Silicon Wafers
- Parylene C Dimer (SCS DPX-C dichloro-di-para-xylylene, Specialty Coating Systems)
- Microposit s1813 Photoresist (Shipley)
- Microposit MF-321 Developer (Shipley)
- DI Water
- Acetone
- Isopropyl Alcohol
- Chromium (99.99% pure) for Metal Evaporation
- Gold (99.99% pure) for Metal Evaporation
- Platinum (99.99% pure) for Metal Evaporation
- AZ P4620 Photoresist (AZ Electronic Materials)
- AZ 400K Developer (AZ Electronic Materials)
- Polyimide adhesive sheet (Pyralux LF Coverlay, Bondply & Sheet Adhesive 175 µm thick, Dupont)

Process Steps:

Step 1: Coat clean 4" silicon wafer with 15 um of Parylene C using SCS Labcoter 2 Parylene deposition system and 25 g of Parylene C dimer.

Step 2: Immediately prior to metalization, spin s1813 photoresist (PR) onto the Parylene-coated wafer at 4000 rpm for 30 s.

Step 3: Bake wafer for 1 min at 115^{o} C. To reduce PR and Parylene cracking, slow cool for 1 min by holding wafer over top of hot plate.

Step 3: Pattern electrode sites and traces onto wafer by exposing for 12 s with i-line UV light (365 nm wavelength), hard vacuum contact, and the appropriate mask.

Step 4: Develop wafer in MF-321 developer for 1 min.

Step 5: Rinse developer from wafer using DI water. Dry with compressed nitrogen.

Step 6: Clean surface of wafer with oxygen plasma prior to metal deposition by etching for 10 seconds in Unaxis 790 RIE using 150 W power and O2 gas.

> *Note: Performing lift-off photolithography immediately prior to the metalization session is recommended. Waiting too long between lithography and metalization will cause stronger bonding of photoresist to the substrate, requiring longer sonication times which could cause cracking and bubbling of the Parylene C.

Step 7: Deposit 10 nm of chromium (0.5 kÅ/s), 200 nm of gold (2 kÅ/s) , and 20 nm of platinum (0.3 Å/s) onto the patterned wafer using a CHA-600 electron beam evaporator.

Step 8: Lift-off undesired metal by sonicating the wafer in acetone (power 6-7). Once the majority of the metal is removed (5-10 min), use a soft q-tip to wipe away unwanted bits, in order to avoid cracking and bubbles in the Parylene coating.

Step 9: Rinse wafers with isopropyl alcohol and dry with compressed air.

Step 10: Bake on hot plate at 70^{o} C for 2 min to remove solvents.

Step 11: Deposit a second, 10 μm layer of Parylene onto the wafer using the SCS Labcoter 2 system and 16.67 g of dimer

Step 12: Spin a layer of AZ P4620 onto the wafer at 2000 rpm for 30s.

Step 13: Bake the wafer at 110^{o} C for 3 min and 10 seconds. Slow cool by holding the wafer above the hot plate for 2 min.

Step 14: Spin a second layer of AZ P4620 resist using the same spin parameters.

Step 15: Bake for 110^{o} C for 3 min and 10 seconds. Slow cool for 2 min.

Step 16: Expose for 3 min with i-line UV light (365 nm wavelength), hard vacuum contact, and the appropriate mask for patterning of device outline.

Step 17: Develop in AZ 400K developer mixed 1:3 with DI water for 2 min, and then rinse with water and dry wafer.

Step 18: Hard bake for 3 min and 10 seconds at 110^{o} C. Slow cool for 2 min by holding wafer above hot plate.

Step 19: Etch device outlines with oxygen plasma RIE for approximately 40 min at 200W power.

*For best results, validate Parylene and PR etch rates in RIE frequently and modify etch time accordingly.

Step 20: Strip photoresist from wafer using acetone and dry.

Step 21: Spin AZ P4620 resist onto wafer at 2000 rpm for 30 seconds.

Step 22: Bake at 110^{o} C for 3 min and 10 seconds, followed by 2 min of slow cooling.

Step 23: Spin a second layer of AZ P4620 resist onto wafer using the same spin parameters.

Step 24: Bake at 110^{o} C for 3 min and 10 seconds. Slow cool for 2 min.

Step 25: Expose wafer for 3 min using the previously described parameters, and the appropriate mask for opening the electrode sites and pads.

Step 26: Develop in AZ 400K developer mixed 1:3 with DI water for 2 min. Rinse wafer and dry.

Step 27: Hard bake at 110^{o} C for 3 min and 10 seconds, followed by a 2 min slow cool.

Step 28: Etch device outlines and electrode site and pad openings with RIE using oxygen plasma at 200 W for approximately 50 min.

Step 29: Analyze wafer using dark field microscopy to determine whether the electrode sites and pads have been completely cleared of Parylene. If not, an additional RIE step will be required.

Step 30: Strip PR with acetone, rinse wafer and dry.

Step 31: Remove devices from wafer by soaking in DI water and peeling them off with a tweezers.

Step 32: Dry devices by laying them on a cleanroom wipe.

Step 33: Cut polyimide stiffener sheets into appropriately sized rectangles to fit over the pad region of the arrays using a plotter cutter.

Step 34: Place micro-ECoG devices face-down on an aluminum foil-wrapped transparency sheet.

Step 35: Place polyimide stiffener sections with onto the pad regions of the micro-ECoG devices. Ensure that the sticky side (the non-lined side) is in contact with the Parylene substrate.

Step 34: Place micro-ECoG devices with polyimide sheets onto a hot plate and place a second aluminum foil-wrapped transparency on top, being careful not to dislodge the stiffener sheets from the devices.

Step 35: Using a pressure clamp to 230-250 kPa pressure, bond the polyimide sheets to the devices at 180^{o} C for 1 hour, and allow devices to slow cool.

Step 36: Assemble PCB connectors by attaching shrouds using superglue and soldering ground and reference wires to the appropriate vias.

Step 37: Insert devices into pre-assembled PCB connectors using the ZIF clip.

Step 38: Verify device patency by testing the electrode site impedance spectra in saline using the Autolab PGSTAT 12 potentiometer.

APPENDIX B CRANIAL WINDOW IMAGING PROCEDURE

The cranial window imaging method was used throughout this research study as a tool for evaluation of the longitudinal tissue response to chronically implanted micro-ECoG devices. Below is a detailed description of the procedure, which has been successfully employed in both mice and rats.

Required Supplies:

- Fluorescein Isothiocyanate-Dextran, MW 2,000,000, Sigma Aldrich
- Phosphate Buffered Saline Solution
- Dexmedetomidine Hydrochloride, Orion Pharma
- Atipamezole Hydrochloride, Orion Pharma
- Lidocaine Topical Anesthetic
- Isoflurane Gas Anesthetic and Regulator
- Stereotaxic Frame and Ear Bars
- Heated Water Blanket
- Isopropyl Alcohol
- Gauze
- 1 ml Syringes
- 25 Gage Needles
- Q-tips
- Pulse Oximeter
- Fluorescent Stereoscope and Light Source
- Opthalmic Ointment

Setup:

- Mix FITC-Dextran 12 mg/ml with sterile saline, 1 ml per rat to be imaged
- Set up microscope stage, light, isoflurane anesthesia regulator, water blanket, oxygen hose, etc.
- Draw up Dexmedetomidine (0.05-0.5 mg/kg)
- Boot the Leica program on the computer and setup a folder into which the images will be saved
- Change the camera exposure time to 100 ms and select the appropriate coloring
- Make sure the lever on the left of the microscope is moved into the "camera" position
- Make sure the filter ring is in the position with no label (no filter in place)

Imaging

Step 1: Administer Dexmedetomidine injection and hold animal in arms until he becomes still

Step 2: Place animal on heated blanket and put nose in oxygen

Step 3: Turn oxygen to 0.8-1 and turn isoflurane to 2%

Step 4: Place pulse oximeter on animal's hind paw and monitor oxygen and heart rate, oxygen level should not be below 94%, if it is, try repositioning the animal's head to open the airway and ensure that all of the hoses are hooked up correctly

Step 5: Once the animal is stable under the anesthesia, apply lidocaine to the inside of the ears with a q-tip and insert the ear bars

Step 6: Once the ear bars are in place, reduce the isoflurane level to 1%

Step 7: Place a folded paper towel under the animal's nose to keep it at the appropriate angle for an open airway, as well as to keep the window flat with the imaging plane

Step 8: Apply opthalmic ointment to both eyes with a q-tip

Step 9: Prop one edge of the stereotax up with padding so that the window to be imaged is flat with the viewing plane, turn on the light and bring the window into focus on the computer screen

Step 10: Swab the window with a small amount of isopropyl alcohol to remove debris

Step 11: When bright field imaging is complete, apply a glove filled with warmed water to the tail Swab tail and give FITC injection, being sure to change needles between each injection attempt

Step 12: Once FITC has been injected, turn on fluorescent lamp to right of computer, switch the filter ring to the position labeled GFP2, and open the shutter (located above the filter ring on the right side of the scope) to allow the blue light into the imaging field

Step 13: When imaging is complete, close the shutter and turn off the fluorescent lamp

Step 14: Level the animal, remove the ear bars, and turn the isoflurane to 0%, leaving the oxygen flow on

Step 15: Administer a subcutaneous injection of 0.02 ml of atipamezole, leaving the animal on oxygen until he is fully conscious

Step 16: Stimulate the animal to encourage wakefulness by gently rubbing his back, if the animal does not awake within 5 min of the injection, give another dose of 0.02 ml atipamezole.

Step 17: Once the animal is awake and active, return him to his cage

Step 18: Turn off the water blanket and drape it over the O2 tank, put away all equipment except the microscope stage, the isoflurane regulator and O2 tank, and the lamp.

APPENDIX C ESTIMATING REFRACTIVE INDEX USING OCT

OCT Specifications

The customized SD-OCT device that was used for this study uses an 8mW light source with spectral bandwidth of 200nm at the central wavelength of 1300nm. The interference patterns are captured by a 1024 pixel line-scan InGaAs camera capable of recording up to 91,900 axial scans per second. A 10x scan lens is used as the OCT objective with depth of focus of 160 µm. The zero path difference was set to 200 µm above the focal plane of the scan lens to take advantage of the whole depth of focus. The designed SD-OCT system provides transverse and axial resolution of 4µm and 5µm in free space, respectively.

Refractive Index Measurement

We estimated the refractive index of a sample by calculating the ratio of its optical to physical thickness. Both of these were obtained by processing the OCT image, similar to the method presented in ref (Tearney et al., 1995). The optical thickness of the specimen was calculated directly from the OCT image, while its physical thickness was assessed by detecting the increment introduced by the sample to the optical path length and cancelling it out from the optical thickness. As shown in Figure C.1, the increase in the optical path length (D) can be calculated by measuring the displacement observed in the OCT image of a flat surface beneath the sample. Therefore, if we denote the physical and optical thicknesses with L and L_O respectively, then refractive index can be calculated by:

$$n = \frac{L_O}{L} = \frac{L_O}{L_O - D} \quad (1)$$

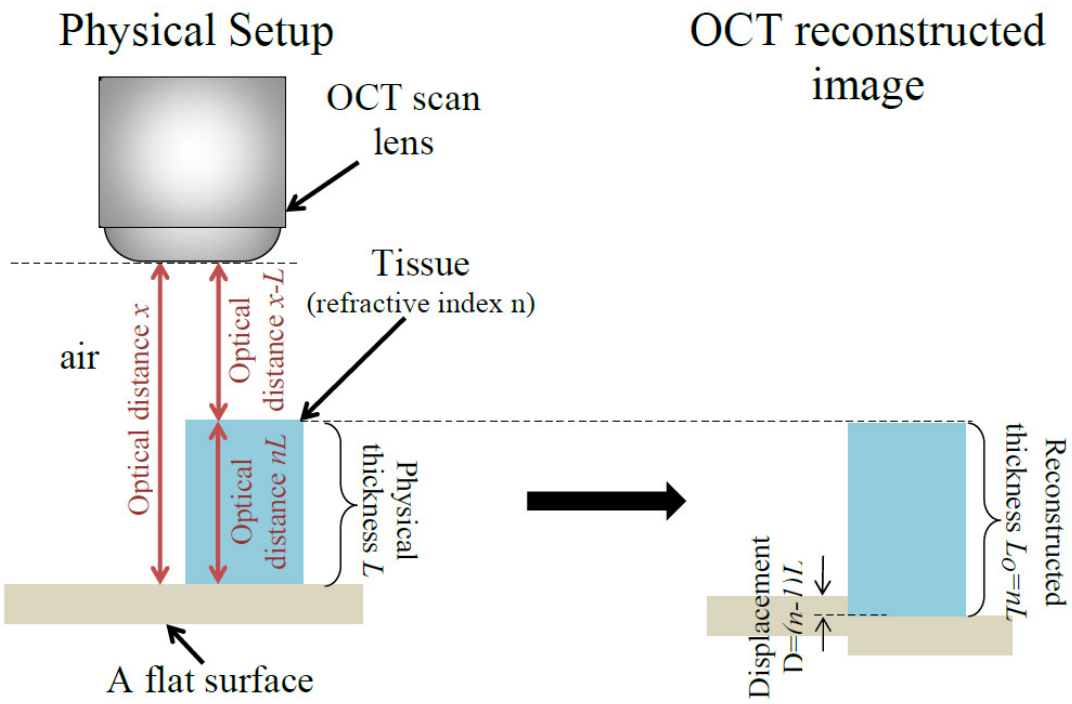

Figure C.1. The effect of change in the optical path on the reconstructed image.

Figure C.2(a) demonstrates an example of how refractive index was estimated using OCT scan of scar tissue. In this example, the displacement is D = 687−547 = 140 µm, and the thickness of the tissue is L_O = 656-219= 437 µm, which results in refractive index of $n = \frac{437}{437-140} = 1.47$.

By using this method, refractive indices of 15 samples were estimated and the results are shown in Figure C.2(b). The averaged refractive index was 1.39, while the standard deviation of the data was 0.0062, after removing the two outliers.

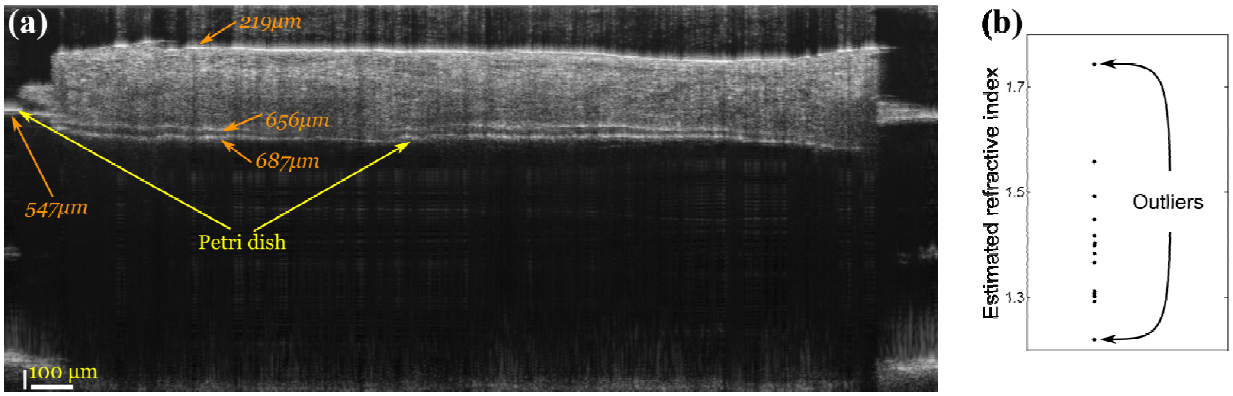

Figure C.2. Measurement of refractive index of scar tissue using SD-OCT. **(a)** an example data that was used to estimate the refractive index. Numbers in italic font specify the axial positions of corresponding points. **(b)** result of refractive index measurements for 15 samples in a petri dish.

APPENDIX D CLEAR DEVICE FABRICATION PROCESS

Required Materials:

- Copper Foil
- 4 inch Silicon Wafers
- Parylene C Dimer (SCS DPX-C dichloro-di-para-xylylene, Specialty Coating Systems)
- Microposit s1813 Photoresist (Shipley)
- Microposit MF-321 Developer (Shipley)
- DI Water
- Acetone
- Isopropyl Alcohol
- Buffered Oxide Etchant
- Chromium (99.99% pure) for Metal Evaporation
- Gold (99.99% pure) for Metal Evaporation
- Platinum (99.99% pure) for Metal Evaporation
- AZ P4620 Photoresist (AZ Electronic Materials)
- AZ 400K Developer (AZ Electronic Materials)
- Polyimide adhesive sheet (Pyralux LF Coverlay, Bondply & Sheet Adhesive 175 μm thick, Dupont)

Process Steps:

Step 1: Grow graphene sheets on 2x3 cm sheets of copper foil using a chemical vapor deposition system

Step 2: Coat clean 4" silicon wafer with 15 um of Parylene C using SCS Labcoter 2 Parylene deposition system and 25 g of Parylene C dimer.

Step 3: Immediately prior to metalization, spin s1813 photoresist (PR) onto the Parylene-coated wafer at 4000 rpm for 30 s.

Step 4: Bake wafer for 1 min at 115^{o} C. To reduce PR and Parylene cracking, slow cool for 1 min by holding wafer over top of hot plate.

Step 5: Pattern traces and connection pads onto wafer by exposing for 12 s with i-line UV light (365 nm wavelength), hard vacuum contact, and the appropriate mask.

Step 6: Develop wafer in MF-321 developer for 1 min.

Step 7: Rinse developer from wafer using DI water. Dry with compressed nitrogen.

Step 8: Clean surface of wafer with oxygen plasma prior to metal deposition by etching for 10 seconds in Unaxis 790 RIE using 150 W power and O2 gas.

> *Note: Performing lift-off photolithography immediately prior to the metalization session is recommended. Waiting too long between lithography and metalization will cause stronger bonding of photoresist to the substrate, requiring longer sonication times which could cause cracking and bubbling of the Parylene C.

Step 9: Deposit 10 nm of chromium (0.5 kÅ/s) and 200 nm of gold (2 kÅ/s) onto the patterned wafer using a CHA-600 electron beam evaporator.

Step 10: Lift-off undesired metal by sonicating the wafer in acetone (power 6-7). Once the majority of the metal is removed (5-10 min), use a soft q-tip to wipe away unwanted bits, in order to avoid cracking and bubbles in the Parylene coating.

Step 11: Rinse wafers with isopropyl alcohol and dry with compressed air.

Step 12: Bake on hot plate at 70^{o} C for 2 min to remove solvents.

Step 13: Transfer 4 monolayers of graphene from copper sheets to center of wafer, over the pre-patterned traces and pads, using a wet transfer method. This process is described in more detail in Appendix E. Also refer to Chapter 4, Figure 4.7 for a graphene wet stacking process flow diagram.

Step 14: Coat wafer with 30 nm SiO_2 layer for protection of graphene during subsequent etch steps, using electron beam evaporation.

Step 15: Spin s1813 photoresist onto wafer at 4000 RPM for 30 seconds

Step 16: Bake wafer for 1 min at 115^{o} C. To reduce PR and Parylene cracking, slow cool for 1 min by holding wafer over top of hot plate.

Step 17: Pattern electrode sites, traces, and connection pads onto wafer by exposing for 12 s with i-line UV light (365 nm wavelength), hard vacuum contact, and the appropriate mask.

Step 18: Develop wafer in MF-321 developer for 1 min.

Step 19: Rinse developer from wafer using DI water. Dry with compressed nitrogen.

Step 20: Use reactive ion etching to pattern the SiO_2 and graphene layers in the form of the electrode sites and traces. Use CF_4 gas at 45 sccm and O_2 gas at 5 sccm, with 100W power, and 40mTorr pressure for 90 seconds so etch the SiO_2 protection layer.

Step 21: Next, etch the unprotected graphene with an RIE process involving O_2 gas at 10 sccm, with 50W power and 10 mTorr pressure for 60 seconds

Step 22: Strip photoresist from wafer using acetone. Rinse with IPA, and dry.

Step 23: Deposit a second, 10 μm layer of Parylene onto the wafer using the SCS Labcoter 2 system and 16.67 g of dimer

Step 24: Spin a layer of AZ P4620 onto the wafer at 2000 rpm for 30s.

Step 25: Bake the wafer at 110^{o} C for 3 min and 10 seconds. Slow cool by holding the wafer above the hot plate for 2 min.

Step 26: Spin a second layer of AZ P4620 resist using the same spin parameters.

Step 27: Bake for 110^{o} C for 3 min and 10 seconds. Slow cool for 2 min.

Step 28: Expose for 3 min with i-line UV light (365 nm wavelength), hard vacuum contact, and the appropriate mask for patterning of device outline.

Step 29: Develop in AZ 400K developer mixed 1:3 with DI water for 2 min, and then rinse with water and dry wafer.

Step 30: Hard bake for 3 min and 10 seconds at 110^{o} C. Slow cool for 2 min by holding wafer above hot plate.

Step 31: Etch device outlines with oxygen plasma RIE for approximately 40 min at 200W power.

*For best results, validate Parylene and PR etch rates in RIE frequently and modify etch time accordingly.

Step 32: Strip photoresist from wafer using acetone and dry.

Step 33: Spin AZ P4620 resist onto wafer at 2000 rpm for 30 seconds.

Step 34: Bake at 110^{o} C for 3 min and 10 seconds, followed by 2 min of slow cooling.

Step 35: Spin a second layer of AZ P4620 resist onto wafer using the same spin parameters.

Step 36: Bake at 110^{o} C for 3 min and 10 seconds. Slow cool for 2 min.

Step 37: Expose wafer for 3 min using the previously described parameters, and the appropriate mask for opening the electrode sites and pads.

Step 38: Develop in AZ 400K developer mixed 1:3 with DI water for 2 min. Rinse wafer and dry.

Step 39: Hard bake at 110^{o} C for 3 min and 10 seconds, followed by a 2 min slow cool.

Step 40: Etch device outlines and electrode site and pad openings with RIE using oxygen plasma at 200 W for approximately 50 min.

Step 41: Analyze wafer using dark field microscopy to determine whether the electrode sites and pads have been completely cleared of Parylene. If not, an additional RIE step will be required.

Step 42: Strip PR with acetone, rinse wafer and dry.

Step 43: Remove devices from wafer by soaking in DI water and peeling them off with a tweezers.

Step 44: Remove SiO_2 layer from individual devices by wet etching in buffered oxide etchant for 60 seconds.

Step 45: Rinse devices in water and dry by laying them on a cleanroom wipe.

Step 46: Cut polyimide stiffener sheets into appropriately sized rectangles to fit over the pad region of the arrays using a plotter cutter.

Step 47: Place micro-ECoG devices face-down on an aluminum foil-wrapped transparency sheet.

Step 48: Place polyimide stiffener sections with onto the pad regions of the micro-ECoG devices. Ensure that the sticky side (the non-lined side) is in contact with the Parylene substrate.

Step 49: Place micro-ECoG devices with polyimide sheets onto a hot plate and place a second aluminum foil-wrapped transparency on top, being careful not to dislodge the stiffener sheets from the devices.

Step 50: Using a pressure clamp to 230-250 kPa pressure, bond the polyimide sheets to the devices at 180^{o} C for 1 hour, and allow devices to slow cool.

Step 51: Assemble PCB connectors by attaching shrouds using superglue and soldering ground and reference wires to the appropriate vias.

Step 52: Insert devices into pre-assembled PCB connectors using the ZIF clip.

Step 53: Verify device patency by testing the electrode site impedance spectra in saline using the Autolab PGSTAT 12 potentiometer.

APPENDIX E GRAPHENE TRANSER AND CHARACTERIZATION

Graphene Growth and Transfer

Graphene monolayers were grown on both sides of 2x3 cm sheets of copper (Cu) foil (Figure E.1). The graphene on one side of the foil was etched using oxygen (O2) plasma (50W, 10 sccm O_2, 10 mTorr, for 1 minute). The remaining graphene was coated by 950k PMMA (polymethyl methacrylate) C4 (MicroChem) for protection of the monolayer graphene during subsequent process steps. Next, the copper foil was etched away in 0.25 M ferric chloride ($FeCl_3$) for 3 hours and the sample was then rinsed in de-ionized (DI) water. After copper etching, the graphene/PMMA was cleaned in 1:10 hydrofluoric (HF) acid for 1 hour to remove any copper composite residues and then rinsed in DI water.

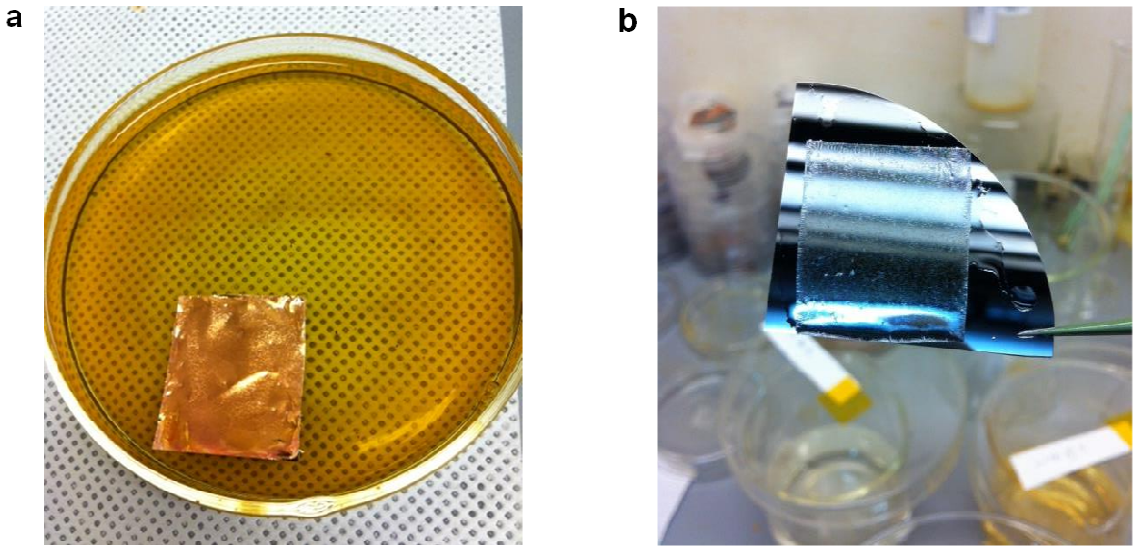

Figure E.1. CVD Graphene Images. The CVD graphene was grown on a 2 cm x 3 cm piece of copper (Cu) foil. **(a)** PMMA/graphene/Cu on Cu etchant ($FeCl_3$). **(b)** After the Cu was completely etched, the PMMA/graphene sheet was moved to DI water using a piece of silicon wafer.

To transfer the graphene sheet to the Parylene C coated silicon wafer substrate, it was necessary that the substrate surface be hydrophilic so that the graphene could adhere easily and uniformly. To

transform the intrinsically hydrophobic surface of Parylene C to hydrophilic, two methods were tested: (1) thin SiO_2 layer deposition. (2) Oxygen (O_2) plasma treatment. Figure E.2 shows the results for both methods. From this test, it was found that both plasma treatment and SiO_2 deposition allowed for sufficient wetting of the substrate surface. Since plasma treatment is a faster, more simple process, it was selected for use in this study.

Following plasma treatment of the substrate, the clean PMMA/graphene sample was dried in a nitrogen atmosphere dry box, and then transferred to the pre-patterned substrate. The PMMA was then removed using acetone and the sample was rinsed in DI water. Following the transfer of the initial sheet, the above process was repeated, transferring additional monolayer sheets onto the same spot until a 4-monolayer thick stack of graphene sheets was made. Figure E.3 shows examples of monolayer and multi-layer graphene sheets after transfer to the wafer.

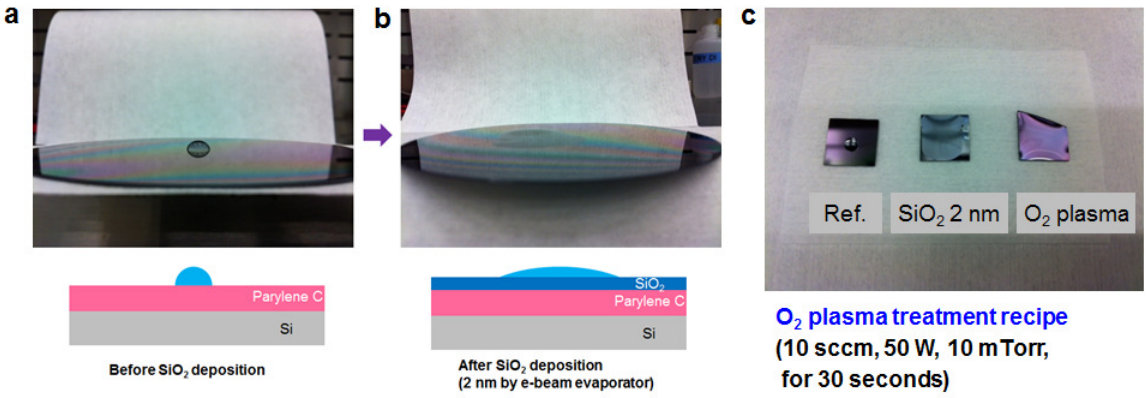

Figure E.2. Wetting property changes of Parylene C after oxygen plasma treatment and SiO_2 deposition . **(a)** Water droplet on hydrophobic Parylene C substrate prior to SiO_2 deposition. **(b)** Water droplet on hydrophilic Parylene C substrate post SiO_2 deposition. **(c)** Comparison of wetting properties for bare Parylene C, Parylene C with 2 nm of e-beam evaporated SiO_2, and oxygen plasma-treated (10 sccm, 50 W, 10 mTorr, 30 sec) Parylene C.

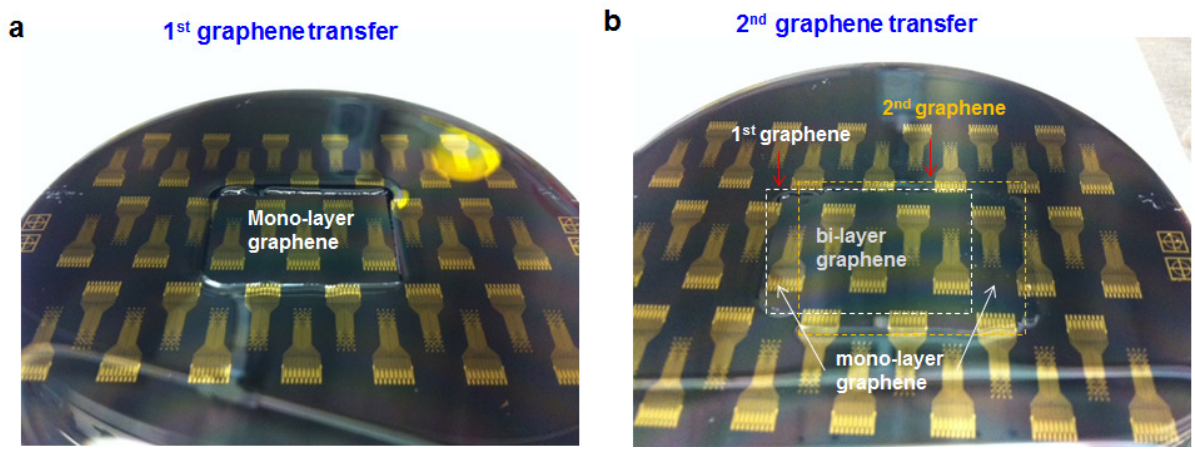

Figure E.3. Graphene sheets after transfer onto pre-processed wafer surfaces. **(a)** Monolayer graphene sheet after transfer onto a pre-processed Parylene-coated silicon wafer. DI water was poured onto the surface of the wafer for verification of the existence of the graphene sheet. Since graphene is intrinsically hydrophobic, due to the coherent bonding of carbon atoms, water does not spread onto the sheet, but instead flows onto the surrounding hydrophilic, plasma treated, Parylene C. **(b)** Same wafer shown in (a) after transfer of a second graphene sheet. The second graphene sheet was intentionally misaligned in this case to make both monolayer and bilayer regions, for comparison tests.

Graphene Characterization

The mono-layer graphene and multi-layer graphene samples were characterized using Raman spectroscopy and current-voltage (I-V) measurement on a SiO_2/Si substrate. Raman spectroscopy has been used as a fundamental method to investigate phonon characteristics of graphene, and can aid in identifying the existence of graphene on a particular substrate and the number of graphene layers present. The intensity ratio change of the 2D and G peaks for 1, 2, and 3-layer graphene verified the viability of the graphene stacking process, showing the unique phonon characteristics of graphene layers (Figure E.4).

The single sharp G peak is characteristic of the two-dimensional sp^2 bonded carbon atoms of graphene. For the 1 layer graphene, the G peak was located at 1572.5 cm^{-1}, and for the 3-layer graphene,

the G peak was at 1563.3 cm^{-1}. Therefore, as the number of graphene layers increased, the G peak showed a left shift (redshift). The 2D peaks were at 2633 cm^{-1} for the 1 layer graphene and at 2640.7 cm^{-1} for 3-layer graphene, showing that the 2D peak experienced a right shift (blueshift) with increasing graphene layers. These peak shift trends are consistent with the previous Raman study for multilayer graphene.

The 2D to G peak ratio (I_{2D}/I_G) trend shown in Figure E.4(d) demonstrates the changes occurring with the addition of each graphene layer. For the 1 layer graphene, the G peak intensity was the lowest, while the 2D peak intensity was the highest with I_{2D}/I_G = 3.63. As the number of graphene layer was increased, the G peak intensity was increased and the 2D peak intensity was decreased, resulting in I_{2D}/I_G ratios for 2-layer and 3-layer graphene were 1.43 and 0.91, respectively. This decreasing I_{2D}/I_G ratio is characteristic of multilayer graphene samples. It is also important to note that the D peak near 1350 cm^{-1}, which is generally a result of sample defects, was not significant for the graphene layers. This proves that the CVD graphene grown for this study did not have a significant number of defects before and after stacking.

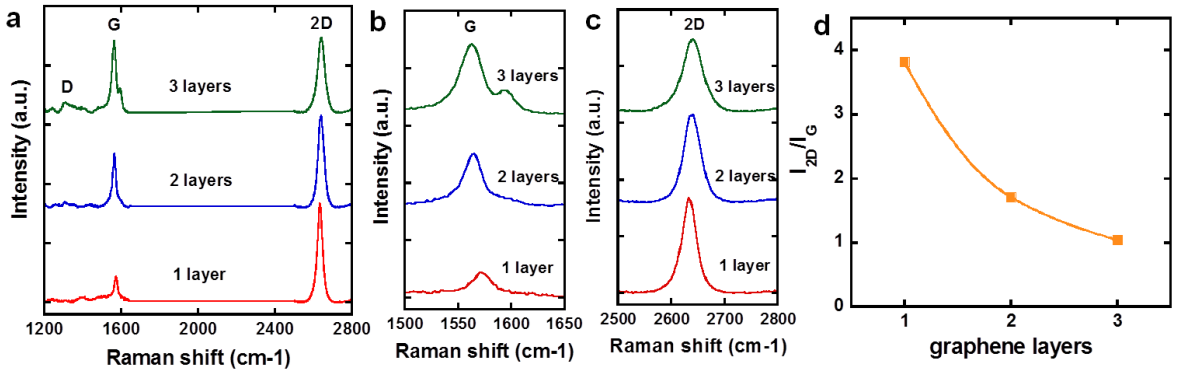

Figure E.4. Raman spectroscopy of stacked graphene. **(a)** G and 2D peaks for 1, 2, and 3-layer graphene. **(b)** and **(c)** Enlarged G and 2D peak regions, respectively. **(d)** G and 2D peak ratio (I_{2D}/I_G) trend versus number of graphene layers. The Raman spectroscopy was carried out with a Horiba LabRAM ARAMIS Raman system using a 532 nm green laser and a 100x objective.

To verify the resistance reduction effect of the stacked multilayer graphene, current-voltage (I-V) measurements were performed (Figure E.5). For comparison, 1, 2, and 3-layers of graphene were transferred on each SiO_2/Si substrate with the graphene and source/drain metal patterning shown in Figure E.5(d). The measured current values for the 2-layer graphene samples were about 1.6 times larger than those of the 1-layer graphene samples, while the 3-layer graphene sample showed about 1.85 times more current than the 1-layer graphene sheet. The resistance values extracted from the data indicate that the 2-layer and the 3-layer graphene samples have 0.62 and 0.55 times smaller resistances than the monolayer graphene sheet, respectively. From this data, we can hypothesize that further increase in the number of graphene layers will not substantially reduce sample resistance, however it will reduce transparency.

The sheet resistance for the 3-layer stacked graphene sample was calculated to be ~608 ohm/sq using the equation:

$$Sheet\ Resistance = \frac{Sample\ Resistance}{Sample\ Area} \qquad \text{(E.1)}$$

This value is higher than reported values for grown multilayer graphene or doped graphene (Bae et al., 2010; Kim et al., 2009). Note that the sheet resistance value obtained in this study was not from a four point probe method, and thus contains the contact resistance term. Although a lower sheet resistance is desired for electrode applications, it is more critical to have low and stable *in vivo* electrode site impedance for micro-ECoG applications.

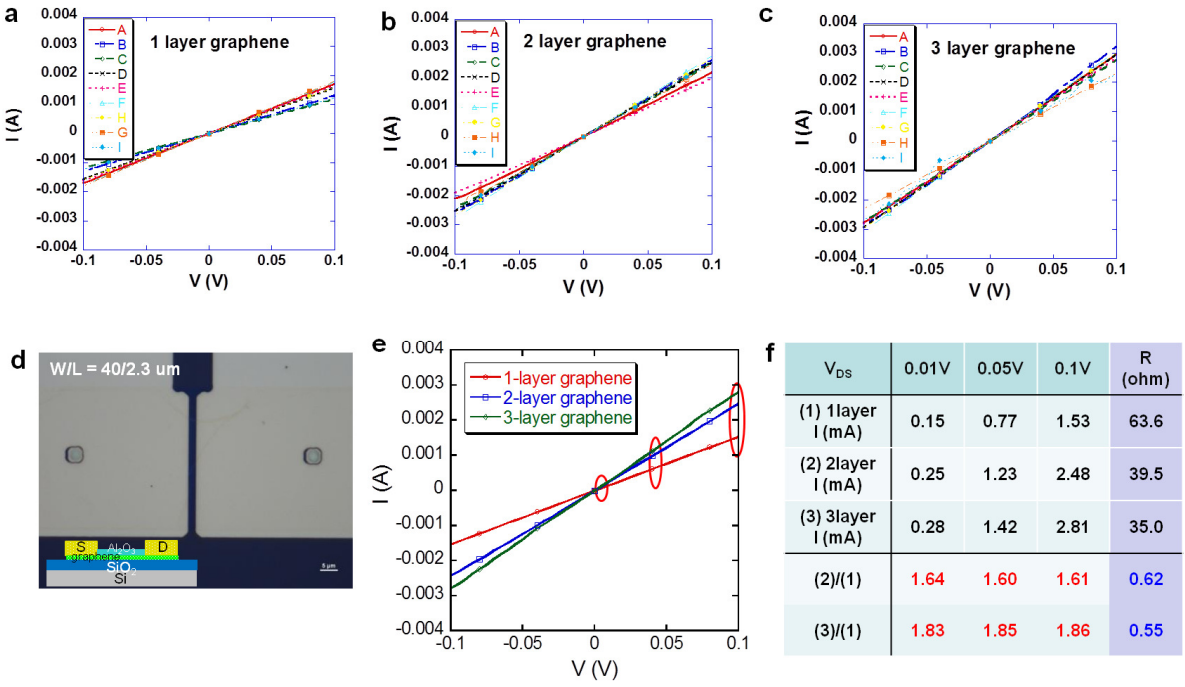

V_{DS}	0.01V	0.05V	0.1V	R (ohm)
(1) 1layer I (mA)	0.15	0.77	1.53	63.6
(2) 2layer I (mA)	0.25	1.23	2.48	39.5
(3) 3layer I (mA)	0.28	1.42	2.81	35.0
(2)/(1)	1.64	1.60	1.61	0.62
(3)/(1)	1.83	1.85	1.86	0.55

Figure E.5. Current-Voltage (I-V) measurements. **(a)**, **(b)**, and **(c)** I-V results for one-layer, two-layer, and three-layer graphene devices, respectively. **(d)** Structure of the test setup. The width and length of the graphene channels are 40 um and 2.3 um, respectively. **(e)** Average I-V results for one, two, and three-layer graphene. **(f)** Extracted current values for V_{DS} = 0.01 V, 0.05 V, and 0.1 V.

REFERENCES

Adrian, E.D., 1928. The basis of sensation.

Alwarappan, S., Erdem, A., Liu, C., Li, C.-Z., 2009. Probing the Electrochemical Properties of Graphene Nanosheets for Biosensing Applications. J. Phys. Chem. C 113, 8853–8857.

Arieli, A., Grinvald, A., Slovin, H., 2002. Dural substitute for long-term imaging of cortical activity in behaving monkeys and its clinical implications. J. Neurosci. Methods 114, 119–133.

Aronin, C.E.P., Sefcik, L.S., Tholpady, S.S., Tholpady, A., Sadik, K.W., Macdonald, T.L., Peirce, S.M., Wamhoff, B.R., Lynch, K.R., Ogle, R.C., Botchwey, E.A., 2010. FTY720 Promotes Local Microvascular Network Formation and Regeneration of Cranial Bone Defects. Tissue Eng. Part A 16, 1801–1809.

Bae, S., Kim, H., Lee, Y., Xu, X., Park, J.-S., Zheng, Y., Balakrishnan, J., Lei, T., Ri Kim, H., Song, Y.I., Kim, Y.-J., Kim, K.S., Özyilmaz, B., Ahn, J.-H., Hong, B.H., Iijima, S., 2010. Roll-to-roll production of 30-inch graphene films for transparent electrodes. Nat. Nanotechnol. 5, 574–578.

Bailey, A.J., Bazin, S., Sims, T.J., Le Lous, M., Nicoletis, C., Delaunay, A., 1975. Characterization of the collagen of human hypertrophic and normal scars. Biochim. Biophys. Acta BBA - Protein Struct. 405, 412–421.

Bakken, H.E., Kawasaki, H., Oya, H., Greenlee, J.D.W., Howard III, M.A., 2003. A device for cooling localized regions of human cerebral cortex. J. Neurosurg. 99, 604–608.

Bender, M., Trube, J., Stollenwerk, J., 1999. Deposition of transparent and conducting indium-tin-oxide films by the r.f.-superimposed DC sputtering technology. Thin Solid Films 354, 100–105.

Bernstein, J.G., Boyden, E.S., 2011. Optogenetic tools for analyzing the neural circuits of behavior. Trends Cogn. Sci. 15, 592–600.

Bettinger, C.J., Bruggeman, J.P., Misra, A., Borenstein, J.T., Langer, R., 2009. Biocompatibility of biodegradable semiconducting melanin films for nerve tissue engineering. Biomaterials 30, 3050–3057.

Bindman, L.J., Lippold, O.C.J., Redfearn, J.W.T., 1963. Comparison of the effects on electrocortical activity of general body cooling and local cooling of the surface of the brain. Electroencephalogr. Clin. Neurophysiol. 15, 238–245.

Brass, A., Kadler, K.E., Thomas, J.T., Grant, M.E., Boot-Handford, R.P., 1992. The fibrillar collagens, collagen VIII, collagen X and the C1q complement proteins share a similar domain in their C-terminal non-collagenous regions. FEBS Lett. 303, 126–128.

Bredfeldt, J.S., Liu, Y., Pehlke, C.A., Conklin, M.W., Szulczewski, J.M., Inman, D.R., Keely, P.J., Nowak, R.D., Mackie, T.R., Eliceiri, K.W., 2014. Computational segmentation of collagen fibers from second-harmonic generation images of breast cancer. J. Biomed. Opt. 19, 016007–016007.

Brown, E., Munn, L.L., Fukumura, D., Jain, R.K., 2010. In vivo imaging of tumors. Cold Spring Harb. Protoc. 2010, pdb.prot5452.

Brown, L.F., Yeo, K.T., Berse, B., Yeo, T.K., Senger, D.R., Dvorak, H.F., Water, L. van de, 1992. Expression of vascular permeability factor (vascular endothelial growth factor) by epidermal keratinocytes during wound healing. J. Exp. Med. 176, 1375–1379.

Bundy, D.T., Zellmer, E., Gaona, C.M., Sharma, M., Szrama, N., Hacker, C., Freudenburg, Z.V., Daitch, A., Moran, D.W., Leuthardt, E.C., 2014. Characterization of the effects of the

human dura on macro- and micro-electrocorticographic recordings. J. Neural Eng. 11, 016006.

Campagnola, P.J., Millard, A.C., Terasaki, M., Hoppe, P.E., Malone, C.J., Mohler, W.A., 2002. Three-dimensional high-resolution second-harmonic generation imaging of endogenous structural proteins in biological tissues. Biophys. J. 82, 493–508.

Castagnola, E., Maiolo, L., Maggiolini, E., Minotti, A., Marrani, M., Maita, F., Pecora, A., Angotzi, G.N., Ansaldo, A., Fadiga, L., Fortunato, G., Ricci, D., 2013. Ultra-flexible and brain-conformable micro-electrocorticography device with low impedance PEDOT-carbon nanotube coated microelectrodes, in: 2013 6th International IEEE/EMBS Conference on Neural Engineering (NER). Presented at the 2013 6th International IEEE/EMBS Conference on Neural Engineering (NER), pp. 927–930.

Cazorla, M., de Carvalho, F.D., Chohan, M.O., Shegda, M., Chuhma, N., Rayport, S., Ahmari, S.E., Moore, H., Kellendonk, C., 2014. Dopamine D2 Receptors Regulate the Anatomical and Functional Balance of Basal Ganglia Circuitry. Neuron 81, 153–164.

Chapman, D., Weber, K.T., Eghbali, M., 1990. Regulation of fibrillar collagen types I and III and basement membrane type IV collagen gene expression in pressure overloaded rat myocardium. Circ. Res. 67, 787–794.

Chen, H., Müller, M.B., Gilmore, K.J., Wallace, G.G., Li, D., 2008. Mechanically Strong, Electrically Conductive, and Biocompatible Graphene Paper. Adv. Mater. 20, 3557–3561.

Cui, X., Hetke, J.F., Wiler, J.A., Anderson, D.J., Martin, D.C., 2001. Electrochemical deposition and characterization of conducting polymer polypyrrole/PSS on multichannel neural probes. Sens. Actuators Phys. 93, 8–18.

Cui, X., Martin, D.C., 2003. Electrochemical deposition and characterization of poly(3,4-ethylenedioxythiophene) on neural microelectrode arrays. Sens. Actuators B Chem. 89, 92–102.

D'Amato, R.J., Loughnan, M.S., Flynn, E., Folkman, J., 1994. Thalidomide is an inhibitor of angiogenesis. Proc. Natl. Acad. Sci. 91, 4082–4085.

Daniels, J.T., Schultz, G.S., Blalock, T.D., Garrett, Q., Grotendorst, G.R., Dean, N.M., Khaw, P.T., 2003. Mediation of Transforming Growth Factor-β1-Stimulated Matrix Contraction by Fibroblasts: A Role for Connective Tissue Growth Factor in Contractile Scarring. Am. J. Pathol. 163, 2043–2052.

Danielson, K.G., Baribault, H., Holmes, D.F., Graham, H., Kadler, K.E., Iozzo, R.V., 1997. Targeted Disruption of Decorin Leads to Abnormal Collagen Fibril Morphology and Skin Fragility. J. Cell Biol. 136, 729–743.

Deisseroth, K., 2011. Optogenetics. Nat. Methods 8, 26–29.

Drew, P.J., Shih, A.Y., Driscoll, J.D., Knutsen, P.M., Blinder, P., Davalos, D., Akassoglou, K., Tsai, P.S., Kleinfeld, D., 2010. Chronic optical access through a polished and reinforced thinned skull. Nat Meth 7, 981–984.

Dvorak, H.F., Brown, L.F., Detmar, M., Dvorak, A.M., 1995. Vascular permeability factor/vascular endothelial growth factor, microvascular hyperpermeability, and angiogenesis. Am. J. Pathol. 146, 1029–1039.

Ellmer, K., 2012. Past achievements and future challenges in the development of optically transparent electrodes. Nat. Photonics 6, 809–817.

Foley, C.P., Nishimura, N., Neeves, K.B., Schaffer, C.B., Olbricht, W.L., 2012. Real-time imaging of perivascular transport of nanoparticles during convection-enhanced delivery in the rat cortex. Ann. Biomed. Eng. 40, 292–303.

Fong, J., Bingaman, W., Alexopoulos, A., Prayson, R., 2010. Iatrogenic Patholical Findings Related to Invasive EEG Monitoring of Medically Intractable Epilepsy.

Fong, J.S., Alexopoulos, A.V., Bingaman, W.E., Gonzalez-Martinez, J., Prayson, R.A., 2012. Pathologic Findings Associated With Invasive EEG Monitoring for Medically Intractable Epilepsy. Am. J. Clin. Pathol. 138, 506–510.

Freeman, A.I., Mayhew, E., 1986. Targeted drug delivery. Cancer 58, 573–583.

Fukumura, D., Xu, L., Chen, Y., Gohongi, T., Seed, B., Jain, R.K., 2001. Hypoxia and Acidosis Independently Up-Regulate Vascular Endothelial Growth Factor Transcription in Brain Tumors in Vivo. Cancer Res. 61, 6020 –6024.

Gabbiani, G., Lous, M.L., Bailey, A.J., Bazin, S., Delaunay, A., 1976. Collagen and myofibroblasts of granulation tissue. Virchows Arch. B 21, 133–145.

Garkavtsev, I., Kozin, S.V., Chernova, O., Xu, L., Winkler, F., Brown, E., Barnett, G.H., Jain, R.K., 2004. The candidate tumour suppressor protein ING4 regulates brain tumour growth and angiogenesis. Nature 428, 328–332.

Gerhardt, H., Golding, M., Fruttiger, M., Ruhrberg, C., Lundkvist, A., Abramsson, A., Jeltsch, M., Mitchell, C., Alitalo, K., Shima, D., 2003. VEGF guides angiogenic sprouting utilizing endothelial tip cell filopodia. J. Cell Biol. 161, 1163–1177.

Gierthmuehlen, M., Ball, T., Henle, C., Wang, X., Rickert, J., Raab, M., Freiman, T., Stieglitz, T., Kaminsky, J., 2011. Evaluation of μECoG electrode arrays in the minipig: Experimental procedure and neurosurgical approach. J. Neurosci. Methods 202, 77–86.

Green, R.A., Lovell, N.H., Wallace, G.G., Poole-Warren, L.A., 2008. Conducting polymers for neural interfaces: Challenges in developing an effective long-term implant. Biomaterials 29, 3393–3399.

Grill, W.M., Mortimer, J.T., 1998. Stability of the input-output properties of chronically implanted multiple contact nerve cuff stimulating electrodes. Rehabil. Eng. IEEE Trans. On 6, 364–373.

Gross, G.W., 1979. Simultaneous Single Unit Recording in vitro with a Photoetched Laser Deinsulated Gold Multimicroelectrode Surface. IEEE Trans. Biomed. Eng. BME-26, 273–279.

Gross, G.W., Wen, W.Y., Lin, J.W., 1985. Transparent indium-tin oxide electrode patterns for extracellular, multisite recording in neuronal cultures. J. Neurosci. Methods 15, 243–252.

Gunning, D., Adams, C., Cunningham, W., Mathieson, K., O'Shea, V., Smith, K.M., Chichilnisky, E.J., Litke, A.M., Rahman, M., 2005. spacing 519-electrode arrays for in vitro retinal studies. Nucl. Instrum. Methods Phys. Res. Sect. Accel. Spectrometers Detect. Assoc. Equip. 546, 148–153.

Ha, Y.-H., Nikolov, N., Pollack, S.K., Mastrangelo, J., Martin, B.D., Shashidhar, R., 2004. Towards a Transparent, Highly Conductive Poly(3,4-ethylenedioxythiophene). Adv. Funct. Mater. 14, 615–622.

Hassler, C., Boretius, T., Stieglitz, T., 2011. Polymers for neural implants. J. Polym. Sci. Part B Polym. Phys. 49, 18–33.

He, S., Song, B., Li, D., Zhu, C., Qi, W., Wen, Y., Wang, L., Song, S., Fang, H., Fan, C., 2010. A Graphene Nanoprobe for Rapid, Sensitive, and Multicolor Fluorescent DNA Analysis. Adv. Funct. Mater. 20, 453–459.

Henle, C., Raab, M., Cordeiro, J., Doostkam, S., Schulze-Bonhage, A., Stieglitz, T., Rickert, J., 2011. First long term in vivo study on subdurally implanted Micro-ECoG electrodes, manufactured with a novel laser technology. Biomed. Microdevices 13, 59–68.

Holtmaat, A., Bonhoeffer, T., Chow, D.K., Chuckowree, J., Paola, V.D., Hofer, S.B., Hübener, M., Keck, T., Knott, G., Lee, W.-C.A., Mostany, R., Mrsic-Flogel, T.D., Nedivi, E., Portera-Cailliau, C., Svoboda, K., Trachtenberg, J.T., Wilbrecht, L., 2009. Long-term, high-resolution imaging in the mouse neocortex through a chronic cranial window. Nat. Protoc. 4, 1128–1144.

Hopkins, A., Garman, A., Clarke, C., 1988. The first seizure in adult life: value of clinical features, electroencephalography, and computerised tomographic scanning in prediction of seizure recurrence. The Lancet 331, 721–726.

Huang, D., Swanson, E.A., Lin, C.P., Schuman, J.S., Stinson, W.G., Chang, W., Hee, M.R., Flotte, T., Gregory, K., Puliafito, C.A., Et, A., 1991. Optical coherence tomography. Science 254, 1178–1181.

Humayun, M.S., Weiland, J.D., Fujii, G.Y., Greenberg, R., Williamson, R., Little, J., Mech, B., Cimmarusti, V., Van Boemel, G., Dagnelie, G., de Juan Jr., E., 2003. Visual perception in a blind subject with a chronic microelectronic retinal prosthesis. Vision Res. 43, 2573–2581.

Jasper, H.H., Shacter, D.G., Montplaisir, J., 1970. The effect of local cooling upon spontaneous and evoked electrical activity of cerebral cortex. Can. J. Physiol. Pharmacol. 48, 640–652.

Jimenz Hamann, M.C., Sacks, M.S., Malinin, T.I., 1998. Quantification of the collagen fibre architecture of human cranial dura mater. J. Anat. 192, 99–106.

Jo, G., Choe, M., Lee, S., Park, W., Kahng, Y.H., Lee, T., 2012. The application of graphene as electrodes in electrical and optical devices. Nanotechnology 23, 112001.

Kalbacova, M., Broz, A., Kong, J., Kalbac, M., 2010. Graphene substrates promote adherence of human osteoblasts and mesenchymal stromal cells. Carbon 48, 4323–4329.

Khodagholy, D., Doublet, T., Gurfinkel, M., Quilichini, P., Ismailova, E., Leleux, P., Herve, T., Sanaur, S., Bernard, C., Malliaras, G.G., 2011. Highly Conformable Conducting Polymer Electrodes for In Vivo Recordings. Adv. Mater. 23, H268–H272.

Kim, D.H., Viventi, J., Amsden, J.J., Xiao, J., Vigeland, L., Kim, Y.S., Blanco, J.A., Panilaitis, B., Frechette, E.S., Contreras, D., others, 2010. Dissolvable films of silk fibroin for ultrathin conformal bio-integrated electronics. Nat. Mater. 9, 511–517.

Kim, K.S., Zhao, Y., Jang, H., Lee, S.Y., Kim, J.M., Kim, K.S., Ahn, J.-H., Kim, P., Choi, J.-Y., Hong, B.H., 2009. Large-scale pattern growth of graphene films for stretchable transparent electrodes. Nature 457, 706–710.

Kim, Y.-T., Bridge, M.J., Tresco, P.A., 2007. The influence of the foreign body response evoked by fibroblast transplantation on soluble factor diffusion in surrounding brain tissue. J. Controlled Release 118, 340–347.

Kitzmiller, J., Beversdorf, D., Hansford, D., 2006. Fabrication and testing of microelectrodes for small-field cortical surface recordings. Biomed. Microdevices 8, 81–85.

Kleinfeld, D., Mitra, P.P., Helmchen, F., Denk, W., 1998. Fluctuations and stimulus-induced changes in blood flow observed in individual capillaries in layers 2 through 4 of rat neocortex. Proc. Natl. Acad. Sci. 95, 15741–15746.

Kumar, K., Toth, C., Nath, R., Laing, P., 1998. Epidural spinal cord stimulation for treatment of chronic pain—some predictors of success. A 15-year experience. Surg. Neurol. 50, 110–121.

Kwon, K.Y., Sirowatka, B., Li, W., Weber, A., 2012. Opto-uECoG array: Transparent u;ECoG electrode array and integrated LEDs for optogenetics, in: 2012 IEEE Biomedical Circuits and Systems Conference (BioCAS). Presented at the 2012 IEEE Biomedical Circuits and Systems Conference (BioCAS), pp. 164–167.

Ledochowitsch, P., Félus, R.J., Gibboni, R.R., Miyakawa, A., Bao, S., Maharbiz, M.M., 2011. Fabrication and testing of a large area, high density, parylene MEMS #x00B5;ECoG array, in: 2011 IEEE 24th International Conference on Micro Electro Mechanical Systems (MEMS). Presented at the 2011 IEEE 24th International Conference on Micro Electro Mechanical Systems (MEMS), pp. 1031–1034.

Ledochowitsch, P., Olivero, E., Blanche, T., Maharbiz, M.M., 2011. A transparent uECoG array for simultaneous recording and optogenetic stimulation, in: 2011 Annual International Conference of the IEEE Engineering in Medicine and Biology Society,EMBC. Presented at the 2011 Annual International Conference of the IEEE Engineering in Medicine and Biology Society,EMBC, pp. 2937–2940.

Leuthardt, E.C., Freudenberg, Z., Bundy, D., Roland, J., 2009. Microscale recording from human motor cortex: implications for minimally invasive electrocorticographic brain-computer interfaces. Neurosurg. Focus 27, E10.

Leuthardt, E.C., Schalk, G., Wolpaw, J.R., Ojemann, J.G., Moran, D.W., 2004. A brain–computer interface using electrocorticographic signals in humans. J. Neural Eng. 1, 63–71.

Levi, B., Nelson, E.R., Li, S., James, A.W., Hyun, J.S., Montoro, D.T., Lee, M., Glotzbach, J.P., Commons, G.W., Longaker, M.T., 2011. Dura Mater Stimulates Human Adipose-Derived Stromal Cells to Undergo Bone Formation in Mouse Calvarial Defects. STEM CELLS 29, 1241–1255.

Li, N., Zhang, X., Song, Q., Su, R., Zhang, Q., Kong, T., Liu, L., Jin, G., Tang, M., Cheng, G., 2011. The promotion of neurite sprouting and outgrowth of mouse hippocampal cells in culture by graphene substrates. Biomaterials 32, 9374–9382.

Li, Y., Song, Y., Zhao, L., Gaidosh, G., Laties, A.M., Wen, R., 2008. Direct labeling and visualization of blood vessels with lipophilic carbocyanine dye DiI. Nat. Protoc. 3, 1703–1708.

Liao, L., Lin, Y.-C., Bao, M., Cheng, R., Bai, J., Liu, Y., Qu, Y., Wang, K.L., Huang, Y., Duan, X., 2010. High-speed graphene transistors with a self-aligned nanowire gate. Nature 467, 305–308.

Lin, C.-M., Lee, Y.-T., Yeh, S.-R., Fang, W., 2009. Flexible carbon nanotubes electrode for neural recording. Biosens. Bioelectron. 24, 2791–2797.

Loeb, G.E., Peck, R.A., 1996. Cuff electrodes for chronic stimulation and recording of peripheral nerve activity. J. Neurosci. Methods 64, 95–103.

Lomber, S.G., Payne, B.R., Horel, J.A., 1999. The cryoloop: an adaptable reversible cooling deactivation method for behavioral or electrophysiological assessment of neural function. J. Neurosci. Methods 86, 179–194.

Ludwig, K.A., Uram, J.D., Yang, J., Martin, D.C., Kipke, D.R., 2006. Chronic neural recordings using silicon microelectrode arrays electrochemically deposited with a poly (3, 4-ethylenedioxythiophene)(PEDOT) film. J. Neural Eng. 3, 59.

Mabeta, P., Pepper, M.S., 2011. Hemangiomas—Current therapeutic strategies. Int. J. Dev. Biol. 55, 431.

Marker, D.F., Tremblay, M., Lu, S., Majewska, A.K., Gelbard, H.A., 2010. A Thin-skull Window Technique for Chronic Two-photon In vivo Imaging of Murine Microglia in Models of.

Marmor, M.F., Holder, G.E., Seeliger, M.W., Yamamoto, S., 2004. Standard for clinical electroretinography (2004 update). Doc. Ophthalmol. 108, 107–114.

Mayhan, W.G., Heistad, D.D., 1985. Permeability of blood-brain barrier to various sized molecules. Am. J. Physiol. - Heart Circ. Physiol. 248, H712–H718.

Maynard, E.M., Nordhausen, C.T., Normann, R.A., 1997. The Utah intracortical electrode array: a recording structure for potential brain-computer interfaces. Electroencephalogr. Clin. Neurophysiol. 102, 228–239.

Min, S.K., Kim, W.Y., Cho, Y., Kim, K.S., 2011. Fast DNA sequencing with a graphene-based nanochannel device. Nat. Nanotechnol. 6, 162–165.

Minami, T., 2008. Substitution of transparent conducting oxide thin films for indium tin oxide transparent electrode applications. Thin Solid Films 516, 1314–1321.

Murphy, W.L., Simmons, C.A., Kaigler, D., Mooney, D.J., 2004. Bone regeneration via a mineral substrate and induced angiogenesis. J. Dent. Res. 83, 204–210.

Navarro, X., Krueger, T.B., Lago, N., Micera, S., Stieglitz, T., Dario, P., 2005. A critical review of interfaces with the peripheral nervous system for the control of neuroprostheses and hybrid bionic systems. J. Peripher. Nerv. Syst. 10, 229–258.

Noh, H., Moon, K., Cannon, A., Hesketh, P.J., Wong, C.P., 2004. Wafer bonding using microwave heating of parylene intermediate layers. J. Micromechanics Microengineering 14, 625.

Norlin, P., Kindlundh, M., Mouroux, A., Yoshida, K., Hofmann, U.G., 2002. A 32-site neural recording probe fabricated by DRIE of SOI substrates. J. Micromechanics Microengineering 12, 414–419.

North, R.B., Kidd, D.H., Olin, J.C., Sieracki, J.M., 2002. Spinal cord stimulation electrode design: prospective, randomized, controlled trial comparing percutaneous and laminectomy electrodes-part I: technical outcomes. Neurosurgery 51, 381–390.

Otto, K.J., Johnson, M.D., Kipke, D.R., 2006. Voltage pulses change neural interface properties and improve unit recordings with chronically implanted microelectrodes. Biomed. Eng. IEEE Trans. On 53, 333–340.

Oyama, Y., Kazama, J.J., Fukagawa, M., Arakawa, Y., Ezuka, I., 2010. Ectopic ossification in the cranial dura mater in dialysis patients with secondary hyperparathyroidism. NDT Plus 3, 64–67.

Özer, E., Mungan, M.U., Tuna, B., Kazimoğlu, H., Yörükoğlu, K., KIrkalI, Z., 1999. Prognostic significance of angiogenesis and immunoreactivity of cathepsin d and type IV collagen in high-grade stage T1 primary bladder cancer. Urology 54, 50–55.

Paetzold, R., Heuser, K., Henseler, D., Roeger, S., Wittmann, G., Winnacker, A., 2003. Performance of flexible polymeric light-emitting diodes under bending conditions. Appl. Phys. Lett. 82, 3342–3344.

Park, S.K., Han, J.I., Kim, W.K., Kwak, M.G., 2001. Deposition of indium–tin-oxide films on polymer substrates for application in plastic-based flat panel displays. Thin Solid Films 397, 49–55.

Park, S.Y., Park, J., Sim, S.H., Sung, M.G., Kim, K.S., Hong, B.H., Hong, S., 2011. Enhanced Differentiation of Human Neural Stem Cells into Neurons on Graphene. Adv. Mater. 23, H263–H267.

Perlmutter, J.S., Mink, J.W., 2006. Deep brain stimulation. Annu Rev Neurosci 29, 229–257.

Pinto, A.M., Gonçalves, I.C., Magalhães, F.D., 2013. Graphene-based materials biocompatibility: A review. Colloids Surf. B Biointerfaces 111, 188–202.

Pokaipisit, A., Horprathum, M., Limsuwan, P., 2008. Influence of Annealing Temperature on the Properties of ITO Films Prepared by Electron Beam Evaporation and Ion-Assisted Deposition. Kasetsart JNat Sci 42, 362–366.

Polikov, V.S., Tresco, P.A., Reichert, W.M., 2005. Response of brain tissue to chronically implanted neural electrodes. J. Neurosci. Methods 148, 1–18.

Postma, H.W.C., 2010. Rapid Sequencing of Individual DNA Molecules in Graphene Nanogaps. Nano Lett. 10, 420–425.

Potter, S.M., Wang, C.-M., Garrity, P.A., Fraser, S.E., 1996. Intravital imaging of green fluorescent protein using two-photon laser-scanning microscopy. Gene 173, 25–31.

Protasoni, M., Sangiorgi, S., Cividini, A., Culuvaris, G.T., Tomei, G., Dell'Orbo, C., Raspanti, M., Balbi, S., Reguzzoni, M., 2011. The collagenic architecture of human dura mater. J. Neurosurg. 114, 1723–1730.

Provenzano, P.P., Eliceiri, K.W., Keely, P.J., 2009. Multiphoton microscopy and fluorescence lifetime imaging microscopy (FLIM) to monitor metastasis and the tumor microenvironment. Clin. Exp. Metastasis 26, 357–370.

Richardson-Burns, S.M., Hendricks, J.L., Foster, B., Povlich, L.K., Kim, D.-H., Martin, D.C., 2007a. Polymerization of the conducting polymer poly (3, 4-ethylenedioxythiophene)(PEDOT) around living neural cells. Biomaterials 28, 1539–1552.

Richardson-Burns, S.M., Hendricks, J.L., Martin, D.C., 2007b. Electrochemical polymerization of conducting polymers in living neural tissue. J. Neural Eng. 4, L6.

Richner, T.J., Thongpang, S., Brodnick, S.K., Schendel, A.A., Falk, R.W., Krugner-Higby, L.A., Pashaie, R., Williams, J.C., 2014. Optogenetic micro-electrocorticography for modulating and localizing cerebral cortex activity. J. Neural Eng. 11, 016010.

Richner, T.J., Thongpang, S., Brodnick, S.K., Schendel, A.A., Falk, R.W., Krugner-Higby, L.A., Pashaie, R., Williams, J.C., n.d. Optogenetic micro-electrocorticography for modulating and localizing cerebral cortex activity. J. Neural Eng.

Risling, M., Fried, K., Lindå, H., Carlstedt, T., Cullheim, S., 1993. Regrowth of motor axons following spinal cord lesions: Distribution of laminin and collagen in the CNS scar tissue. Brain Res. Bull. 30, 405–414.

Rodri´guez, F.J., Ceballos, D., Schu¨ttler, M., Valero, A., Valderrama, E., Stieglitz, T., Navarro, X., 2000. Polyimide cuff electrodes for peripheral nerve stimulation. J. Neurosci. Methods 98, 105–118.

Roggendorf, W., Opitz, H., Schuppan, D., 1988. Altered expression of collagen type VI in brain vessels of patients with chronic hypertension. Acta Neuropathol. (Berl.) 77, 55–60.

Roitbak, T., Syková, E., 1999. Diffusion barriers evoked in the rat cortex by reactive astrogliosis. Glia 28, 40–48.

Rothman, S.M., Smyth, M.D., Yang, X.F., Peterson, G., 2005. Focal cooling for epilepsy: an alternative therapy that might actually work. Epilepsy Behav. 7, 214–221.

Rousche, P.J., Pellinen, D.S., Pivin, D.P., J., Williams, J.C., Vetter, R.J., kirke, D.R., 2001. Flexible polyimide-based intracortical electrode arrays with bioactive capability. IEEE Trans. Biomed. Eng. 48, 361–371.

Rouse, A.G., Williams, J.J., Wheeler, J.J., Moran, D.W., 2013. Cortical Adaptation to a Chronic Micro-Electrocorticographic Brain Computer Interface. J. Neurosci. 33, 1326–1330.

Rubehn, B., Bosman, C., Oostenveld, R., Fries, P., Stieglitz, T., 2009. A MEMS-based flexible multichannel ECoG-electrode array. J. Neural Eng. 6, 036003.

Sajanti, J., Björkstrand, A.-S., Finnilä, S., Heikkinen, E., Peltonen, J., Majamaa, K., 1999. Increase of collagen synthesis and deposition in the arachnoid and the dura following subarachnoid hemorrhage in the rat. Biochim. Biophys. Acta BBA - Mol. Basis Dis. 1454, 209–216.

Schendel, A.A., Thongpang, S., Brodnick, S.K., Richner, T.J., Lindevig, B.D.B., Krugner-Higby, L., Williams, J.C., 2013. A cranial window imaging method for monitoring vascular growth around chronically implanted micro-ECoG devices. J. Neurosci. Methods 218, 121–130.

Schneider, G.F., Kowalczyk, S.W., Calado, V.E., Pandraud, G., Zandbergen, H.W., Vandersypen, L.M.K., Dekker, C., 2010. DNA Translocation through Graphene Nanopores. Nano Lett. 10, 3163–3167.

Schwartz, A.B., 2004. Cortical Neural Prosthetics. Annu. Rev. Neurosci. 27, 487–507.

Schwartz, A.B., Cui, X.T., Weber, D.J., Moran, D.W., 2006. Brain-Controlled Interfaces: Movement Restoration with Neural Prosthetics. Neuron 52, 205–220.

Segler, A., Tsimberidou, A.-M., 2012. Lenalidomide in solid tumors. Cancer Chemother. Pharmacol. 69, 1393–1406.

Selner, A.N., Ban, T., Williams, J., Thongpang, S., Hetling, J.R., 2011. Novel contact lens electrode array for multi-electrode electroretinography (meERG), in: Bioengineering Conference (NEBEC), 2011 IEEE 37th Annual Northeast. Presented at the Bioengineering Conference (NEBEC), 2011 IEEE 37th Annual Northeast, pp. 1–2.

Seymour, J.P., Kipke, D.R., 2007. Neural probe design for reduced tissue encapsulation in CNS. Biomaterials 28, 3594–3607.

Shirani, J., Pick, R., Roberts, W.C., Maron, B.J., 2000. Morphology and significance of the left ventricular collagen network in young patients with hypertrophic cardiomyopathy and sudden cardiac death. J. Am. Coll. Cardiol. 35, 36–44.

Sohn, J.-Y., Park, J.-C., Um, Y.-J., Jung, U.-W., Kim, C.-S., Cho, K.-S., Choi, S.-H., 2010. Spontaneous healing capacity of rabbit cranial defects of various sizes. J. Periodontal Implant Sci. 40, 180–187.

Stead, M., Bower, M., Brinkmann, B.H., Lee, K., Marsh, W.R., Meyer, F.B., Litt, B., Gompel, J.V., Worrell, G.A., 2010. Microseizures and the spatiotemporal scales of human partial epilepsy. Brain 133, 2789–2797.

Sun, Y., Weber, K.T., 2000. Infarct scar: a dynamic tissue. Cardiovasc. Res. 46, 250–256.

Szarowski, D.H., Andersen, M.D., Retterer, S., Spence, A.J., Isaacson, M., Craighead, H.G., Turner, J.N., Shain, W., 2003. Brain responses to micro-machined silicon devices. Brain Res. 983, 23–35.

Takeuchi, S., Ziegler, D., Yoshida, Y., Mabuchi, K., Suzuki, T., 2005. Parylene flexible neural probes integrated with microfluidic channels. Lab. Chip 5, 519–523.

Tanaka, N., Fujii, M., Imoto, H., Uchiyama, J., Nakano, K., Nomura, S., Fujisawa, H., Kunitsugu, I., Saito, T., Suzuki, M., 2008. Effective suppression of hippocampal seizures in rats by direct hippocampal cooling with a Peltier chip.

Tearney, G.J., Brezinski, M.E., Southern, J.F., Bouma, B.E., Hee, M.R., Fujimoto, J.G., 1995. Determination of the refractive index of highly scattering human tissue by optical coherence tomography. Opt. Lett. 20, 2258–2260.

Thongpang, S., Richner, T.J., Brodnick, S.K., Schendel, A., Kim, J., Wilson, J., Hippensteel, J., Krugner-Higby, L., Moran, D., Ahmed, A.S., others, 2011. A micro-electrocorticography platform and deployment strategies for chronic BCI applications. Clin. EEG Neurosci. Off. J. EEG Clin. Neurosci. Soc. ENCS 42, 259.

Tozer, G.M., Ameer-Beg, S.M., Baker, J., Barber, P.R., Hill, S.A., Hodgkiss, R.J., Locke, R., Prise, V.E., Wilson, I., Vojnovic, B., 2005. Intravital imaging of tumour vascular networks using multi-photon fluorescence microscopy. Adv. Drug Deliv. Rev. 57, 135–152.

Trachtenberg, J.T., Chen, B.E., Knott, G.W., Feng, G., Sanes, J.R., Welker, E., Svoboda, K., others, 2002. Long-term in vivo imaging of experience-dependent synaptic plasticity in adult cortex. Nature 420, 788–794.

Tremblay, M.-È., Majewska, A.K., 2011. A role for microglia in synaptic plasticity? Commun. Integr. Biol. 4, 220–222.

Tsai, H.-C., Zhang, F., Adamantidis, A., Stuber, G.D., Bonci, A., Lecea, L. de, Deisseroth, K., 2009. Phasic Firing in Dopaminergic Neurons Is Sufficient for Behavioral Conditioning. Science 324, 1080–1084.

Van Zuijlen, P.P.M., Ruurda, J.J.B., van Veen, H.A., van Marle, J., van Trier, A.J.M., Groenevelt, F., Kreis, R.W., Middelkoop, E., 2003. Collagen morphology in human skin and scar tissue: no adaptations in response to mechanical loading at joints. Burns 29, 423–431.

Vetter, R.J., Williams, J.C., Hetke, J.F., Nunamaker, E.A., Kipke, D.R., 2004. Chronic neural recording using silicon-substrate microelectrode arrays implanted in cerebral cortex. Biomed. Eng. IEEE Trans. On 51, 896–904.

Villringer, A., Them, A., Lindauer, U., Einhaupl, K., Dirnagl, U., 1994. Capillary perfusion of the rat brain cortex. An in vivo confocal microscopy study. Circ. Res. 75, 55 –62.

Viventi, J., Kim, D.-H., Vigeland, L., Frechette, E.S., Blanco, J.A., Kim, Y.-S., Avrin, A.E., Tiruvadi, V.R., Hwang, S.-W., Vanleer, A.C., Wulsin, D.F., Davis, K., Gelber, C.E., Palmer, L., Spiegel, J.V. der, Wu, J., Xiao, J., Huang, Y., Contreras, D., Rogers, J.A., Litt, B., 2011. Flexible, foldable, actively multiplexed, high-density electrode array for mapping brain activity in vivo. Nat. Neurosci. 14, 1599–1605.

Wang, H., Cui, L.-F., Yang, Y., Sanchez Casalongue, H., Robinson, J.T., Liang, Y., Cui, Y., Dai, H., 2010. Mn3O4–Graphene Hybrid as a High-Capacity Anode Material for Lithium Ion Batteries. J. Am. Chem. Soc. 132, 13978–13980.

Wang, W., Degenhart, A.D., Collinger, J.L., Vinjamuri, R., Sudre, G.P., Adelson, P.D., Holder, D.L., Leuthardt, E.C., Moran, D.W., Boninger, M.L., Schwartz, A.B., Crammond, D.J., Tyler-Kabara, E.C., Weber, D.J., 2009. Human motor cortical activity recorded with Micro-ECoG electrodes, during individual finger movements. Conf. Proc. Annu. Int. Conf. IEEE Eng. Med. Biol. Soc. IEEE Eng. Med. Biol. Soc. Conf. 2009, 586–589.

Wang, X., Zhi, L., Mullen, K., 2008. Transparent, Conductive Graphene Electrodes for Dye-Sensitized Solar Cells. Nano Lett. 8, 323–327.

Widge, A.S., Jeffries-El, M., Cui, X., Lagenaur, C.F., Matsuoka, Y., 2007. Self-assembled monolayers of polythiophene conductive polymers improve biocompatibility and electrical impedance of neural electrodes. Biosens. Bioelectron. 22, 1723–1732.

Wilks, S.J., Richner, T.J., Brodnick, S.K., Kipke, D.R., Williams, J.C., Otto, K.J., 2012. Voltage Biasing, Cyclic Voltammetry, & Electrical Impedance Spectroscopy for Neural Interfaces. J. Vis. Exp. JoVE.

Williams, J.C., Hippensteel, J.A., Dilgen, J., Shain, W., Kipke, D.R., 2007. Complex impedance spectroscopy for monitoring tissue responses to inserted neural implants. J. Neural Eng. 4, 410.

Williams, J.C., Rennaker, R.L., Kipke, D.R., 1999. Long-term neural recording characteristics of wire microelectrode arrays implanted in cerebral cortex. Brain Res. Protoc. 4, 303–313.

Williams, J.J., Rouse, A.G., Thongpang, S., Williams, J.C., Moran, D.W., 2013. Differentiating closed-loop cortical intention from rest: building an asynchronous electrocorticographic BCI. J. Neural Eng. 10, 046001.

Wilson, J.A., Felton, E.A., Garell, P.C., Schalk, G., Williams, J.C., 2006. ECoG factors underlying multimodal control of a brain-computer interface. Neural Syst. Rehabil. Eng. IEEE Trans. On 14, 246–250.

Woolley, A., Desai, H., Otto, K., 2011. Imaging the Tissue Response Around Brain-Implanted Microdevices. Microsc. Microanal. 17, 146–147.

Wu, J., Becerril, H.A., Bao, Z., Liu, Z., Chen, Y., Peumans, P., 2008. Organic solar cells with solution-processed graphene transparent electrodes. Appl. Phys. Lett. 92, 263302.

Xia, F., Mueller, T., Golizadeh-Mojarad, R., Freitag, M., Lin, Y., Tsang, J., Perebeinos, V., Avouris, P., 2009. Photocurrent Imaging and Efficient Photon Detection in a Graphene Transistor. Nano Lett. 9, 1039–1044.

Xiao, Y., Cui, X., Hancock, J.M., Bouguettaya, M., Reynolds, J.R., Martin, D.C., 2004. Electrochemical polymerization of poly(hydroxymethylated-3,4-ethylenedioxythiophene) (PEDOT-MeOH) on multichannel neural probes. Sens. Actuators B Chem. 99, 437–443.

Xu, H.-T., Pan, F., Yang, G., Gan, W.-B., 2007. Choice of cranial window type for in vivo imaging affects dendritic spine turnover in the cortex. Nat. Neurosci. 10, 549–551.

Yang, J., Kim, D.H., Hendricks, J.L., Leach, M., Northey, R., Martin, D.C., 2005. Ordered surfactant-templated poly (3, 4-ethylenedioxythiophene)(PEDOT) conducting polymer on microfabricated neural probes. Acta Biomater. 1, 125–136.

Yang, X., Liu, G., Balandin, A.A., Mohanram, K., 2010. Triple-Mode Single-Transistor Graphene Amplifier and Its Applications. ACS Nano 4, 5532–5538.

Yoo, E., Kim, J., Hosono, E., Zhou, H., Kudo, T., Honma, I., 2008. Large Reversible Li Storage of Graphene Nanosheet Families for Use in Rechargeable Lithium Ion Batteries. Nano Lett. 8, 2277–2282.

Yoo, J.-M., Song, J.-I., Tathireddy, P., Solzbacher, F., Rieth, L.W., 2012. Hybrid laser and reactive ion etching of Parylene-C for deinsulation of a Utah electrode array. J. Micromechanics Microengineering 22, 105036.

Yuen, T.G.H., Agnew, W.F., 1995. Histological evaluation of polyesterimide-insulated gold wires in brain. Biomaterials 16, 951–956.

Zeisberger, S.M., Odermatt, B., Marty, C., Zehnder-Fjällman, A.H.M., Ballmer-Hofer, K., Schwendener, R.A., 2006. Clodronate-liposome-mediated depletion of tumour-associated macrophages: a new and highly effective antiangiogenic therapy approach. Br. J. Cancer 95, 272–281.

Zhang, Y., Ali, S.F., Dervishi, E., Xu, Y., Li, Z., Casciano, D., Biris, A.S., 2010. Cytotoxicity Effects of Graphene and Single-Wall Carbon Nanotubes in Neural Phaeochromocytoma-Derived PC12 Cells. ACS Nano 4, 3181–3186.

Ziegler, D., Suzuki, T., Takeuchi, S., 2006. Fabrication of flexible neural probes with built-in microfluidic channels by thermal bonding of parylene. Microelectromechanical Syst. J. Of 15, 1477–1482.